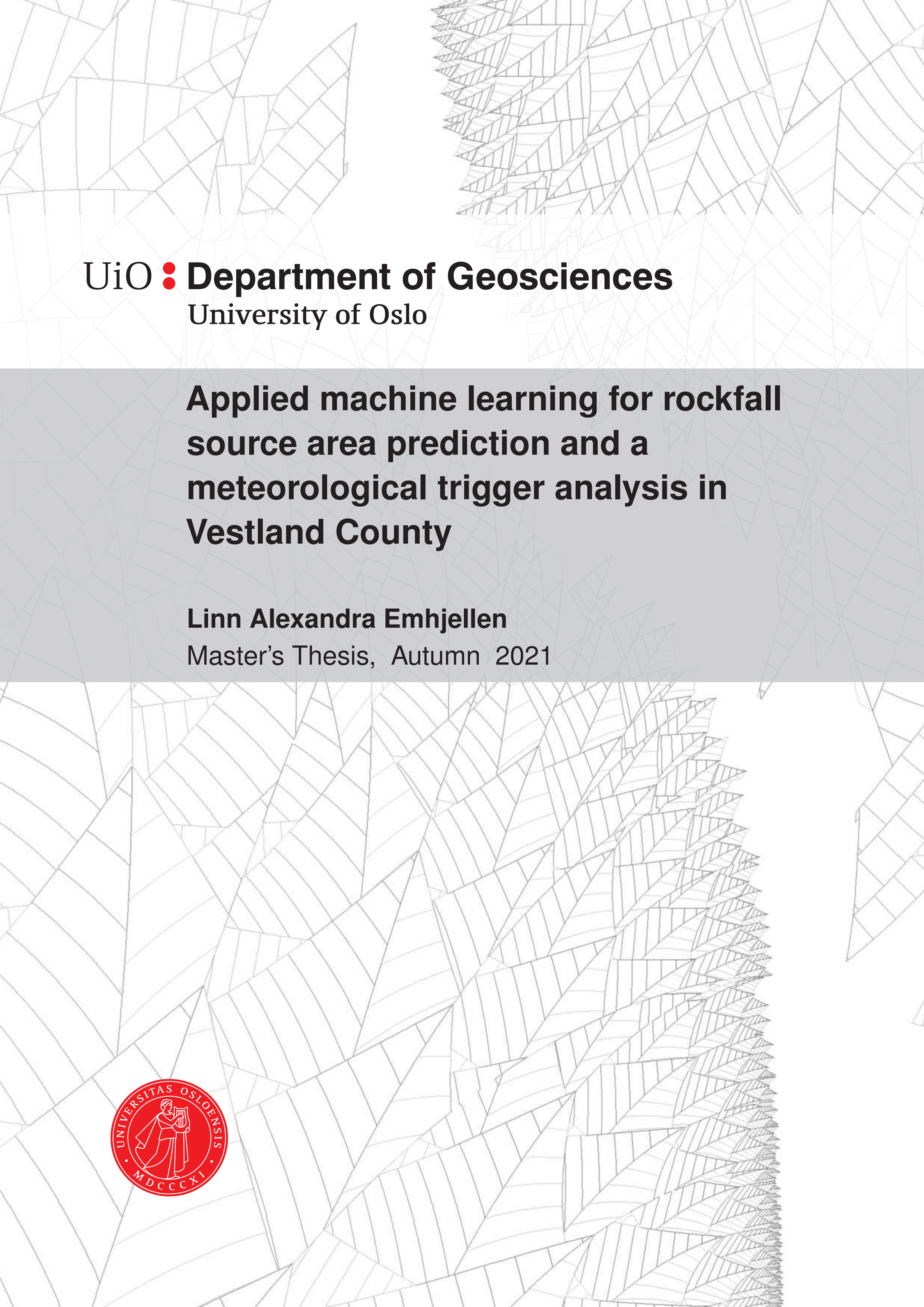

UiO : **Department of Geosciences**
University of Oslo

# Applied machine learning for rockfall source area prediction and a meteorological trigger analysis in Vestland County

**Linn Alexandra Emhjellen**
Master's Thesis, Autumn 2021

Applied machine learning for rockfall source area prediction and a meteorological trigger analysis in Vestland County

http://www.duo.uio.no/

Printed: Reprosentralen, University of Oslo

# Abstract

One of the main challenges in the rockfall hazard assessment is to determine where and when rockfall occurs. The existing national susceptibility map with potential rockfall source areas in Norway based on slope angle thresholds and whether the terrain is on "bare rock" do not consider any other factors influencing rockfall probability. This study investigates the potentials and limitations of applying four machine learning (ML) algorithms for the spatial prediction of rockfall source areas. The "ensemble" Random Forest (RF), the "ensemble" Gradient Boosted Regression Tree (GBRT), the Multilayer Perceptron neural network (MLP), and the Logistic Regression (LR) model were introduced for this purpose.

Machine learning models, developed using different combinations of input features, were trained and cross-validated with data from the municipalities of Lærdal and Aurland. The final models were tested, without being recalibrated, for two other areas in Vestland County to investigate the models' regional performance. All four machine learning algorithms were capable of predicting rockfall source areas, with the GBRT model yielding the most promising results. However, the modeled rockfall source areas need further evaluation due to uncertainties related to spatial dependency in the data. This limitation is a fundamental challenge with machine learning in Geosciences. Maps displaying rockfall source areas categorized into four different susceptibility classes were created from predicted probabilities compared to the existing national map and other maps obtained from statistical methods.

Two data sets were collected in order to investigate how temperature and precipitation affect rockfall release probability. One represents the "normal climate" in Vestland and the other the climate when rockfall occurs. Differences between the data sets were described using statistical methods. Freeze-thaw was the most significant weather type to trigger rockfalls in the current climate in Vestland County, with most rockfall events occurring on a day of thawing. The local and seasonal effects were explored by fitting individual Logistic Regression models for 16 locations and each month. Results show that the effect of temperature and precipitation varies with both location and month, leading to the recommendation of adopting Hierarchical Bayesian models for temporal prediction in the future.

# Acknowledgements

I am very thankful for everyone who has helped me through this year.

First of all, I would like to thank my supervisors. Thank you Ulrik Domaas, Anders Solheim and Bernd Etzelmüller for the guidance, advice and encouragements.

I am also grateful to Zhoungqiang Liu for sharing his expertise in the field of Machine Learning. Thank you for your patience and valuable opinions. Also, thank you Nezam Bozorgzadeh for valuable discussions during the summer.

Thank you, Luc Girod, at The University of Oslo, for providing the script to extract SeNorge2 data.

I would also like to use this opportunity to thank my fellow students in study room 210. You have been invaluable in this strange year in the middle of a pandemic. Thank you for long conversations, sharing of foods, and many laughs.

A huge thank you to Elin, Mina, Nellie, and Tham for the friendship that began in our first year at the University of Oslo. I know it will last a lifetime!

Then, I would like to thank my family and friends for always supporting and believing in me.

And lastly, a very special thanks to Mikkel. Thank you for all love, support, and late-night dinners.

Oslo, 17.08.2021

Linn Alexandra Emhjellen

# Contents

# List of Figures

# List of Tables

# Abbrevations and Acronyms

| | |
|---|---|
| **ACC** | Accuracy |
| **AIC** | Akaike information criterion |
| **AUC** | Area Under the Curve |
| **CV** | Cross Validation |
| **FN** | False Negative |
| **FP** | False Positive |
| **GBRT** | Gradient Boosted Regression Tree |
| **KCV** | K-fold Cross Validation |
| **LiDAR** | Light Detection and Radar |
| **LR** | Logistic Regression |
| **ML** | Machine Learning |
| **MLP** | Multilayer Perceptron |
| **RF** | Random Forest |
| **ROC** | Receiver Operating Characteristics |
| **SWE** | Snow Water Equivalent |
| **TN** | True Negative |
| **TP** | True Positive |
| **TRI** | Terrain Ruggedness Index |

# Chapter 1

# Introduction

## 1.1 Rockfall - A rapid mass movement process

The topography and climate of Norway make large parts of the country susceptible to gravity-driven geohazards such as landslides, debris flows, and rockfalls. Mass movements pose a potential threat to transportation and power infrastructure. They may also cause property damage and loss of life (Ministry of Petroleum and Energy, 2012). A rockfall is a detachment and subsequent fall of rock fragments from a cliff. Individual rock fragments move like rigid bodies, interacting with the runout path through episodic impacts. The movement of rock avalanches, on the other hand, can be described as a more flow-like movement of masses of multiple rock fragments (Hungr et al., 2014). The rock fragment will roll, slide, or bounce down the path until the slope decreases and it deposits (Hungr et al., 2014). It is a rapid process, making it nearly impossible to act when an event occurs (Volkwein et al., 2011).

Since 1900, 125 rock avalanche and rockfall events have resulted in more than 300 fatalities in Norway, according to historical records (Ministry of Petroleum and Energy, 2012). Approximately half of these fatalities were caused by three rock avalanche events in Western Norway: the Loen accidents (1905 and 1036) and the Tafjord accident (1934), in which rock masses were deposited in the fjords and caused fatal tsunamis. The most common result of smaller and more frequent rockfall events is the temporary closure of transportation routes and economic losses due to damage to buildings and roads.

The Norwegian Public Roads Administration reports an average of 530 observed annual mass movement events at roads in Vestland county (Vegvesen, 2019; Figure 1.1). The most common type of mass movement observed is landslides and rockfalls, and it is estimated that one-third of events reaching the roads go unreported. Understanding this rapid process is critical for predicting where and when an event will occur and how far the runout will be. Knowing when an event is likely to occur will assist regional and local authorities prepare for the next event, establish early warning systems, and implement mitigation measures. Tunnels, retaining structures, and rerouting high-risk roads are examples of such measures.

All bedrock slopes are subject to weathering, which can result in fracturing and joint opening (L. K. Dorren, 2003). Existing discontinuities and fractures increase the likelihood of rockfall occurrence depending on their density and orientation. The degree of weathering is determined by bedrock type and environmental factors that cause mechanical and chemical weathering, but the triggering mechanisms determine whether and when a rockfall event occurs (L. K. Dorren, 2003). Several factors have been reported in the literature as the triggering cause of rockfall (Sandersen et al., 1997, L. K. Dorren, 2003, Dyrrdal et al., 2012, Allen and Huggel, 2013, Matsuoka, 2019). Rockfall is usually caused by a combination of topographical, geological, and climatological factors.

A rockfall hazard assessment should thus consider both the *spatial* and *temporal* probability of events (Volkwein et al., 2011). Identifying rockfall source areas is a necessary but time-consuming step in such an assessment (Fanos and Pradhan, 2019). Rockfall source areas can be identified in the field or by researching rockfall inventories, both of which are time-consuming and expensive methods. The Geological Survey of Norway (NGU) created a national susceptibility map for rockfall in 2009 on appointment for the Norwegian Water Resources and Energy Directorate (NVE). The map displays potential release areas as well as run-out zones. Thresholds based on slope angle and whether the surface is categorized as "bare rock" determine the release zones, but no other conditional or triggering mechanisms are considered. A more detailed susceptibility can be used to prioritize areas for further hazard mapping, such as identifying unstable blocks, modeling run-out lengths, estimating the magnitude of potential events, estimating return periods, and planning mitigation measures (Volkwein et al., 2011).

Figure 1.1: Road (Fylkesvei) 337 Veitastrond in the municipality of Luster, 2014(Jens Tveit, Vegvesen, 2019).

A semi-automatic method for rockfall source area identification would thus be a step forward in assessing rockfall hazards. This thought formed the basis for the first part of the thesis; To determine whether different machine learning algorithms could be applied to predict potential rockfall source areas in Vestland county.

This study will propose a new methodology for the spatial prediction of rockfall source areas. Once the data has been collected and processed, machine learning algorithms can "learn" from the relationships in the training data and are simple to use. A few studies have applied machine learning methods for rockfall susceptibility mapping in recent years (Bagheri et al., 2018, Losasso and Sdao, 2018, Fanos and Pradhan, 2019), but no study has applied machine learning algorithms for rockfall source area prediction in Norway to date. Random Forest (RF), Multilayer Perceptron (MLP), Logistic Regression (LR) and Gradient Boosted Regression Trees (GBRT) were evaluated for this purpose.

The temporal susceptibility of rockfall occurrence has yet to be combined with the spatial susceptibility in machine learning techniques, which is difficult due to the practical limitations of the national rockfall inventory database. As a result, the approach to addressing the problem of temporal distribution resulted in the second part of the thesis; An statistical analysis of two meteorological databases. One database represents the "Rockfall climate," and the other represents the "normal situation" in Vestland County. The Kruskal Wallis method will be used to describe the differences between the two databases, while Logistic regression will be used to describe the effects of temperature and precipitation on the probability of rockfall occurrence. Meteorological models make it possible to forecast the weather, but knowledge about the correlation between rockfall occurrences and factors such as temperature and precipitation is still limited (Delonca et al., 2014).

The climate is changing, and the frequency of heavy precipitation will likely increase during the 21st century (Seneviratne et al., 2012, Hanssen-Bauer et al., 2017). Better knowledge about the effects of weather on rockfall release may help project the future frequency of rockfall events triggered by weather conditions. This thesis aims to explore the potentials and limitations of machine learning methods for rockfall source area prediction and enlighten some of the questions regarding the correlation between temperature, precipitation, and rockfall occurrence in Vestland. The thesis is part of a project at The Norwegian Geotechnical Institute (NGI) that addresses various aspects of uncertainty in rockfall runout path modeling and predicting rockfall occurrence probability.

## 1.2 Objectives

The thesis's main objective or overarching aim is to explore the potentials and limitations of machine learning methods for rockfall source area prediction in Vestland and discuss the effects of precipitation and temperature as triggering mechanisms for rockfall.

The following research questions will be investigated:

- How well do ensemble machine learning methods predict rockfall source areas in Vestland compared to the more simple Logistic Regression model?
- Is there a significant difference in Vestland County between the "rockfall climate" and the "normal situation"?
- How significant are the effects of weather conditions on the probability of rockfall release? Furthermore, is it possible to fit a Logistic regression prediction model for Vestland County using temperature and precipitation?

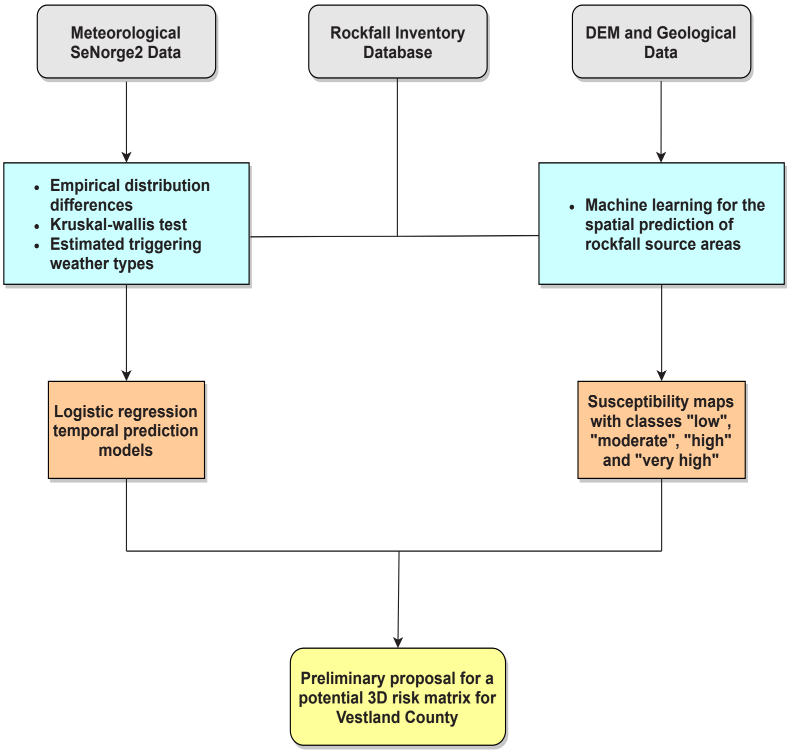

Figure 1.2: The structure of the thesis is depicted in a flowchart. The thesis is divided into two parts: a spatial analysis for the prediction of rockfall source areas in Vestland and a temporal analysis of the effects of temperature and precipitation on the occurrence of rockfalls in Vestland. Combining the findings of these two parts is discussed in the final section of the Discussion chapter.

# Chapter 2

# Background and Theoretical Framework

## 2.1 A summary of previous work

Several studies have been conducted to better understand the nature of rockfalls. Popular topics have included conditional and triggering mechanisms, empirical and dynamical runout modeling, and risk prediction from rockfall occurrence. This brief summary focuses on research on meteorological triggering mechanisms and machine learning for mass-movement prediction.

### 2.1.1 Triggering mechanisms

Luckman (1976) divided the major controls of rockfall release into two categories: (1) climatic factors such as temperature and the availability and state of water as trigger mechanisms, and (2) geologic factors that influence the spatial distribution of rockfall activity. A well-known triggering mechanism of rockfall is freeze-thaw activity (Grove, 1972, Coutard and Francou, 1989, McCarroll et al., 1998, Matsuoka and Sakai, 1999, Rupp and Damm, 2020, Douglas, 1980). Rockfalls triggered by frost-thaw activity are low-magnitude, high-frequency events that are common in alpine areas (Hungr et al., 1999, cited in L. K. Dorren, 2003). Rupp and Damm (2020) used 670 rockfall events recorded over the last 200 years to analyze the spatial and temporal occurrence of rockfalls in a national rockfall database from Germany. According to the study, rockfall occurs primarily during the winter months, and freeze-thaw cycles are the primary cause of rockfall in the area (Rupp and Damm, 2020).

The effects of precipitation as a triggering mechanism are more uncertain. Rapp (1960) suggested that rainfall diminishing the internal friction between slip planes in the bedrock, rainfall causing high hydrostatic pressure in joints, and rainfall facilitating the thawing of ice after frost bursting may contribute to the release of rockfalls in autumn. While Matsuoka and Sakai (1999) stated that no apparent relationship between the number of rockfalls and the number of precipitation events was observed in their study.

Few studies have attempted to quantify the influence of meteorological factors on rockfall frequency (Delonca et al., 2014). Macciotta et al. (2017), however, conducted a study to quantify rockfall probabilities and their temporal distribution associated with weather seasonality. The study used an inventory database of rockfalls along a railway corridor in the Canadian Cordillera, consisting of 102 rockfall events.

A Binomial distribution was used to estimate the probability of rockfall events based on their recorded frequency. The study found that the dryer months coincided with the months with the lowest frequency of rockfalls, implying that the decrease in rockfall occurrences could be explained by less precipitation during these months. Increased precipitation in November also corresponded to peaks in recorded rockfall occurrences (Macciotta et al., 2017). The lowest daily rockfall probability was estimated to be in May and July, with the highest daily rockfall probability estimated to be in October (Macciotta et al., 2017).

Using three different databases with varying frequencies of rockfall events, Delonca et al. (2014) conducted a study to detect a statistical correlation between meteorological and rockfall databases. For the high-frequency database, the standard time series approach highlighted the already obvious correlation between precipitation, temperature, and rockfall. For low-frequency databases, a new methodology was proposed. The objective of this methodology is to weigh the number of rockfalls by the probability of occurrence of the studied triggering factor (Delonca et al., 2014). The approach confirmed the positive correlation between rainfall and rockfall events in one of the low-frequency databases and the correlation between cumulative rainfall and rockfalls in the other low-frequency database (Delonca et al., 2014). Many rockfalls occur when other triggering factors, such as precipitation and freezing conditions, are absent. Collins and Stock (2016) did a study on the triggering of exfoliation fractures by cyclic thermal stressing. The study found that heating and cooling cycles can cause deformation and stresses capable of fracturing granitic exfoliation sheets, and that both increasing temperatures and temperature fluctuations can promote fracture (Collins and Stock, 2016).

The prediction of rockfall occurrence remains a difficult task. Marquínez et al. (2003) investigated the susceptibility of mountain cliffs in North Spain to rockfall. The goal was to create a statistical, predictive model of rockfall activity using only a few environmental and geological variables. There were two different rockfall activity indexes determined (Marquínez et al., 2003). The Susceptibility Statistical Model of Rockfall was developed using multivariate logistic regression analysis, with rockfall activity as the dependent variable and altitude, slope gradient, roughness, solar radiation, and lithology structure as independent variables.

### 2.1.2 Machine learning for prediction of mass movements

Recently, a few studies have been conducted in which machine learning methods have been applied to the spatial distribution of mass-movement processes. Bagheri et al. (2018) used various methods to predict rockfall occurrence caused by the Changureh-Avaj Earthquake in 2002, including Logistic Regression (LR) and artificial neural networks (MLP and RBF).A distribution map of the rockfalls caused by the earthquake, aspect, distance to rivers, distance to roads, ground strength class, hypocentral distance, shake intensity, slope angle, and slope height in the study area were the initial information layers used in the study (citebagheri predicting 2018). ArcGIS was used to create an occurrence probability map and classify the hazard levels. The MLP and RBF methods were performed with relatively high accuracy. The study showed that Artificial neural network methods make it possible to predict the possibility of rockfall occurrence with a small amount of information (Bagheri et al., 2018).

Liu et al. (2020) used the "ensemble" Random Forest (RF), the "ensemble" Gradient Boosted Regression Tree (GBRT), and the Multilayer Perceptron neural network (MLP) for spatial modeling of shallow landslides in Kvam, Norway. The landslides were triggered by an intensive rainfall event with a duration of three days (Liu et al., 2020). The controlling factors used in the modeling were slope angle, aspect, plan curvature, profile curvature, flow accumulation, flow direction, distance to rivers, saturation, water content, rainfall, and distance to roads (Liu et al., 2020). The findings show that machine learning can successfully predict the spatial extent of shallow landslides when applied to a large, heterogeneous dataset. The GBRT model produced the best results, with an 87 percent prediction efficiency when compared to observed landslides in the area (Liu et al., 2020).

Losasso and Sdao (2018)) conducted a study in which an artificial neural network model was used to create a rockfall susceptibility map. As input parameters, the authors used slope, soil use, lithology, source areas, rockfall niches, elevation, and kinetic energy values, and the results were described as reliable (Losasso and Sdao, 2018). Using LiDAR data, textcitefanos novel 2019 used several hybrid machine learning models to identify rockfall source areas in the presence of other landslides.

A study where an artificial neural network model was used to create a rockfall susceptibility map was conducted by Losasso and Sdao (2018)). Slope, soil use, lithology, source areas, rockfall niches, elevation, and kinetic energy values were used as input parameters, and the authors describe the result as reliable (Losasso and Sdao, 2018).Using LiDAR data, Fanos and Pradhan (2019) used several hybrid machine learning models to identify rockfall source areas in the presence of other landslides. The most effective slope angle thresholds for the source areas were determined using a model, and the most significant conditioning factors were chosen using the Chi-Square method. A probability map was created using the model with the best fit. The models' high accuracy demonstrated that conditional factors derived from LiDAR data could be used instead of geomechanical factors like discontinuity and fractures (Fanos and Pradhan, 2019).

Böhme et al. (2013) compared the Logistic Regression model to the Weights-of-Evidence method for rockfall susceptibility mapping in Sogn and Fjordane County. They came to the conclusion that using Logistic regression with the same controlling parameters results in a susceptibility map that is very similar to the Weight-of-Evidence method but with larger posterior probabilities. With their susceptibility map, they successfully predicted 70

## 2.2 Classification and definition of rockfall

Hungr et al. (2014) proposed a definition of rockfall, which is based on classifications by Varnes (1978), Hutchinson (1989) and Hungr et al. (2001).

Rockfall: 'Detachment, fall, rolling, and bouncing of rock fragments. May occur singly or in clusters, but three is little dynamic interaction between the most mobile moving fragments, which interact mainly with the substrate (path)...'. (Hungr et al., 2014).

The new version of the Varnes classification system proposed by Hungr et al. (2014) is shown in Table 2.1. The classification is based on the type of movement and the type of material. The size of the individual block is not included in this international classification, but rockfall, also known as "steinsprang" in Norway, is commonly defined as rock fragments with a total volume of a few hundred cubic meters. Other types of fragmental mass movements from bedrocks include *"steinskred"* with volumes ranging from 100 to 10,000 $m3$, and *"fjellskred"*, with volumes ranging from 10,000 to 100,000 $m3$ ('Steinsprang og steinskred', 2020).

Table 2.1: Classification of landslides based on the material type "rock", modified from Hungr et al. (2014).

| **Type of movement** | **Rock** |
|---|---|
| Fall | Rock fall |
| Topple | Rock block topple<br>Rock flexural topple |
| Slide | Rock rotational slide<br>Rock planar slide<br>Rock wedge slide<br>Rock compound slide<br>Rock irregular slide |
| Spread | Rock slope spread |
| Flow | Rock avalanche |
| Slope deformation | Mountain slope deformation<br>Rock slope deformation |

## 2.3 Rockfall hazard

Rockfall hazards are defined as the probability that a rockfall event of a given volume will occur in a given area at a given time (Varnes 1984, cited in Delonca et al., 2014). Natural hazards are commonly measured on scientific magnitude and intensity scales. The magnitude of a hazard process is usually inversely proportional to its frequency of occurrence ((Smith, 2013). Smaller rockfall events are more common than larger events, as is well known in the case of rockfall occurrence (Hantz et al., 2016, Douglas, 1980). A power law can be used to describe the magnitude-frequency relationship:

$$F = AV^{-B} \tag{2.1}$$

Where F is the frequency of rockfalls larger than a specific volume V, A is the frequency of rockfalls larger than 1 $m^3$ and B is the scaling exponent (Hantz et al., 2016).

Volkwein et al., 2011 described rockfall hazard in mathematical terms:

$$H_{ijk} = P(L)_j \times P(T|L)_{ijk} \tag{2.2}$$

Where $P(L)$ is the probability of a rockfall event in the volume class $j$, and $P(T|K)_ijk$ is the reach probability. The reach probability is the probability that a rock fragment will reach a specific runout length. $P(T|K)$ is the probability that a block triggered by the same event reaches a location $i$ with intensity or kinetic energy value in class $k$ (Volkwein et al., 2011).

It is common to divide the slope into three zones; the *source area*, the *runout path* and the *runout area* (Figure 2.1).

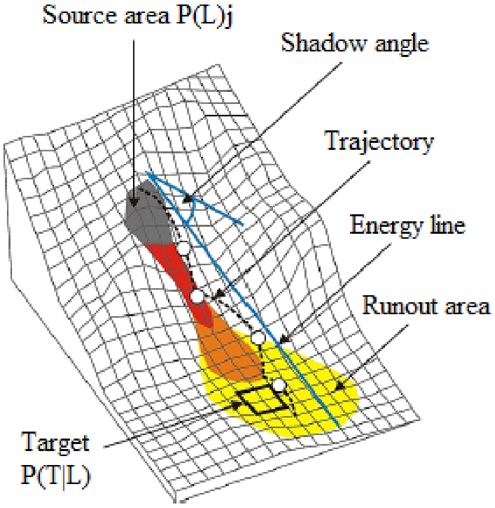

Figure 2.1: Graphic definition of rockfall hazard, modified from Volkwein et al. (2011).

It is difficult to predict where and when rockfall will occur. One issue with this question is that few natural slopes are continuously monitored, and observations of the precise location, size, and time of rockfall events are scarce. Since 1950, the Geological Survey of Norway (NGU), the Norwegian Road Authorities (SVV), BaneNor, and the Norwegian Geotechnical Institute (NGI) have recorded observed mass movements. In Norway, the observations are compiled into a national inventory of mass movements. Inventory of rockfall has also been collected in Canada (Macciotta et al., 2017), France (Delonca et al., 2014), Hong Kong (Chau et al., 2003), and Austria (Sass and Oberlechner, 2012) among other countries.

### 2.3.1 Spatial and temporal distribution

*Rockfall activity* can be detected in the field through observations of vegetation damage (Å ilhán et al., 2013) and other signs of recent rockfalls such as fresh deposits. A conical talus will form beneath a rock wall where there has been or is currently high rockfall activity, and it is a good indicator of the relative spatial distribution of rockfalls in an area. Scars in the terrain and talus slopes can also be detected using aerial photos and high-resolution terrain models. The spatial distribution of recorded rockfall events is skewed toward valleys with population and infrastructure. Typically, events are observed and recorded near roads and railways (Jaedicke et al., 2009,Delonca et al., 2014,Macciotta et al., 2017).

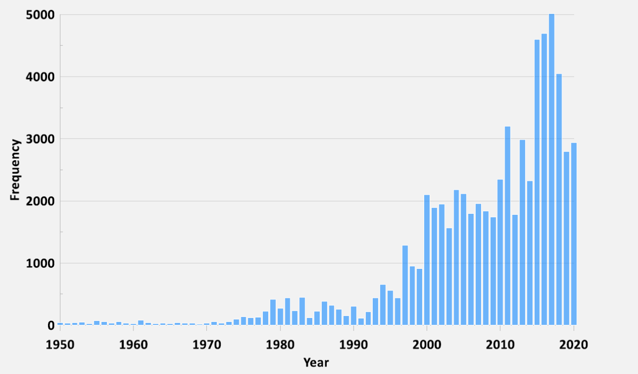

Figure 2.2: The frequency of the mass movements in Norway (Gilbert, 2020)

*The timing of rockfall events* are extremely complex, and we don't yet understand the controls on the temporal occurrence of rockfall events. Lichenometry is a method that has been commonly used to estimate rockfall activity in rock walls for a long time (McCarroll et al., 1998, Grove, 1972). The size and age of the lichen growth on the deposited rockfall fragments are studied in order to estimate the age of the talus slope and if rockfall activity is present. Later estimation of rockfall occurrence frequency is based on observational studies of inventories and statistical approaches. The frequency may be sorted into categorical classes of frequency or quantitative as yearly, seasonal, monthly and, daily frequencies or probabilities.

The number of observed events in Norway clearly increases after 1970, probably because of a systematic registration in the later years that was mentioned in section 2.2. Changed climatic conditions may also be a factor in this increase in observed events (Figure 2.2). This temporal distribution coincides with the Austrian database where there is a general increase in observed events (Sass and Oberlechner, 2012).

Macciotta et al. (2017) conducted a study to quantify rockfall probabilities and their temporal distribution associated with weather seasonality. The study used an inventory database of rockfalls along a railway corridor in the Canadian Cordillera, consisting of 102 rockfall events. A Binomial distribution was used to estimate the probability of rockfall events based on their recorded frequency. The study showed that the dryer months coincided with the months of low rockfall frequency so that the decrease in rockfall occurrences could be explained by less precipitation these months. Increased precipitation in November also coincided with peaks in recorded rockfall occurrences (Macciotta et al., 2017). The minimum rockfall probability was estimated to be in May and July, while the maximum daily rockfall probability was estimated to be in October (Macciotta et al., 2017).

### 2.3.2 Causes of rockfall

Rockfall and other mass movement hazards are common in mountainous areas with steep terrain, but they can occur in a variety of climatic conditions. Rockfalls are most common on slopes steeper than 40 degrees (NVE, 2020), but they can occur on less steep slopes as well. Weathering and crack propagation are examples of conditional factors or preparatory processes that make a slope prone to rockfall. It is also important to consider the orientation and density of cracks and discontinuities in the rock mass. In general, conditional factors are processes that reduce slope stability. They are influenced by both internal factors such as the local geology and external conditions such as meteorology, topography, vegetation cover, snow cover, thermal state, and hydrology.(Matsuoka, 2019), and human activity (Smith, 2013). The removal of vegetation and the increase in slope angle caused by construction activity may reduce lateral support and increase the gravitational forces acting on the slope. It is difficult to distinguish between promoters and mechanisms that initiate rockfall events because a particular process frequently both promotes crack propagation and can be the triggering cause. (L. K. Dorren, 2003). A wide range of rockfall triggering mechanisms has been described in the literature and they are processes near the surface and in the shallow joint systems of the bedrock (Sandersen et al., 1997). They can be meteorological factors, human activities, or seismic activity. Seismic activity as the triggering mechanism for rockfalls in Norway is usually disregarded and will not be further looked into in this thesis. Meteorological factors as the triggering mechanism will be described in Section 2.4.

### 2.3.3 Principles of susceptibility mapping

A susceptibility map's purpose is to predict potential relative unstable zones that are prone to multiple or one specific type of landslide. It does not predict absolute probabilities, but it is a preventive tool used in area planning and areas where detailed hazard mapping, modeling, and mitigation measures are required (Jiménez-Perálvarez et al., 2009). The basis for empirical susceptibility mapping is the assumption that future landslides will occur under the same conditions as in the past.

The Geological Survey (NGU) in Norway developed a national susceptibility map for debris flows and rockfalls in 2009, which is available at Skrednett.no. The map is developed using a Digital Elevation Model of 25 x 25 m resolution and provides which provides a qualitative assessment of the rockfall susceptibility (Derron, 2010). The most commonly used methods for mapping landslide susceptibility are statistical models (Erener and Düzgün, 2010), Böhme et al., 2013, Jiménez-Perálvarez et al., 2009). The potential rockfall source areas in the national susceptibility map are physically determined. All areas with slope angles above 43 $\circ$ are defined as potential rockfall source areas. Areas with slope angles above 34$\circ$ are defined as potential source areas if the terrain is categorized as bare rock (Derron, 2010). The runout length is automatically calculated for each source area, using a 2D extension of the alpha-beta model, an empirical model developed by NGI in 1994 based on known rockfall events in Norway (Lied and Bakkehøi, 1980). However, statistical models are the most preferred methods for landslide susceptibility mapping (Erener and Düzgün, 2010).

### 2.3.4 Factor of Safety

The factor of safety (FS) is an index to describe the stability of a slope (Hoek, 1981). A few geomechanical terms should be introduced before defining the Factor of Safety (FS). Stress is defined as a force, $F$, acting on an area, $A$. We divide the stress vector into two components. Normal stress, $\sigma$, acting normal to the surface, and shear stress, $\tau$, acting parallel to the surface. A rock is assumed to be a Mohr-Coulomb material for all shear failures, where the shear strength $\tau$ is expressed in terms of cohesion $c$ and friction angle $\varphi$ (Wyllie and Mah, 2004). The shear strength of a rock is the amount of stresses required to cause permanent deformation or failure of the rock (Wyllie and Mah, 2004). $\varphi$ is equal to the angle of an inclined plane.

The factor of Safety (FS) is defined as the resisting forces of the slope divided by the driving forces of the slope (Wyllie and Mah, 2004).

$$FS = \frac{Resisting forces}{Driving forces} \tag{2.3}$$

$$FS = \frac{cA + \sum N tan\phi}{\sum S} \tag{2.4}$$

Where $c$ is cohesion., A is the area of the surface, $\sum N$ is the product of the total normal forces, $\sum S$ is the vector sum of the shear forces acting down the plane (Wyllie and Mah, 2004). A $FS > 1$ value indicates that the slope is stable. A $FS \leq 1$ value indicates that the slope is unstable and will fail. If the resisting forces are reduced or the driving forces are increased, a slope can fail. Failure in a slope can thus occur if the resisting forces are reduced or the driving forces are increased. Increasing the slope angle of a sliding plane increases the component of gravity parallel to the slope, the driving forces on a steep slope are greater than the driving forces on a less steep slope. The slope is therefore the most important conditioning factor of instability. The equation for FS will vary for different slopes with different components of driving and resisting forces.

### 2.3.5 Failure modes

*Plane failure* is the most simple, two-dimensional failure mode. It occurs when a block slides on a plane, the sliding plane is then defined by a single discontinuity or weak layer that strikes near parallel to the slope face (Wyllie and Mah, 2004). The dip of the sliding plane has to be greater than the angle of friction of the slope to initiate planer failure (Wyllie and Mah, 2004). Planar failures often occur as large rockslides, but can also occur as individual rockfalls of smaller volumes (Turner and L. Schuster, 2012). The most important factor influencing the rate of movement is friction along the slip surface. Failure can be caused by a decrease in shear strength, an increase in pore water pressure, or a decrease in joint roughness due to weathering (Sandersen et al., 1997).

*Wedge failure* is a more complex, three-dimensional failure mode. The failure occurs when a set of discontinuities obliquely to the slope results in the sliding of a wedge. The sliding occurs along the line of intersection between the two sliding planes that form a V-shaped wedge (Wyllie and Mah, 2004, Turner and L. Schuster, 2012). Wedge failure occurs in a much wider range of geologic and geometric conditions than planar failure. A condition for this failure mode is that the lone of intersection ”daylights” in the slope face, and the dip is steeper than the angle of friction of that slope.

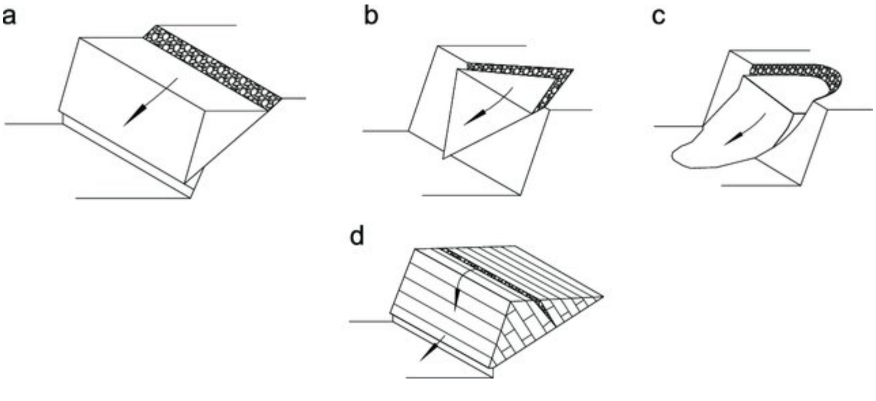

Figure 2.3

*Circular failure* occurs in highly weathered rocks with a high number of fractures, and the individual rock fragments will behave like soil and fail in circular mode (Wyllie and Mah, 2004). The material that slides is defined by a vertical tension crack in the face of the slope or upper surface.

*Toppling failure* is a type of movement where the rock fragment, block, or column rotates forward around a fixed base (Figure2.3, Wyllie and Mah, 2004, Turner and L. Schuster, 2012). It is a common source of rockfalls (Turner and L. Schuster, 2012). Block toppling is when columns of rocks divided by widely spaced orthogonal joints are formed in strong rocks with a second set of discontinuities dipping into the face forming the basal plane. The basal plane of a flexural toppling is not as defined as a block topple, because the discontinuities break as they bend forward. Flexural toppling is often initialized by erosion, sliding, or excavation of the toe of the slope. the toppling then retrogresses backward into the rock mass by the formation of steep tensile cracks (Wyllie and Mah, 2004). Block-flexure toppling occurs in slopes that are divided by numerous cross-joints, the toppling is a result of the accumulation of displacements on the cross-joints. Failure is usually caused by a decrease in cohesion in the toe area of the rock or by a decrease in instability as the center of mass moves outwards (Sandersen et al., 1997).

## 2.4 Triggering factors

This section will focus on triggering factors associated with meteorological conditions, specifically the effects of temperature and precipitation. Meteorological conditions have been identified as the most common category of triggering factors for rockfalls in Norway (Sandersen et al., 1997, Jaedicke et al., 2008, Dyrrdal et al., 2012, Kalsnes et al., 2021). Other well-known potential triggering mechanisms for rockfall occurrence are earthquakes (Luckman, 1976), Bagheri et al., 2018, Kalsnes et al., 2021) the expansion of cracks by tree roots (Collins and Stock, 2016, Kalsnes et al., 2021), and human activities (Kalsnes et al., 2021). Meteorological triggering mechanisms are related to wind, temperature, and precipitation.

Meteorological conditions have a significant impact on rockfall and are frequently discussed (Luckman, 1976, Delonca et al., 2014,D'Amato et al., 2016, Macciotta et al., 2017, Douglas, 1980, Sass and Oberlechner, 2012, Matsuoka and Sakai, 1999, Coutard and Francou, 1989, Rupp and Damm, 2020). However, establishing a common understanding and quantifying the relationship between rockfall occurrence and precipitation and temperature remains difficult. This section will highlight the difficulties regarding the prediction of rockfall events based on meteorological conditions.

### 2.4.1 Ice/rock interaction

The physics of ice/rock interaction related to rock fracture by ice growth is debated in the literature. There are two competing hypotheses (Hales and Roering, 2007). The first hypothesis proposes that the 9 % volumetric expansion of ice forming in pore spaces within the rock increases tensional stress at crack tips, causing the rock to break. The rock fragments are released as a result of the subsequent thawing, resulting in rockfall. This is known as freeze/thaw weathering, and it will be discussed further in the following section.

The second and alternative theory concerns a mechanism known as segregation ice growth. Water migrates through a frozen fringe toward ice lenses, where it accumulates (Hales and Roering, 2007).The stress required to fracture rock is provided by van der Waals and electrostatic forces created at the ice/rock interface. As a result of the increased stress on the fracture walls, a small fracture will form at the crack tip. Water is then drawn towards the point of failure by a chemical potential gradient from warmer parts of the rock (Hales and Roering, 2007).

#### Freeze-thaw cycles

Rockfall occurrences related to freeze-thaw activity are low magnitude, high frequency events which is typical in alpine areas (Hungr et al., 1999, cited in L. K. Dorren, 2003). Rupp and

Damm, 2020 analyzed the spatial and temporal rockfall occurrence of a national rockfall database from Germany, using 670 rockfall events recorded during the past 200 years. The study suggests that rockfall occurs predominantly in the winter months and that freeze-thaw cycles are the major trigger of rockfall in the area (Rupp and Damm, 2020).

The freeze potential (FP) is an index that reflects the ice production assuming constant water-seepage into the rock mass (D'Amato et al., 2016, Matsuoka, 1994). FP for a freeze-thaw episode beginning at $t_0$ can be defined as:

$$\begin{aligned} \text{If} \int {t_0}^t (Tf - T(t))\,dt < 0,\ \text{then FP} = 0 \\ \text{If} \int {t_0}^t (Tf - T(t))\,dt > 0,\ \text{then FP} = \int {t_0}^t (Tf - T(t))\,dt \end{aligned} \tag{2.5}$$

Where $T_f$ is the freezing point of water and $T(t)$ is the temperature of time $t$ (D'Amato et al., 2016). A freeze-thaw episode includes three different types of temperature states (Figure 2.4). (1) Negative cooling, when the temperature is below zero and decreases. (2) Negative warming when the temperature is below zero and increases. And (3) thawing, when the temperature is above zero and FP is larger than zero. The ice is considered as entirely melted when FP is zero (D'Amato et al., 2016). Events with temperatures near 0 °C during the winter season has been categorized as *near zero events* by Dyrrdal et al. (2012).

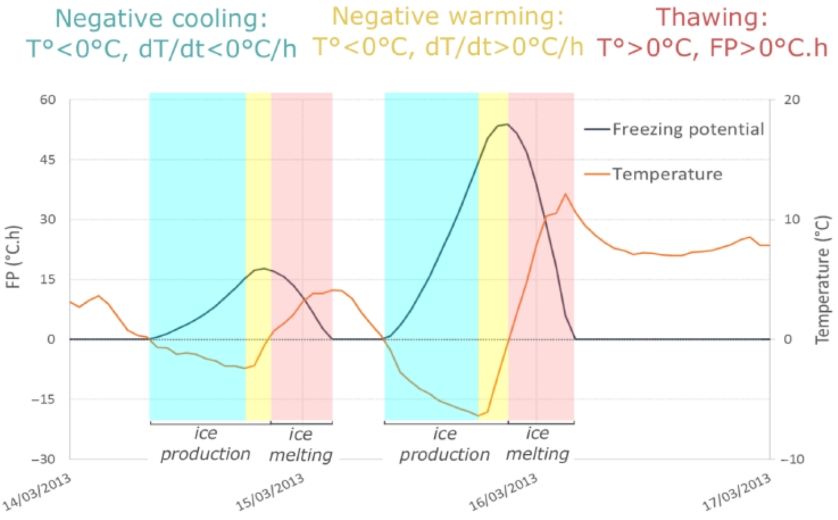

Figure 2.4: Definition of the temperature states in a freeze-thaw episode (D'Amato et al., 2016).

D'Amato et al. (2015) demonstrated in a laboratory study that cooling of rock caused contraction and crack propagation, and that cracks could propagate due to ice expansion. The rockfall does however not occur immediately. Results from Matsuoka and Sakai (1999), D'Amato et al. (2016) and Matsuoka (2019) show that thawing is the cause of more rockfall events than freezing. The rockfall inventory study in D'Amato et al. (2016) show that rockfall occurrence increases with air temperature until FD decreases to zero. A suggestion is that the cohesion of the rock-ice interface holds the rock fragments so that the rockfall event will occur when the ice melts (D'Amato et al., 2016). Rockfall occurrence due to thermal expansion can thus be delayed until the thawing period. Delonca et al. (2014) demonstrate a correlation between rockfalls and the daily minimum temperature for a database from Auvergne, with the largest correlation with the minimum temperature two days before the event.

Rockfall frequency in periods with freezing is quantified as 7 times higher than the frequency in periods with no freezing in D'Amato et al. (2016), 2.4 times higher in Frayssines and Hantz, 2006, 3.9 times higher in Delonca et al. (2014) and between 4-8 times higher in Matsuoka (2019)). Delonca et al. (2014) concluded that they found a ”perfect” correlation between the rockfalls and meteorological factors for 50% of the events. Moen and Humstad (2009) however, suggests that the triggering mechanism of 50% out of 80 observed rockfall events in Oppdølstranda, Vestland County were unknown. They categorized freeze-thaw as the triggering mechanism for 40% of the events and precipitation and snowmelt as the triggering mechanism for 10% of the events.

### Frost-cracking

The alternative theory about frost-cracking is based on the argument that at least 91% saturation in a "closed system" is required to obtain enough force from ice expansion to break rock during the freeze/thaw process. Because unsaturated or open systems are more common in nature, the alternative theory could be applied more easily to natural systems (Hales and Roering, 2007).

Frost-cracking of rocks depends on the time spent within a specific range of subzero temperatures that is known as the frost cracking window (Anderson, 1998). Frost cracking is caused by the crystallization of ice within existing cracks, which results in slow growth of cracks due to ice segregation (Anderson, 1998, Kellerer-Pirklbauer, 2017). The physical process of crystallization of ice in cracks can be compared to the generation of ice lenses in freezing soils (Anderson, 1998, Hales and Roering, 2007). Water migrates along mineral surfaces towards the largest pores or existing cracks, where it freezes (Anderson, 1998). The forces occurring at the rock-ice interface must be larger than the cohesive strength of the rock mass in order for lens growth to occur (Hales and Roering, 2007).

The rate of growth depends on the access to water and the temperature within the rock. Very low temperatures increase the viscosity of water, causing the growth of cracks to slow down at very low temperatures. The optimal temperature range for frost cracking is typically between -3 and -10 , which is the temperature range that is referred to as the ”frost cracking window”. Anderson (1998) investigated the time spent within this frost cracking window as a function of depth. The frost-cracking index was defined as the fraction of year spent within the frost cracking window, modeled by a relatively simple thermal model based on the vertical heat flux within the rock (Fourier's Law) and the radiation balance at the surface at different latitudes. Temperatures at different depths of the bedrock surface were also measured, Anderson (1998) showed that summer daytime temperatures are cooler than the rock surface temperature and the opposite during night. The study also showed that the daytime temperatures during winter are well below the temperature of the bedrock surface.

### 2.4.2 Thawing and thermal stress

Laboratory shear box tests reveal that the strength of an ice-filled crack is a function of normal stress and temperature (Davies et al., 2000). Thawing of ice-filled fractures can lead to a rapid loss of shear strength in the crack. An ice-filled crack that is near thawing has much lower strength than a crack with no ice (Davies et al., 2000, Davies et al., 2001). The factor of safety as a function of temperature shows that the stability of ice-filled discontinuities begins to decrease when the temperature reaches -5 $°C$ ( Figure 2.5). D'Amato et al. (2016) suggest that the ice will start melting at the ice-air interface when a thawing period begins, but not immediately at the ice-rock interface and that the thermal expansion will continue.

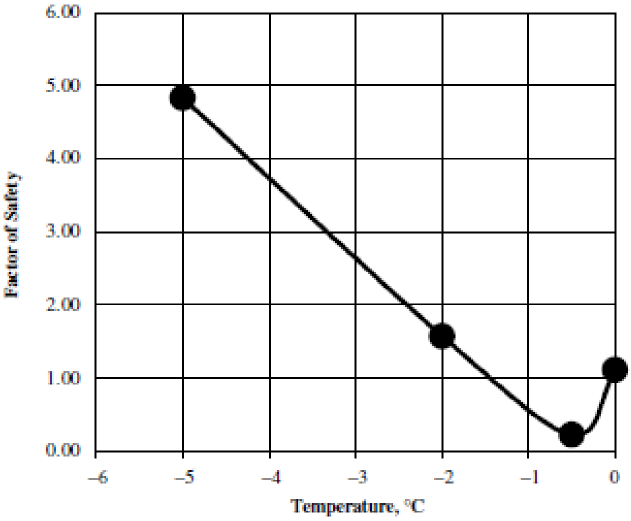

Figure 2.5: The Factor of Safety as a function of temperature in a discontinuity (Davies et al., 2001).

Many rockfalls occur during periods when other triggering factors such as precipitation and freezing conditions are not present, Collins and Stock (2016) did a study to investigate the triggering by cyclic thermal stressing of exfoliation fractures in Yosemite Valley. The study demonstrated that cycles of heating and cooling may lead to deformation and stresses capable of fracturing granitic exfoliation sheets and that both increasing temperatures en temperature fluctuations may promote fracture (Collins and Stock, 2016). This cyclic thermal stressing is related to temperatures that are not common in high latitudes and may not be a cause of rockfall in Norway.

However, "extremely" warm temperatures may also trigger rockfalls in high mountain areas in for example Switzerland and New Zealand (Allen and Huggel, 2013). Allen and Huggel (2013) showed that 67% of rockfall and rockslide events in the Swiss Alps were related to extremely warm days in the week prior to failure. The triggering were related to rapid thawing and snowmelt (Allen and Huggel, 2013).

Kristensen et al. (2021) discussed the failure of the Veslemannen rock slope in 2019 and showed that the sensitivity of the slope to precipitation was related to ground temperatures. The failure happened after several years with accelerated movement related to precipitation events, but the accelerations occurred exclusively during late summer and fall. This suggested that the influence of possible permafrost and deep seasonal frost strongly influenced the seasonal variation in the timing of acceleration events. A frozen layer prevented water to reach the sliding zone earlier in the season (Kristensen et al., 2021). This phenomenon can explain slope failure in periods of warm temperatures in areas with deep seasonal frost.

### 2.4.3 Intense rainfall episodes

The effects of precipitation as a triggering mechanism are uncertain. Rainfall may contribute to the release of rockfalls in autumn by decreasing internal friction between slip planes in the bedrock, causing high hydrostatic pressure in joints, and facilitating the thawing of ice after frost bursting (Rapp, 1960). While Matsuoka and Sakai (1999) suggested that no obvious relationship between the number of rockfalls and the number of precipitation events was observed in their study.

Intense rainfall episodes is commonly suggested as a triggering mechanism for rockfall (Krautblatter and Moser, 2009, Delonca et al., 2014, Matsuoka and Sakai, 1999, D'Amato et al., 2016, Matsuoka, 2019). D'Amato et al. (2016) defined that a precipitation event starts when it begins to rain after a given length of time without any precipitation (D'Amato et al., 2016). The length of the time period without precipitation should be chosen so that each rainfall episode is independent. A period of two days without precipitation was selected as a minimum between precipitation episodes for late spring/summer and four days for the other seasons in Italy (Brunetti et al., 2010). Intense rainfall episodes increases the water pressure in joints and cracks in the shallow bedrocks, causing the release of rockfalls due to the pressure or lubrication of joints (Matsuoka, 2019). The direct influence of precipitation begins when the rain falls on the cliff, but the water that goes through soil and rock to reach the cliff surface has to be taken into account. D'Amato et al. (2016) assumed, after field observations, that the rainwater has entirely flown off the cliff after 25 hours.

A study by Krautblatter and Moser (2009) in the German Alps showed that rockfall intensity is only coupled with rainfall intensity above a certain threshold of 9-13 mm per 30 minutes and that the relationship is highly nonlinear. A study by Delonca et al. (2014) confirmed a positive correlation between rainfall and rockfall events in one of the low-frequency databases and a correlation between cumulative rainfall and rockfalls in the other low-frequency database.

Table 2.2: Summary of studies related to rockfall occurrence and meteorological factors. Modified from D'Amato et al., 2016.

| **Author** | **Country** | **Elevation [m.a.s.l]** | **Collection method** | **Duration [years]** | **Main results** |
|---|---|---|---|---|---|
| Luckman (1976) | Candada | 1800-2500 | Direct observations, deposit observations | 8 | Diurnal occurrence of rockfall. Max in spring and during storms in the summer |
| Douglas (1980) | Ireland | 0-100 | Collection of rock debris on square | 4 | Correlation between number of freeze-thaw events and RF and % of period below 0 degrees and RF. |
| Sandersen et al. (1996) | Norway | 0-2400 | Newspaper report | 1 | Continental climate: Higher activity during snowmelt season. Marine climate: Higher activity during autumn. Many RF not correlated with weather. |
| Matsuka and Sakai (1999) | Japan | 2800 - 3200 | Rock debris on snow | 14 | Max RF activity about 10 days after seasonal thawing. No correlation with precipitation or diurnal frost cycles. |
| Chau et al. (2003) | Hong Kong | 0 - 957 | Deposit on human infrastructures | 15 | Influence of rainfall, lower threshold of daily rainfall 150-200 mm. |
| Frayssines and Hantz (2006) | France | 200-2000 | Historical inventory | 34 | Influence of freeze-thaw cycles, slight influence of rainfall. |

| | | | | | |
|---|---|---|---|---|---|
| Krautblatter and Moser (2008) | Germany | | Measurements of rockfall deposits in collectors | 4 | Rockfall intensity is coupled to rainfall intensity above a threshold (9-13 mm/30 min). The response of rockfall to rainfall intensity above the threshold is highly non-linear. |
| Humstad (2010) | Norway | 0 - 200 | Historical inventory | 11 | Freeze-thaw is suggested as triggering for 34% of RF, freeze-thaw and rainfall as 5% and rainfall as 11%. 50% of RF events has unknown trigger. |
| Mateos et al. (2012) | Majorca Islands | 200-700 | Deposits on roads | 2 | Influence of intense rainfall 90 mm per 34 hours. Influence of antecedent rainfall over 800mm, and freeze-thaw cycles. |
| Delonca et al. (2014) | France | 0- 200<br>300 - 400<br>700 - 900 | Deposit on railway network | 0.3 to 1.4 | Reunion: Correlation with rainfall<br>Burgundy: Correlation with rainfall<br>Auvergne: Correlation with daily minimum temperature |
| Collings and Stock (2016) | USA | | Field monitoring | 3.5 | Cycles of heating and cooling lead to stresses capable of fracturing granitic exfoliation sheets. |
| D'amato et al (2016) | France | 800 - 1300 | TLS and photographic survey of scars | 2.4 | Highest rockfall frequency during freeze-thaw episodes, especially during thawing. Secondary influence of rainfall. |
| Kellerer-Pirklbauer (2017) | Austria | 190 - 2725 | Monitoring of rock temperature data | 9 | The number of freeze-thaw cycles affect the frost shattering of near-surface rock (10's of cm). A higher number of cycles in sun-exposed rock walls. |

| | | | | | |
|---|---|---|---|---|---|
| Matsuka (2019) | Japan | 2900 | On-site-time-lapse images and monitoring of meteorological conditions | 6 | 4-8 times higher RF rates in winter than in summer. Heavy precipitation trigger rockfalls probably because of raised water pressure in rock joints. Intermediate rainfalls in late autumn and spring followed by shallow freezing and rapid thawing are causing RF. Deep seasonal freezing to about 5 meters enables the release of RF during seasonal thawing in late spring and early summer. Short-term large thermal fluctuations during winter may produce cyclic thermal stress that triggers RF. |

## 2.5 Machine Learning

### 2.5.1 Definitions

Machine Learning is the field of science that describes how to program computers so that they can learn from data (Géron, 2019). The goal is to develop algorithms that are capable of automatic learning (Mehta et al., 2019). It was already defined by Arthur Samuels in 1959 as '*The field of study that gives computers the ability to learn without being explicitly programmed*'(cited in Géron, 2019). Arther Samuels is recognized as a pioneer in the Machine learning field, he successfully programmed or *"learned"* a computer to play a better game of checkers than the person who wrote the program (Samuel, 1959).

A new, more formal definition was suggested by Tom Mitchell in 1997: '*A computer program is said to learn from experience E with respect to some task T and some performance measure P, if its performance on T, as measured by P, improved with experience E.*' (Tom Mitchell, 1997).

Statistical methods and machine learning methods can be difficult to distinguish. The main concern of the method distinguishes Machine Learning from statistics. The primary concern or goal of machine learning is to correctly predict unobserved, out-of-sample data points, whereas statistics' primary concern is fitting the model (Mehta et al., 2019).

### 2.5.2 Defining the learning problem

A machine learning problem seeks to discover a pattern or structure in a set of data and then use that pattern to make predictions on previously unseen data (Kuhn, 2013). Depending on whether the output to be predicted is numerical or categorical, the learning problem is referred to as a regression problem or a classification problem. Determining whether a pixel is a rockfall source area is a binary classification problem with two possible categorical outcomes: "rockfall," which represents rockfall source areas, and "no rockfall," which represents areas that are not susceptible to rockfall occurrence.

The basic assumption of the empirical machine learning approach is that future events of interest are likely to occur in similar conditions as in the past (Fanos and Pradhan, 2019).

The learning problem can thus be expressed as a set of $p$ features, $X = (X_1, ..., X_p)$ and a target variable $Y$, where the aim is to find some statistical relationship or pattern from the data. The "learned" relationship may be expressed mathematically as a function, $f$, which can be applied on unseen data $X'$ to make predictions $\hat{Y}$ (Hastie et al., 2009):

$$\hat{Y} = f(X') \tag{2.6}$$

Geological or meteorological parameters may be useful for classifying rockfall source areas and thus make up the $p$ features. For the learning problem of rockfall source area classification, is target variable $Y$ either "rockfall" or "no rockfall". To train the model, a dataset with observed, true labels (e.g., rockfall or no rockfall) can be used. The learning process of machine learning will be described in the following section.

### 2.5.3 Supervised learning - the training process

Supervised learning is a learning process in which the machine learning algorithm is given input data and true labels (the training set) to help it "learn." For example, Labels could be 0 or 1, representing either rockfall source areas or not rockfall source areas. The machine-learning algorithm then identifies patterns present in the data and uses labels to "learn" from this knowledge. The algorithm compares predicted outcomes to the actual, observed outcomes to identify errors n the predictor and change the model by adjusting its parameters so that the model best fits the training set (Saravanan and Sujatha, 2018, Géron, 2019). The aim of the training process is to minimize the cost function for the algorithm.

*Gradient Descent* is a popular optimization strategy in machine learning (Géron, 2019). The technique iteratively changes the parameters (also known as weights) to minimize a cost function. The cost function is a measure of the prediction error in terms of the model's ability to estimate the relationship between the outcome and the input features. It displays the difference between the predicted and observed values. The Gradient Descent method begins with a random selection of initial model parameters, followed by measuring the local gradient of the cost function to ensure that the next learning step is in the direction of descending gradient. The parameters are changed with each step, with each step attempting to decrease the cost function until the algorithm converges to a minimum (Géron, 2019). Because not all cost functions are bowl-shaped with one minimum (Figure 2.6a), the main challenge with Gradient Descent is to find the global minimum rather than the local minimum (Figure 2.6b).

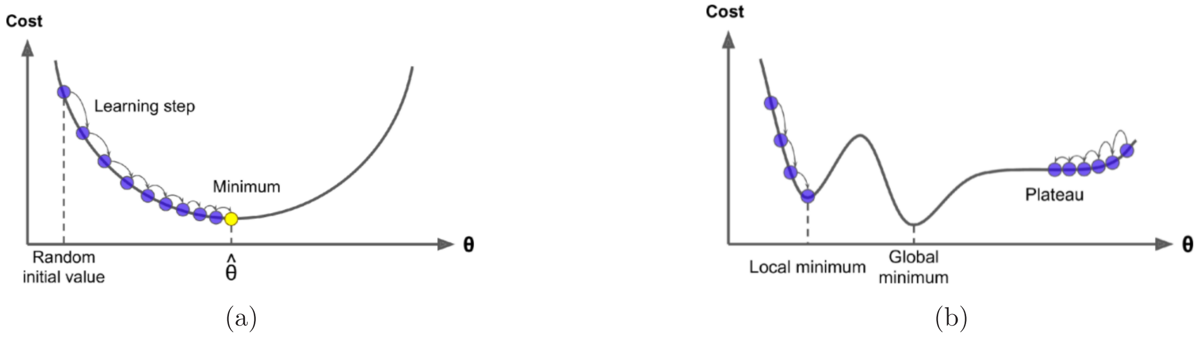

(a)

(b)

Figure 2.6: Illustration of the Gradient Descent strategy Géron (2019).

### 2.5.4 Evaluation of model performance with Cross-Validation

The model should be able to predict unseen or "Out-of-the-bag" data and should be calibrated through training and testing. The model should thus be "generalized" and not over-fitted to the data it is trained on. It is common to "hide" a part of the available data until the model is ready to evaluate its performance on unseen data. Performance metrics (Section 2.5.5), comparing predicted outcomes to actual outcomes, are then used to evaluate the model performance.

Multiple approaches can be used when splitting the data. One method is to split the data into a training and test set. This method is often referred to as the ”Hold-out” method. The risk of overfitting will still exist with this method, and it is difficult to evaluate how the model will perform on unseen data using only one test set. The performance of the model may be dependent on the size and values in the test set, and the test set will not be complete ”Out-of-the-bag” when it is involved in tuning the hyperparameters of the model (Section 3.2.9). Another method is splitting the data into three sets; training, testing, and validation. The disadvantage with this method is that there are fewer data left for training the model.

A widely used method that combines these two methods is *Cross-Validation (CV)*. Cross-validation can be implemented to eliminate the risk of overfitting even further without reducing the size of the training data and is the most widely used method for estimation of prediction error (Hastie et al., 2009). The held out sub-sample of the data is referred to as the *validation set*, which will be used to test the performance of the final model. The rest of the data are used for training and tuning with Cross-validation, and are referred to as the *calibration set*.

K-fold Cross-Validation (KCV) is an iterative CV technique where the training data is split into $K$ parts or *folds*. The model is trained through $K$ iterations (Hastie et al., 2009), where one *fold* is held out as the test set for each iteration. The $K$ evaluation scores are summarized, and the mean of the set of $K$ scores is used as the model's performance score. The results from the k-fold CV can be used to study the variability of the performance based on how the test set is chosen (Kuhn, 2013). The standard deviation will tell how much the scores are varying with each iteration.

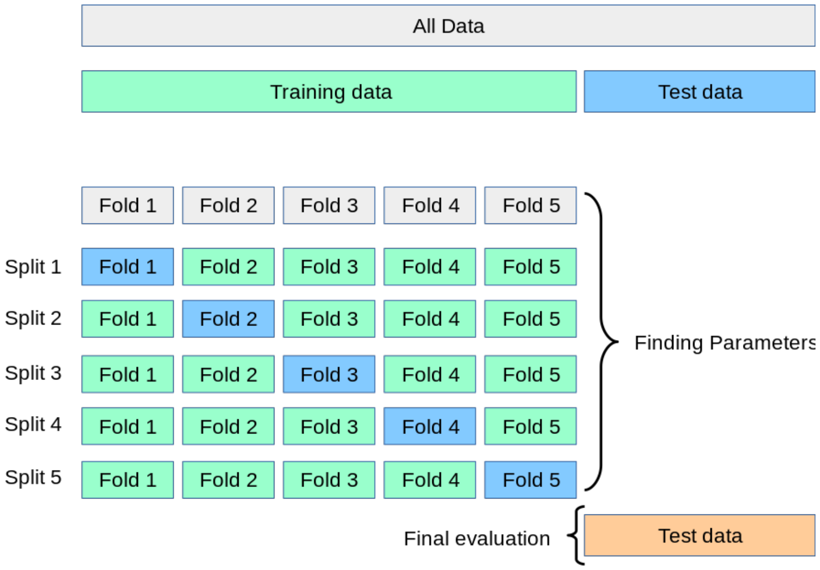

Figure 2.7: Illustration of model evaluation with a 5-fold Cross Validation `Scikit-learn` documentation.

### 2.5.5 Evaluation metrics

Model performance is evaluated by comparing predicted outcomes with observed outcomes (Géron, 2019,Kuhn, 2013). The confusion matrix represents the four possible outcomes of a prediction for a binary classification problem (Figure 2.9). True positive (TP) prediction refers to a correctly classified prediction in the positive class, and true negative (TN) predictions are correctly classified in the negative class. The true positive and true negative predictions make up the correct predictions.

False negatives (FN) are predictions that belong in the positive class but are classified in the negative class. False positives (FP) are predictions that are incorrectly classified as the positive class when they belong in the negative class. The false negative and false positive predictions make up the incorrectly classified predictions. The confusion matrix shows the number of correctly and incorrectly classified pixels and the class to which they belong compared to the class they were classified. In the binary classification of rockfall source areas, the positive class is defined as rockfall source area pixels, while the negative class is defined as no rockfall pixels.

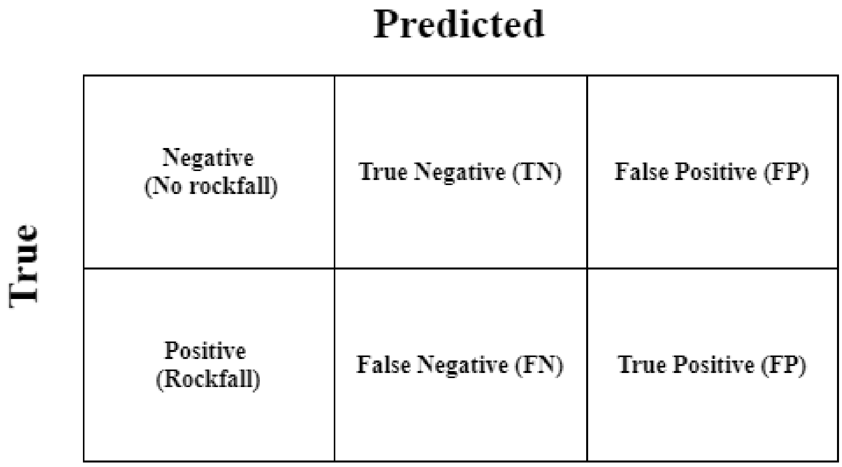

|  |  | Predicted |  |
|---|---|---|---|
| True | Negative (No rockfall) | True Negative (TN) | False Positive (FP) |
|  | Positive (Rockfall) | False Negative (FN) | True Positive (FP) |

Figure 2.8: The confusion matrix for a two-class problem ”Rockfall” or ”No rockfall”.

Evaluation metrics are defined based on these four prediction outcomes represented in the confusion matrix. For the classification problem to predict rockfall source areas are ”rockfall” denoted as the positive class and ”no rockfall” as the negative class. The outcomes of the true positive and true negative are the correct predictions, while false positives and false negatives are not correctly predicted. Accuracy (ACC), F1 score (F1), precision (P), recall (R) and the ROC curve can be used to evaluate the classification algorithms.

Accuracy measures the proportion of correctly classified predictions to the total number of predictions. (Liu et al., 2020):

$$ACC = \frac{TP + TN}{TP + FP + TN + FN} \tag{2.7}$$

Precision is a ratio that expresses how well the classifier classifies true positives in comparison to the total number of positive predictions:

$$P = \frac{TP}{TP + FP} \tag{2.8}$$

Recall is defined as the ratio of correctly classified instances in one class to the total number of instances in the class (Géron, 2019, Derczynski, 2016). Recall is also known as the True Positve Rate (TPR) or sensitivity (Géron, 2019).

$$R = \frac{TP}{TP + FN} \tag{2.9}$$

F1 score can be defined by precision, $P$ and recall, $R$ (Derczynski, 2016, Géron, 2019) and is defined as:

$$F1 = 2 \times \frac{P \times R}{P + R} \tag{2.10}$$

The F1 score balances precision and recall equally and ranges from 0 to 1, where 1 is the ideal score and indicates a perfect model. Because it is the harmonic mean of the two metrics, a classifier will only get a high F1 score if both recall and precision are high (Géron, 2019). The receiver operating characteristics (ROC) curve is obtained by plotting the True Positive Rate (TPR or recall) against the False Positive Rate (FPR). The area under the ROC-curve (AUC), which ranges from 0 to 1, can be used to compare the performance of models. A perfect classifier has an AUC of one, whereas a random classifier has an AUC of 0.5 (Géron, 2019).

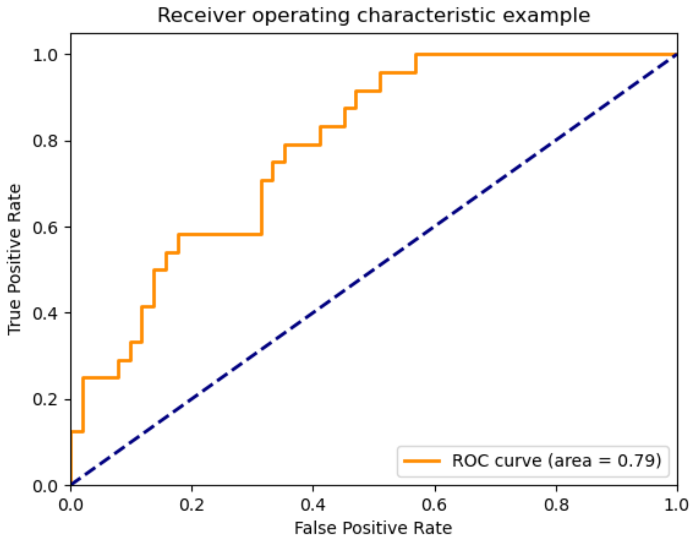

Figure 2.9: An example of the Receiver Operating Characteristics (ROC) curve from `Scikit-learn` documentation.

# Chapter 3

# Data and Methods

## 3.1 Setting

### 3.1.1 Climate and natural hazards in Vestland County

Vestland County has a land area of approximately 33 870,98 $km^2$. The County was formed on January 1st, 2020, and includes the previous Counties of Hordaland and Sogn og Fjordane. There are considerable differences in climate between local areas in Vestland County. Parts of the County are coastal areas with a maritime climate with mild temperatures and large amounts of precipitation. Other parts of the County are midland, with a continental climate and small amounts of precipitation (The Norwegian Meteorological Institute, 2021). The mean winter temperature is around 0 °C in coastal areas, while it is considerably lower in high mountain areas and inner valleys. Yearly precipitation varies between 500 mm in inner valleys and 3500 mm near the coast (The Norwegian Meteorological Institute, 2021).

The mean annual temperature in Vestland is estimated to increase by approximately 4 °C considering the climate changes. The increase in temperature will be highest for autumn and winter and lowest for summer. During winter, extremely low temperatures will become rare, while extremely warm temperatures will become more common during summer. The annual precipitation is estimated to increase by 10 to 15 % for all seasons, with differences throughout the County. Autumn is estimated to have the most significant increase in precipitation. The amount of snow is estimated to decrease in coastal areas drastically but increase in higher mountain areas until a further increase in temperature in the latter part of the century.

Data from the national rockfall inventory (Section 3.1.4) shows that the frequency of rockfall events is highest in December, January, February, and March and lowest in June, July, and August (Figure 3.1).

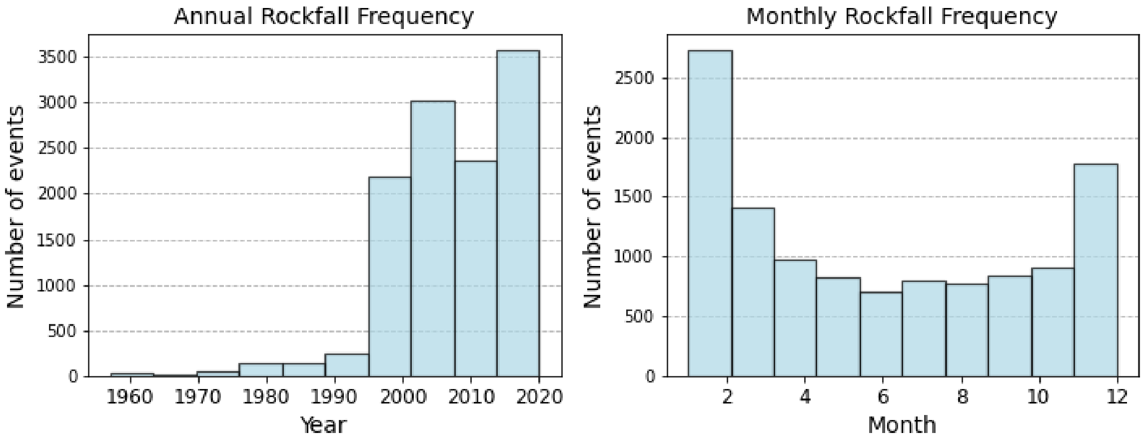

Figure 3.1: Annual and monthly frequency of rockfall in Vestland County. Data from the national rockfall inventory (Skrednett.no).

### 3.1.2 Training area for ML models

The training area consists of two municipalities in Vestland County, Norway; Lærdal and Aurland. Vestland County (earlier Sogn og Fjordane and Hordaland) has a maritime climate with mild winters and temperatures depending on altitude and distance-to-coast. Lærdal and Aurland are in the innermost part of the county, but are close to two branches of Sognefjorden. Fjords, valleys with river deltas, and steep slopes characterize the area.

The area of Lærdal and Aurland municipalities are 1,343 and 1,568 $km^2$ respectively (Figure 3.2). The two municipalities have approximately 3906 residents distributed in the small towns of Lærdalsøyri, Aurlandsvangen, Vassbygdi, Flåm, Undredal, and Gudvangen. Several studies about rock slope instabilities have been conducted in Vestland County (Böhme et al., 2013, Blikra et al., 2006). The area is affected by post-glacial gravitational slope failures and current slope instabilities, resulting in multiple potential rockfall source areas and both active and non-active talus slopes (Böhme et al., 2013). Rockfall and other landslide deposits are highly visible in the area. Rockfall in the area may potentially affect transportation routes, private houses, and public buildings. The most common consequence of rockfall events is temporary road closing, but property damage and causalities also occur. An example of a recent known rockfall event that could have had extensive consequences is the 17th of March 2003 where two rock fragments of 3 $m^3$ were deposited in the garden of a private farmhouse (Hefre et al., 2016).

The bedrock in the area is primarily variations of gneiss, with some overlaying phyllite and rocks from Jotun/Valdresdekket. Gabbro and amphibolite are examples of such rocks. The crush zone in the transition between the basement, the overthrust sheet, and faults of Jotundekket may be the origin of rockfall and rock-slides in the area (Hefre et al., 2016). The area is relatively dry, with annual precipitation of 510 mm in Lærdal (**kss**) and 685 mm in Aurlandsvangen (Sandersen, 2015). Hefre et al. (2016) made a summary of climate elements for Lærdal, based on available data from the Norwegian Meteorological Institute. The maximum daily precipitation in Lærdal was 60 mm from 1953 to 1996 and the annual mid-temperature 5.6 ° C . Snow will often accumulate in higher elevations despite the mild winters, causing runoff from snowmelt during spring. The precipitation also increases up to 50 % in the high-elevation areas compared to sea level.

The decision to use municipality borders was made to obtain some homogeneity in the data. Although, it is impossible to reach perfect homogeneity because different individuals made the registrations of rockfall impacts. It is also common to investigate a constricted area such as a municipality or a county for a hazard assessment and susceptibility mapping in Norway (Böhme et al., 2013,Erener and Düzgün, 2010).

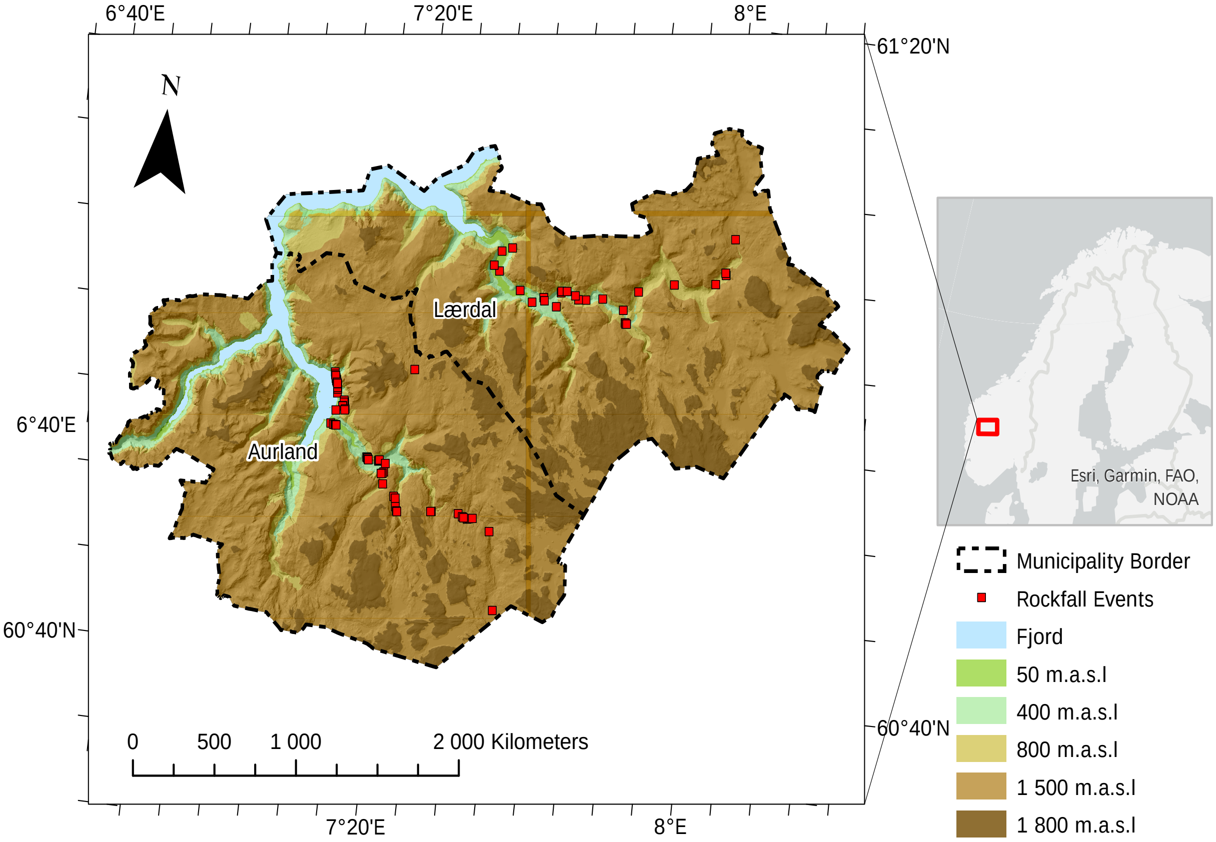

Figure 3.2: Study area and the selected rockfall events. The map is made from a 10 x 10 m DEM layered over a hillshade in ArcGISPro. The DEM is from hoydedata.no (Kartverket, 2020).

### 3.1.3 Fieldwork

Fieldwork was carried out to gain an understanding of the geological setting in the area. This thesis is part of a larger project in Norway on various aspects of rockfall. As a result, the fieldwork was carried out in collaboration with another student (Morken 2021, in prep) in June 2020. Inspections of eight different locations with talus slopes and release areas yielded useful information about the training area. Although roughness data for four talus slopes were collected, it was not used in this study. Another survey was carried out between October 13th and October 15th, 2020. The goal was to take a closer look at the release areas at the June locations. Both release areas and talus slopes were photographed during a helicopter flight. Field observations, which are extremely useful in the field of natural hazards, can provide a broader perspective on a research question.

### 3.1.4 Rockfall inventory

The Norwegian national rockfall inventory database can be found at www.Skrednett.no. The database contains 35845 rockfall events observed in Norway from 1950 to the present. Other

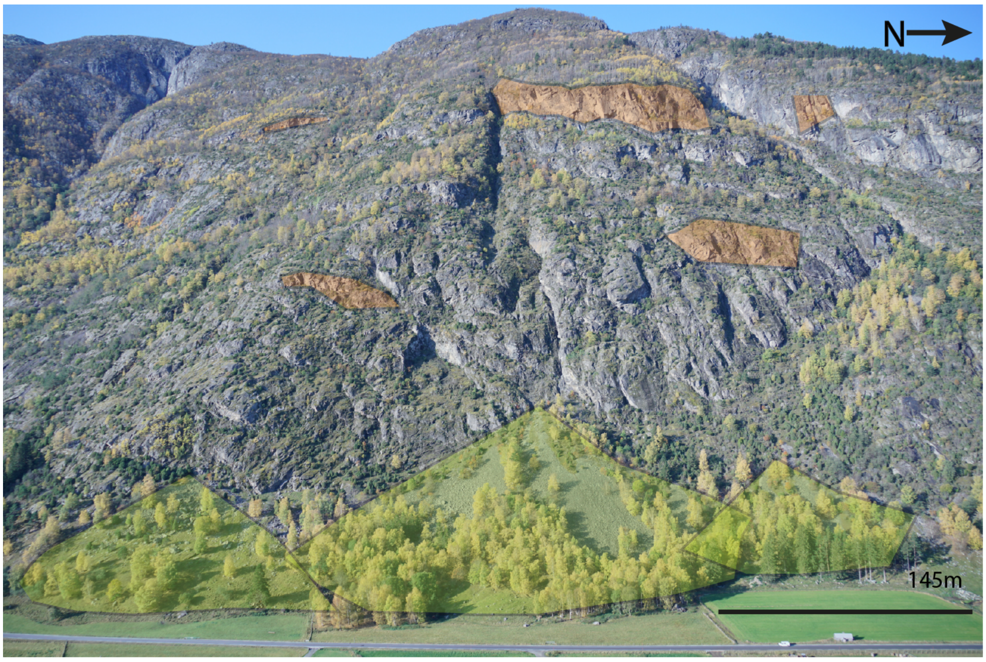

Figure 3.3: Overview picture of a typical area with a talus slope and steep rock wall with multiple potential rockfall source areas in Lærdalen. Some of the most apparent unstable rockfall source areas showing potential loose blocks are marked in orange. Three talus slopes are marked in green. Photo by: Lin Alexandra Emhjellen.

geohazards such as snow avalanches, rockslides, and debris slides are also recorded in the database. The Norwegian Public Road Administration, The Norwegian Geotechnical Institute (NGI), The Geological Survey of Norway (NGU) and BaneNor have contributed to the inventory. NVE's RegObs app allows the general public to register observations. For this study, rockfalls with codes 110 (unspecified volume) and 111 (up to 100 $m3$) have been extracted for Vestland County. All rockfalls registered between 1961 and 2020 are included in the extracted database.

All extracted events include the impact's location coordinates and the date (year, month, day). Other columns, such as comments on infrastructure damage, are possible to register but are not extracted for this thesis because this information is lacking for most events. For the training of the machine learning algorithms, 95 events observed in the study area Lærdalsdalen and Aurlandsdalen were chosen. In the meteorological analysis, 1355 events were used.

## 3.2 Machine Learning - Data and Methods

The focus of the thesis is applied machine learning for rockfall source area prediction, this section will therefore describe how the different algorithms work in general and how they were used. Detailed descriptions of how the predictions are calculated are excluded due to the scope of the project and time constraints. Three ML algorithms were trained to predict rockfall source areas; Logistic Regression, Random Forest, Gradient Boosted Regression Tree, and Multilayer Perceptron. It is a common approach in applied machine learning to test different algorithms and choose the best predictor based on the results (Géron, 2019).

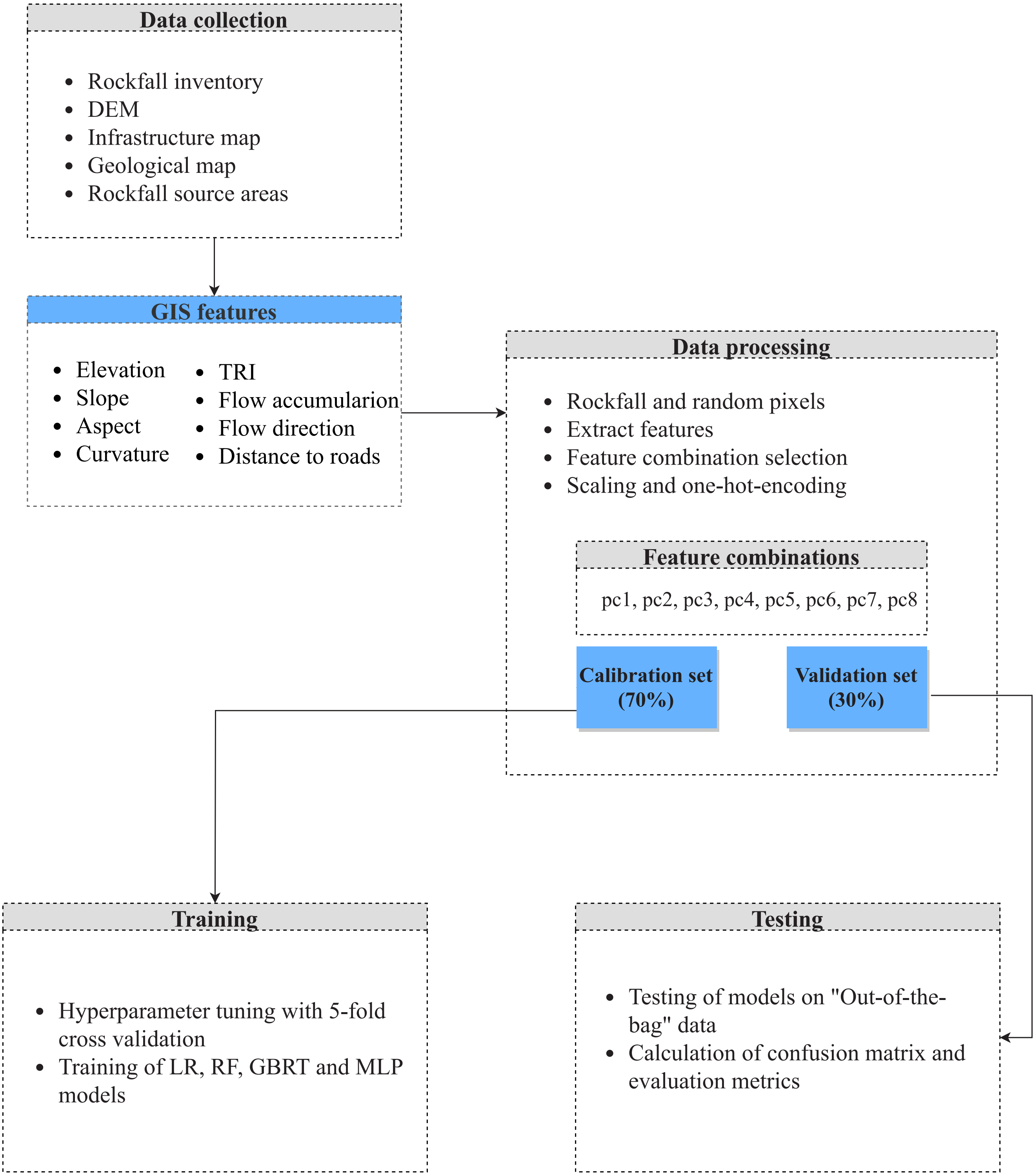

Figure 3.4: The workflow of the machine-learning methodology.

### 3.2.1 GIS data

A DEM (DTM10, 13.04.2021) of 10x10 m resolution from Hoydedata.no (Kartverket,2021) was used to generate relevant topography features in ArcGISPro (2.7.1). Elevation, Slope, Aspect, Plan Curvature, Profile Curvature, TRI, Flow Accumulation, Solar Radiation, and Distance To Roads were calculated using built-in tools (Table 3.1). The elevation is interesting because the spatial distribution of rockfalls is often denser in mountainous areas. The slope angle is considered one of the most important conditional factors for rockfall. Aspect, the slope direction, was chosen as an input feature because it determines the exposure to solar radiation, wind, and precipitation. This feature may affect the stability of the slope and is also interesting concerning precipitation and temperature as triggering mechanisms. Profile Curvature is parallel to the direction of the maximum slope angle and indicates if the slope is upwardly concave or convex at that cell. Plan Curvature is perpendicular to the direction of the maximum slope angle and indicates if the surface is sideward convex or concave at that cell. The curvature factor influences erosion and deposition because of the acceleration and deceleration of downslope flows (Fanos and Pradhan, 2019). Flow accumulation determines the accumulated flow into each cell (Liu et al., 2020). It is relevant because of the potential effect of water accumulation in faults and joints. Distance To Roads is relevant because removal of vegetation, external loads, and excavations are processes that occur on slopes near roads and can affect slope stability (Fanos and Pradhan, 2019, Liu et al., 2020).

TRI was calculated by the method developed by Riley et al. (1999) and expresses the elevation difference between neighboring cells:

$$TRI = \gamma \left[ \sum (X_{ij} - x_{00}^{2} \right]^{1/2} \tag{3.1}$$

Where $\gamma$ is the digital elevation model and $x_{ij}$ is if the elevation of each neighbor cell to cell (0,0) (Riley et al., 1999).

Table 3.1: Description of tools used in ArcGISPro 2.7 to extract the input features.

| **Feature** | **Unit** | **Spatial Analyst tool** | **Description** |
|---|---|---|---|
| Elevation | m.a.s.l | - | Elevation is the cell value of a surface raster (DEM). The national 10 x 10 DEM from Hoydedata.no was downloaded 13.04.2021.~ |
| Slope | Degrees | Slope | The gradient from each cell of a raster. Calculated from the 10 x 10 m DEM with the planar method.<br>The slope is defined as the maximum rate of change in value from a cell to the neighboring cells.<br>A 3 by 3 cell neighborhood is used. The slope value is calculated with a third-order finite-difference estimator.~ |
| Aspect | Degrees ( 0 - 360) | Aspect | The downslope direction of the maximum rate of change in value from a cell to its neighboring cells (slope direction). The value of each cell is the compass direction, measured clockwise from 0 to 360. A 3 by 3 cell neighborhood is used<br>and the direction of the plane is the aspect for the center cell. 0 and 360 is north, flat is denoted as -1. (Burrough, P. A~ |
| Curvature | (1/100) of a z-unit. | Curvature | The second derivative value of the 10 x 10 m DEM. A fourth-order polynomial are for for each cell in a 3 by 3 cell neighborhood.<br>~Curvature is the combination of profile and planform curvatures. The profile curvature is parallel to the slope, the planform curvature is perpendicular to the direction of the maximum slope.~ |
| Terrain Rougedness Index (TRI) | m | Raster Calculator | Calculated from the equation by Riley et al. 1990.<br>The equation in Raster Calculator: mean(DEM) - min(DEM) / max(DEM) - min(DEM) |
| Flow Accumulation | Number of cells | Flow Accumulation | Uses the Flow direction raster as input. Calculated the accumulated weight of all cells flowing into each downslope cell.<br>The default weight is 1 for each cell. The value in each cell in the output raster is the number of cells that flow into that cell.~ |
| Distance To Roads | m | Euclidean Distance | The Euclidean distance is calculated for each cell to the closest source cell with the planar method.<br>~The input source data is a feature class with the name N50_SamferdelsLinje. The output is a raster with 10 x 10 m cell size.<br>Cell size can be defined in the tool.~ |
| Bedrock | Categorical | - | Feature class: Berggrunn N250 from NGU. Scale is 1:250 000. |

### 3.2.2 Mapping of release areas

The coordinates registered in the inventory database for each rockfall show the location where the rocks are deposited. The slope angle was calculated using a DEM with a resolution of 1x1 m. It was also used to investigate the topography visually. A slope angle map, DEM topography, and aerial photos were used to map the source areas. The aerial photographs can be found at *Norgeibilder.no*, a collaboration between the Norwegian Public Roads Administration and the Norwegian Institute of Bioeconomica (NIBIO). The aerial photos from NorgeiBilder freely available for the area are from 1971, 2007, 2008, 2013, 2014, and 2019. Photos from immediately before and after the event would ideally be compared, but that was not possible due to the sparse temporal resolution of the available aerial photos. The release area polygons were divided into 10 x 10 m resolution pixels to represent ”rockfall” source areas. Random pixels were generated in ArcGISpro (2.7.1) to represent ”no rockfall” areas. All features were then extracted to each pixel.

### 3.2.3 Software

The programming language Python was used to implement all methods. Python is one of the most popular high-level programming languages for scientific computing, and it is Open-source. The Python module `scikit-learn` (version 0.23.1) was used for the machine learning algorithm for the spatial analysis. `Scikit-learn` provides several machine learning functions for both supervised and unsupervised problems, submodules for cross-validation, evaluation, and visualization. The module is based on Numpy, Scipy, and Cython (Pedregosa et al., 2011). The Python module `Statsmodels` (version 0.12.2) provides functions for different statistical models and was used for the logistic regression in the meteorological analysis.

Scripts developed for this study can be found here in this GitHub repository:

`https://github.com/Emhjellen-UiO/Emhjellen_masteroppgave.git`

### 3.2.4 Data preparation

It is common to use binary values for the target variable in ML, and 1 was selected for ”Rockfall’ pixels and 0 for ”No rockfall” pixels (Table 3.2). Bedrock is a categorical value and was converted into numerical values by one-hot encoding. One hot encoding makes a new feature for each categorical value, and the numerical value 1 is coded for the correct category and 0 for all others (Figure 3.6). The aspect was also converted from degrees to categorical values and then one-hot encoded. Data preparation before using it in machine learning also includes cleaning the dataset for missing values, dividing it into a calibration set/validation set, and scaling the data. 70 % of the data were selected as the calibration set and 30% the as the validation set using the Test-Train-split method in `scikit-learn`. The exact ratio between calibration and validation was used by Liu et al. (2020) in their study on modeling of shallow landslides with machine learning algorithms.

The data were scaled using the standardization approach, even though it is not required for Random Forest and Gradient Boosting Regression Tree. This method transforms the data to zero mean and unit variance (Choi et al., 2021). There are few guidelines regarding which scaling method should be used in machine learning, but it is suggested that most ML algorithms do not perform well when the input values have very different scales (Géron, 2019,Choi et al., 2021).

Choi et al. (2021) trained four machine learning algorithms using non-scaled data, min-max scaled data, and standardized data (Figure 3.5). The standardization method was chosen based on their findings.

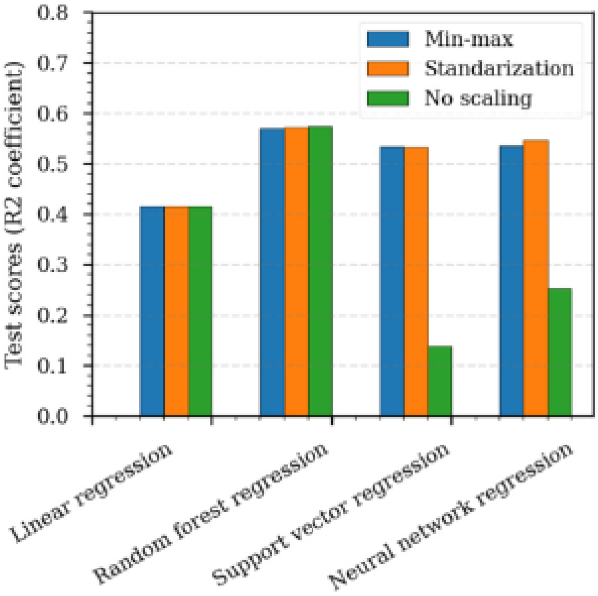

Figure 3.5: Test scores for different ML algorithms with different scaling methods in Choi et al. (2021)).

The standard score of a sample $x$ is calculated as:

$$z = (x - u)/s \tag{3.2}$$

Where $x$ is the numerical value, $u$ is the mean, and $s$ is the standard deviation of the training sample. The scaling of data will be discussed in Section XX.

Table 3.2: Binary representation of the two-pixel types and number of pixels in total, the training set, and test set.

| **Pixel Type** | **Random** | **Rockfall source area** |
|---|---|---|
| **Binary Code** | 0 | 1 |
| **No. of Pixels** | 28556 | 14047 |
| **No. of Pixels in Calibration set** | 19995 | 9827 |
| **No. of Pixels in Validation set** | 8561 | 4220 |

The data are split into two sets; A *calibration set* and a *validation set*. The calibration set will be used for training and tuning the data, the validation set will be held out until the final model is trained and will be validated using this Out-of-the bag data.

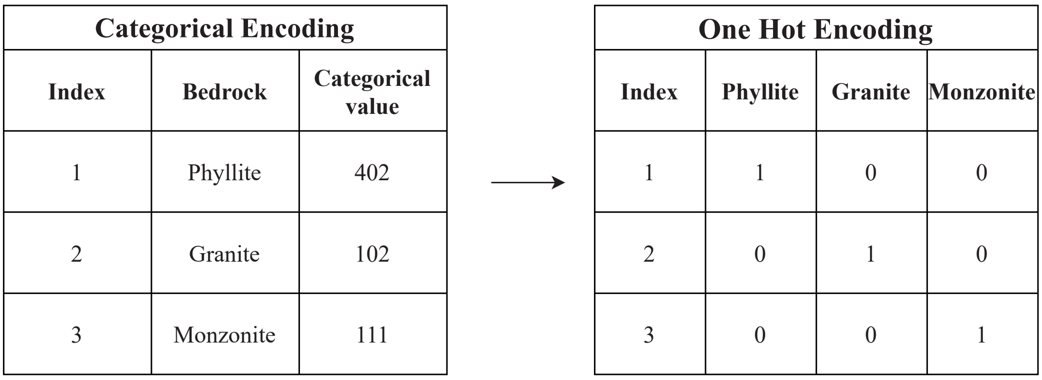

| Categorical Encoding | | |
|---|---|---|
| **Index** | **Bedrock** | **Categorical value** |
| 1 | Phyllite | 402 |
| 2 | Granite | 102 |
| 3 | Monzonite | 111 |

| One Hot Encoding | | | |
|---|---|---|---|
| **Index** | **Phyllite** | **Granite** | **Monzonite** |
| 1 | 1 | 0 | 0 |
| 2 | 0 | 1 | 0 |
| 3 | 0 | 0 | 1 |

Figure 3.6: Example illustration of One-hot encoding.

### 3.2.5 Decision Trees, Random Forest, and Gradient Boosted Regression Trees

The Random Forest and Gradient Boosted Regression Tree models were selected based on success full results in previous studies (Liu et al., 2020, Choi et al., 2021, Bagheri et al., 2018).

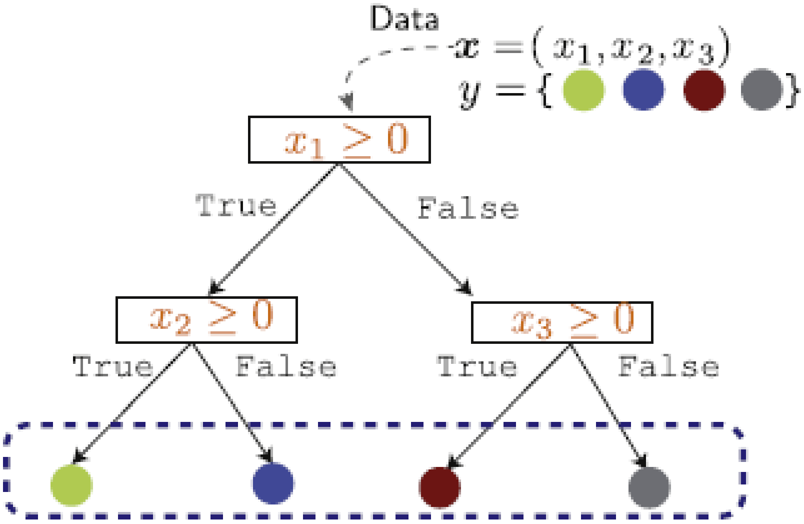

Figure 3.7: A Decision Tree with four possible outcomes from (Mehta et al., 2019).

*Decision trees* are used for both regression and classification problems and are the fundamental basis of the *Random Forest* method. A decision tree is a model with a tree-like structure where each square is called a node representing a test with a true/false answer (Figure 3.7). The node splits into two branches and will move the instance down to another node dependent on the answer to the test. The top node is called the root node, this node can have two child nodes. Nodes with no children are called leaf nodes and represent all possible outcomes and class labels. A decision tree is narrowing the decisions down from the root to a leaf node. It visualizes the options and goes through the possible outcomes dependent on the answer to each option. Decision trees are relatively intuitive, it is easy to see why the outcomes were made. The disadvantage of the Decision Tree method is that it is a high-variance method that is very prone to overfitting because the structure easily adapts itself to the training data (Géron, 2019, Mehta et al., 2019). The consequence of overfitting is that the model fails to correctly predict unseen data, which makes individual Decision trees weak classifiers (Mehta et al., 2019).

The aggregated predictions from a group of predictors will often yield better predictions than the best individual predictor. This technique is called Ensemble Learning. *Random Forest* is an "Ensemble Method", which trains a group of Decision Tree classifiers on random subsets of the training set to obtain predictions from a set of $n$ decision trees. Each decision tree is structured on a sample of the data with a random selection of features at each node (Fanos and Pradhan, 2019), this randomness will reduce the variance by reducing the correlation between the decision trees (Mehta et al., 2019). The class label that gets the most "votes" is predicted. (Géron, 2019, Mehta et al., 2019). This method is called Bagging, short for Bootstrap Aggregation. Random Forest is commonly used instead of a single decision tree because it is less likely to overfitting, and has lower variance without increasing the bias (Fanos and Pradhan, 2019). Random forest has been used for landslide classification in for example Liu et al. (2020), Fanos and Pradhan (2019), Dou et al. (2019) and Park and Kim (2019).

*The Gradient Boosted Regression tree (GBRT)* algorithm is another ensemble model which defines multiple decision trees to make predictions from random subsets but combines boosting and regression techniques instead of bagging to improve the accuracy and decrease the variance (Liu et al., 2020). The elements in the training data are weighted, some of them will appear more often in the subsets of features than others. Gradient Boosted Tree builds one tree at a time and combines results along the way of building decision trees. The subsequent trees are used to better define the not-correlated observations of the previous trees. The goal of the boosting method is thus to improve the prediction based on the previous trees (Liu et al., 2020).GBRT has been used for landslide susceptibility mapping in for example Liu et al. (2020),Park and Kim (2019) and Pourghasemi and Rahmati (2018)).

### Feature Importance

Random Forest has a built-in Feature Importance algorithm, which describes which features are relevant to train the model and affect the performance. The Feature Importance will compute the relative importance of each feature, with a cumulative value of 1. This can help to eliminate irrelevant features from the dataset to improve the efficiency of the model. Feature Importance was used to select 5 different feature combinations used for all the ML algorithms (Section 3.2.8).

### 3.2.6 Multilayer Perceptron

*The Multilayer Perceptron (MLP)* is an artificial neural network model. Artificial neural networks are inspired by the architecture of the brain with a network of biological neurons (Géron, 2019), they are good for large and high complex Machine-Learning tasks. MLP has been used for landslide susceptibility mapping in later years (Liu et al., 2020, Zare et al., 2013, Alkhasawneh et al., 2014), and is also an ensemble model. It is built up of multiple Perceptrons instead of decision trees like RF and GBRT.

A Perceptron consists of input neurons, bias neurons, and output neurons with weight connections between them. The Perceptron calculates a weighted sum of the input data and computes the output by sending the weighted sum through an activation function. The connection weights are adjusted for every wrongly predicted output, the weights from the inputs which contributed to correct predictions are reinforced to reduce the error (Géron, 2019). Some of the limitations of Perceptrons can be reduced or eliminated by stacking multiple Perceptrons into an MLP network (Géron, 2019). The simplest case of a Multilayer Perceptron architecture consists of three layers; the input layer, one hidden layer, and the output layer (Figure 3.8). The MLP is a fully connected network where each node is connected to all the nodes in the adjacent layers (Mehta et al., 2019).

Two methods make up the learning process of an MLP network: Feed-forward and backpropagation. The feed-forward process can be described as an extension of the processes inside one Perceptron and is repeated for each layer of the network (Hastie et al., 2009). Backpropagation optimizes the weights and biases in the model, using the chain rule to compute how much each output connection contributed to the error after making a prediction (Géron, 2019). This method is called backpropagation because the method uses the *chain rule* working backward until it reaches the input layer. The Gradient Descent method is then used to change the connection weights, using the error gradients computed by using the chain rule to reduce the error and (Géron, 2019).

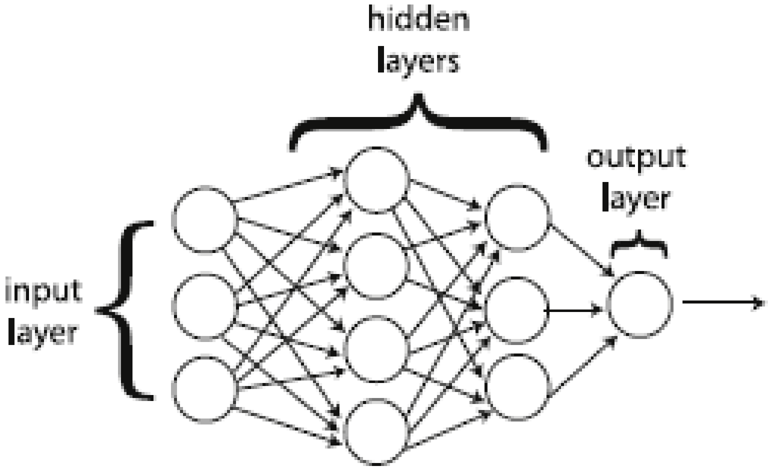

Figure 3.8: The architecture of a Multilayer Perceptron with two hidden layers (Mehta et al., 2019).

### 3.2.7 Logistic Regression

Logistic regression is a machine learning algorithm that was "borrowed" from classical statistics. It is a binary classifier that can be used to estimate the likelihood that an instance belongs to, say, class 0 or class 1, but it can also handle multiple classes (Géron, 2019). The response variable is”no rockfall” or ”rockfall” and is denoted as 0 or 1.

Regression methods are used for describing the relationship between a response variable, $Y$, and one or multiple exploratory variables. The *logit transformation*, $g(x)$, of the response variable is modeled as a linear combination of the predictor variables (Hosmer et al., 2013). $g(x)$ is the inverse of the S-shaped *sigmoid function* (Géron, 2019).

$$g(x) = ln\left[\frac{\pi(x)}{1-\pi(x)}\right] = \beta_0 + \beta_1 x \tag{3.3}$$

Where $\pi(x)$ is the expected value of $Y$, given a specific value of $x$. $\beta_0$ is the coefficient for the intercept, $x$ is the independent predictor variable and $\beta_1$ is the estimated coefficient for $x_1$. $\pi(x)$ is in other words the probability of an event occurring and 1 - $\pi(x)$ the probability of the event not occurring (Hosmer et al., 2013). $g(x)$, referred to as the *logit* or the *log-odds*, is linear in its parameters and may be continuous and range from -$\infty$ to $\infty$ depending on the range of $x$ (Hosmer et al., 2013).

The multiple logistic regression includes more than one predictor variable. Let the $p$ independent variables be denoted by $x' = (x1..Xp)$ and the conditional probability that the outcome is 1 by $Pr(Y = 1|x) = pi(x)$. The following equation (citehosmer applied 2013) gives the logit of the multiple logistic regression model:

$$g(x) = ln\left[\frac{\pi(x)}{1-\pi(x)}\right] = \beta_0 + \beta_1 x_1 + \beta_2 x_2 + .. + \beta_p x_p \tag{3.4}$$

Where the predicted probability, $\pi(x)$ is calculated as:

$$\pi(x) = \frac{e^{g(x)}}{1+e^{g(x)}} \tag{3.5}$$

The prediction is based on the If the estimated probability that the instance belongs to that class is greater than 50%, it is classified as belonging to that class (Géron, 2019):

$$\hat{y} = \begin{cases} 0, & \text{if } \hat{p} < 0.5 \\ 1, & \text{if} \hat{p} \geq 0.5 \end{cases}$$

Logistic regression was used in both the spatial analysis to predict rockfall source areas and the meteorological analysis to predict time.

### 3.2.8 Input Feature Selection

Eight feature combinations were generated from the set of collected input features (Figure 3.4). These features have been used for modeling rockfall source areas and shallow landslide areas in previous studies, but the combinations of features has varied (Alkhasawneh et al., 2014, Dou et al., 2019, Erener and Düzgün, 2010), Fanos and Pradhan, 2019, Liu et al., 2020, Park and Kim, 2019, Pourghasemi and Rahmati, 2018, Zare et al., 2013). In order to eliminate highly correlated features, a correlation analysis of all features was performed. In machine learning models, including highly correlated features as independent variables may obscure the relationship between other variables. In general, including highly correlated features does not improve a model. As a result, it is common to remove these to reduce the complexity of the learning algorithm. Choi et al. (2021) performed a correlation analysis of Leak-off pressure data and relevant variables to test the strength of the correlation between variables at a significance level of 0.05. The research was related to the selection of input features for machine-learning algorithms. Table 3.3 shows their classification of five different levels of correlation. The highest correlation in the set of input features used in this study is 0.5 between elevation and slope angle, falling into the "moderate" class. Both input features were kept.

Table 3.3: Correlation classification by Choi et al. (2021).

| **Absolute Correlation Coefficient $r$** | **Interpretation** |
|---|---|
| 0.9-1.0 | Very strong |
| 0.7-0.9 | Strong |
| 0.4-0.7 | Moderate |
| 0.2-0.4 | Weak |
| 0.0-0.2 | Negligible |

Table 3.4: The eight feature combinations used in the Random Forest, Gradient Boosted Regression Tree, Multilayer Perceptron and Logistic Regression models.

| | **Feature combinations** |
|---|---|
| **pc1** | Slope |
| **pc2** | Slope, Elevation |
| **pc3** | Slope, Aspect |
| **pc4** | Slope, Elevation, Plan curvature,<br>Profile curvature, TRI,<br>Distance to roads |
| **pc5** | Slope, Elevation, Plan curvature,<br>Profile curvature, TRI,<br>Flow direction, Flow accumulation,<br>Distance to roads |
| **pc6** | Slope, Elevation, Plan Curvature,<br>Profile Curvature, TRI |
| **pc7** | Elevation, Aspect, Plan curvature,<br>Profile curvature, TRI,<br>Flow direction, Flow accumulation,<br>Distance to roads |
| **pc8** | Slope, Elevation, Aspect,<br>Plan curvature, Profile curvature,<br>TRI, Flow direction,<br>flow accumulation, Distance to roads,<br>Bedrock |

### 3.2.9 Hyperparameters and implementation of model tuning with Cross-Validation

Hyperparameters are the internal parameters in ML algorithms that are not directly learned and have to be chosen to construct the model. The models can be tuned by optimizing these hyperparameters. The random search was used to tune 3 hyperparameters for the ensemble models RF, MLP, and GBRT (Figure 3.5). Hyperparameters for the logistic regression models was not tuned, default values from `Scikit-learn` was used (Pedregosa et al., 2011).

is a method that selects random hyperparameter combinations from a manually chosen search range and performs Cross-validation. The number of hyperparameter combinations was set as 10 and 5-fold cross-validation was used for each hyperparameter combination. A total of 150 fits were done for each of the eight input feature combinations for each of the algorithms. Default values from `Scikit-learn` were used for all other hyper-parameters.

The "n_estimators" hyperparameter is the number of trees used to build the RF, and the number of boosting stages in the GBRT algorithm,. The "max_depth " is the maximum depth of the trees in RF and GBRT. The "min_sample_leaf" hyperparameter is the minimum number of samples required to be at a leaf node. "Learning_rate" is a constant that multiplies the contribution of each tree by its value. Solver is the algorithm used in the MLP to optimize weights across nodes. The "alpha" hyperparameter is the MLP’s L2 penalty. The number of layerss in the MLP is determined by the hyperparameter "hidden_layer_sizes".

Table 3.5: Hyperparameter tuning of the ensemble models.

| **ML algorithm** | **Hyperparameter** | **Search range** | **Optimized values** | | | | | | | |
|---|---|---|---|---|---|---|---|---|---|---|
| | | | p1 | p2 | p3 | p4 | p5 | p6 | p7 | p8 |
| **RF** | n_estimators | 40-70 | 51 | 43 | 49 | 64 | 61 | 50 | 56 | 67 |
| | max_depth | 5-50 | 10 | 12 | 12 | 20 | 42 | 12 | 28 | 47 |
| | min_samples_leaf | 1-3 | 2 | 2 | 2 | 1 | 1 | 1 | 1 | 1 |
| **MLP** | hidden_layer_sizes | 30-70 | 37 | 62 | 50 | 53 | 54 | 61 | 49 | 45 |
| | alpha | 0 - 2, step = 0.5 | 0 | 0.5 | 1 | 1 | 0 | 0.5 | 0.5 | 0 |
| | solver | ”adam” ,”lbfgs” | ”adam” | ”lbfgs” | ”lbfgs’ | ”adam” | ”adam” | ”adam” | ”adam” | ”adam” |
| **GBRT** | n_estimators | 70 - 120 | 83 | 90 | 77 | 96 | 109 | 107 | 119 | 97 |
| | max_depth | 1 - 15 | 3 | 1 | 1 | 13 | 13 | 13 | 8 | 13 |
| | learning_rate | 0.10 - 0.30 step = 0.02 | 0.1 | 0.28 | 0.2 | 0.22 | 0.22 | 0.12 | 0.22 | 0.2 |

### 3.2.10 Susceptibility mapping

A new set of unseen data was extracted from a smaller area in the training area to make susceptibility maps with 10 x 10 m cell size resolution. In ArcGISPro (2.7.1), the "IDW" interpolation method was used to interpolate values between pixels.In addition, the models were tested on selected areas outside the training area in Vestland County to evaluate the performance on a regional scale. The susceptibility classes were chosen by using the "Natural-breaks (Jenks)" classification method (Bagheri et al., 2018), Losasso and Sdao, 2018, Liu et al., 2020 ) in ArcGISPro(2.7.1) for the susceptibility map including all input features (*pc*8). This classification of susceptibility categories was then used for all other susceptibility maps (Table 4.5). It is not possible to obtain evaluation metrics for the regional performance of the model due to the lack of registered source areas in the inventory database, which means that observed rockfall source area pixels do not exist for this region. However, the results from the regional implementation will be compared to other susceptibility studies in the county, the registered rockfalls, and the existing national potential rockfall source areas.

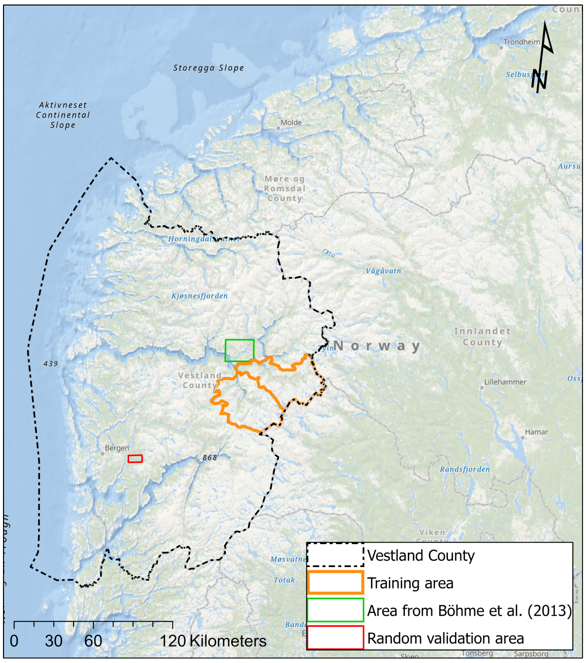

Figure 3.9: Map showing Vestland County, the training area, and a selected "evaluation" area.

## 3.3 Meteorological analysis - Data and Methods

The meteorological analysis consists of three equally important parts: data collection, selecting and calculating relevant variables (described in section 2.2.4), and then describing patterns and interesting relationships in the data using standard statistical methods. As a result, the analysis employs both quantitative and qualitative methods to describe the effects of temperature and precipitation on the release of rockfall occurrence in Vestland County.

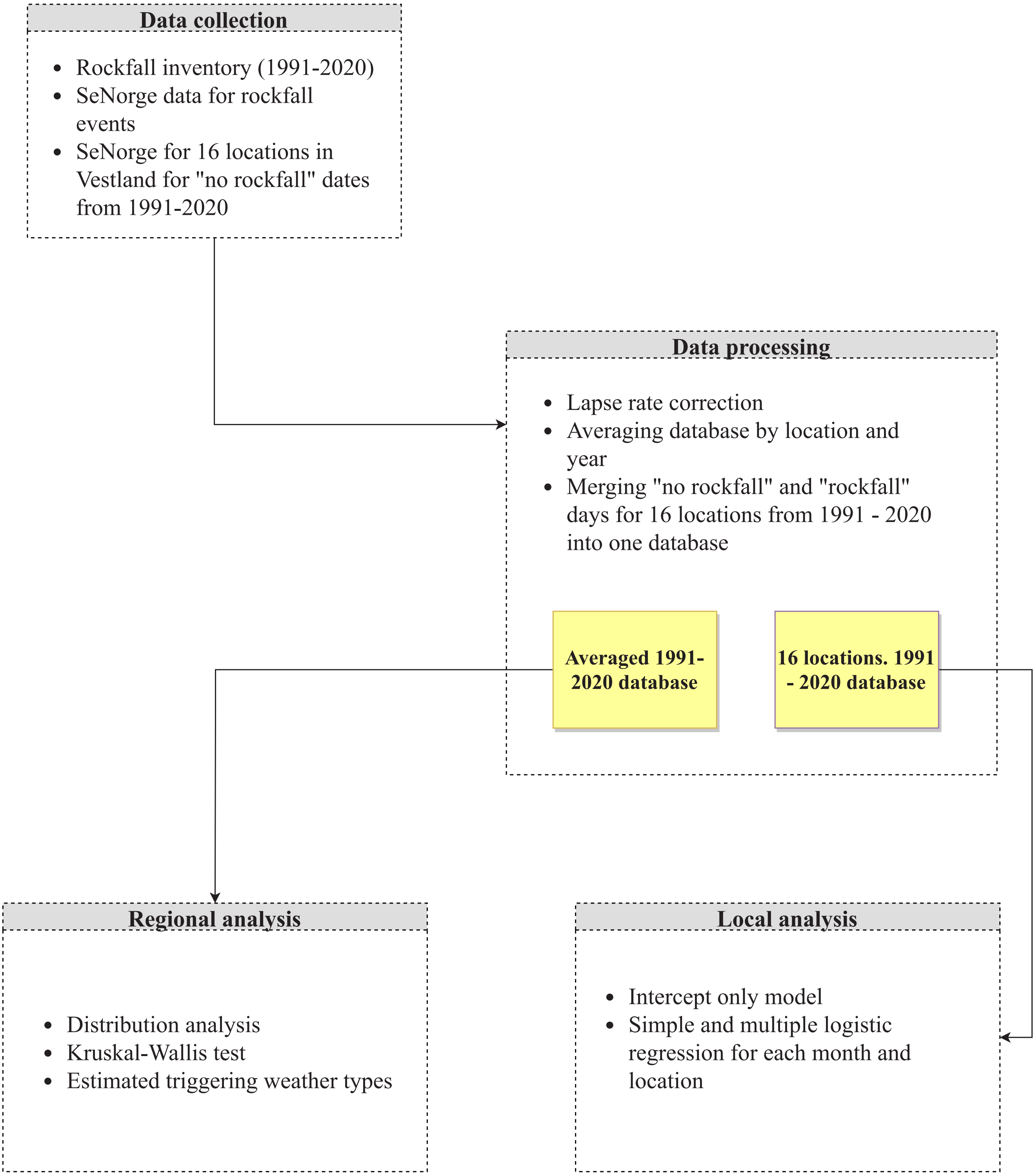

Figure 3.10: The workflow of the temporal analysis of rockfall release probability related to meteorological effects.

### 3.3.1 SeNorge data

Precipitation, temperature, snow depth, and SWE is from the SeNorge2 dataset produced and maintained by The Norwegian Meteorological Institute (MET). The dataset is available at https://thredds.met.no/thredds/catalog/metusers/senorge2/seNorge2/provisional_archive/PREC1d/gridded_dataset/catalog.html.

SeNorge2 provides 1 km x 1 km gridded daily mean temperature and total precipitation for the Norwegian mainland from 1957. Information from *in situ* observations is used to interpolate the data with the Optimal Interpolation method. The number of stations used for the interpolation varies in time due to data availability and station distribution (Lussana et al., 2018). The daily precipitation for a day $D$ is defined as the accumulated precipitation between 06:00 UTC of the day $D$ - 1 and 06:00 UTC of the day $D$. The distribution of stations is denser for lower elevations along the coast and denser in the south than in the north, causing variability in data accuracy.

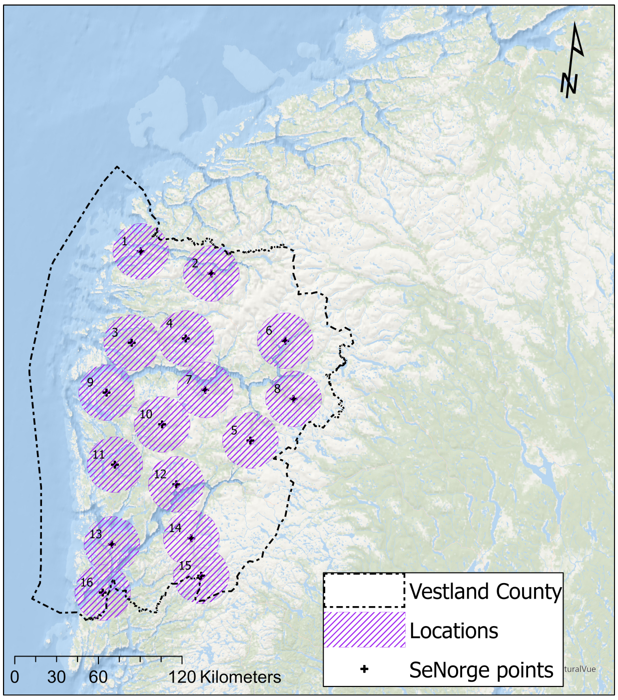

Figure 3.11: Map showing Vestland County, and the defined locations. SeNorge2 data were extracted from the SeNorge points.

### 3.3.2 Vestland rockfall climate database

The meteorological database for Vestland county was made by making extracting SeNorge2 daily temperature and precipitation data from all rockfall impact coordinates from the inventory database (Section 3.1.4). All source areas except the 95 source area polygons that were estimated for Lærdal and Aurland are unknown. The elevation difference between the rock impact and the source area affects both temperature and precipitation. If the rockfall impact is registered at 0 m.a.s.l and the rockfall source area is at 400 m.a.s.l, will a temperature corrected for lapse rate be 2.52 degrees colder than the uncorrected temperature from SeNorge2. A buffer of 500 meters were made around each rockfall impact, and the highest elevation from the 10 x 10 m DEM was extracted and used as elevation. The elevation difference between the SeNorge DEM and extracted elevations was calculated, and temperature and precipitation were adjusted with lapse rate. The lapse rate used for temperature is 0.63 $\circ$C/100 m and an increase in precipitation of 10%/100 m. These values are commonly used for Vestland County.

### 3.3.3 Reference climate database 1991 - 2020

The reference climate database for Vestland was created by extracting daily temperature and precipitation from SeNorge using 16 coordinate points in Vestland County from January 1, 1991 to January 1, 2020. This period was chosen due to the increased number of rockfall events after 1970, as well as the fact that it is the same period as the new official Climate Normal (Figure 3.12). The points were chosen based on their location and representative elevations of 500 m.a.s.l. on average. To achieve some data homogeneity, SeNorge2 data was used. Vestland County has several climate stations, but their temporal resolution varies.

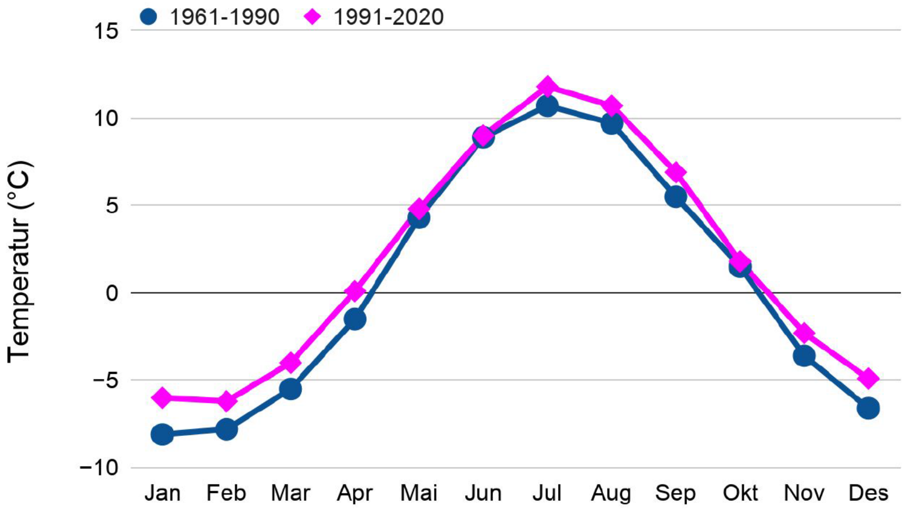

Figure 3.12: Figure from a presentation at The Norwegian Meteorological Institute by Tajet (2021), comparing the previous (1961 - 1990) and the new climate normal (1991 - 2020) in Norway. The temperature is on the y-axis and the months are on the x-axis.

### 3.3.4 Distributions of rockfall climate and reference climate

In statistics, there are two types of random variables: discrete and continuous. A discrete random variable is a set of countable values. Continuous random variables are values that can have an infinite number of values in between any two values. Discrete random variables are categorical, such as the average number of rockfall events per year, whereas continuous random variables, such as temperature and precipitation, are continuous.

$f(x)$ is a probability density function for a continuous random variable, $X$ ,if $f(x)$ satisfies two conditions: $f(x) \geq 0 \quad$ for all $x_i$ and $\int f(x)dx = 1$ for the whole range of $x$.

The cumulative distribution function (CDF) if a continuous random variable is a function ($F(x)$) that gives the probability that the random variable $X$ is less than or equal to $x$, for every value of $x$. $F(x)$ is the integral of its probability density function f(x). The formal definition is then:

$$F(x) = P(X \leq x), \quad for \text{ - } \infty < x < \infty \tag{3.6}$$

and

$$F(x) = \int f(x)dx \tag{3.7}$$

A histogram depicts the probability distribution of a variable, with the normalized probability density on the y-axis and the variable value on the x-axis. As one of the conditions for the PDF for a continuous random variable, the total area of the histogram is one.

The Vestland database was averaged for every 16 locations and each year (1991-2020) in order to represent a reference climate for Vestland County. The distributions' mean, $mu$, and variance, $sigma$, are two significant statistical variables that can provide us with a valuable understanding of the data.

### 3.3.5 Statistical inference and the Kruskal-Wallis H-test

Statistical inference is a procedure that generalizes the characteristics of a sample to the characteristics of a population (DeCoster, 2006). Estimating the mean of a sample and using that mean to draw conclusions about the mean of the entire population is an example of inference.

A common statistical inference method is *hypothesis testing*. The first step in a hypothesis test is to establish a null hypothesis, $H_0$, and an alternative hypothesis, $H_a$. The null hypothesis makes a specific claim about the tested variable, while the alternative hypothesis rejects the null hypothesis. A hypothesis test use data from the sample to either reject or fail to reject the null hypothesis by calculating test statistics that reflect the difference between the tested variable and the expected value of that variable if the null hypothesis were true (DeCoster, 2006). A p-value is calculated for the test statistics, which is the probability that the results of the test statistics are due to random chance if the null hypothesis were indeed true. The null hypothesis is rejected if the p-value is lower than a chosen significance level, $a$. The test fails to reject $H_0$ if the p-value is higher than $a$. A significance level of $a = 0.05$ means a 5% chance of rejecting the null hypothesis when it is actually true.

The Kruskal-Wallis test (Kruskal and Wallis, 1952) can be used to determine whether a variable in two or more data sets comes from the same population. Almost all samples differ to some extent; the question is whether the difference represents a difference between populations or whether it represents the expected variation among random samples from the same population

(Kruskal and Wallis, 1952). The method is a non-parametric version of the commonly used ANOVA test (DeCoster, 2006).

The Kruskal-Wallis test determines whether the difference in the medians of two or more groups is statistically significant. Because the distribution types are unknown, the Kruskal-Wallis test is an appropriate hypothesis test for comparing these two groups of data. The null hypothesis states that there is no significant difference between different variables in "Rockfall climate" and "Reference climate" in Vestland county, implying that the data are from the same population. The level of significance, $a$, is set to 0.05.

The following Kruskal-Wallis tests were performed with a significance level of 0.05:

- $H_0$: There is no significant difference in median daily precipitation in "Rockfall climate" and "Reference climate". $H_a = H_0$ is rejected.
- $H_0$: There is no significant difference in median daily temperature in "Rockfall climate" and "Reference. $H_a = H_0$ is rejected.

The test is carried out by combining the data from the two groups and ranking the subjects based on the values of the tested response measure. The lowest rank has a value of one, and the highest rank has a value of $n1 + n2$ (Kruskal and Wallis, 1952). The Kruskal-Wallis test statistics are calculated as follows:

$$H = \frac{12}{N(N+1)} \sum_{i=1}^{k} \left( \frac{R_i^2}{n_i} \right) - 3(N+1) \tag{3.8}$$

Where N is the total number of observations in the groups, $k$ is the total number of groups, $R_i$ is the sum of the ranks for group $i$ and $n_i$ is the sample size for group $i$ (Kruskal and Wallis, 1952).

### 3.3.6 The Logistic Regression prediction model

Logistic Regression was described in Section 3.2.7. This model was used to fit models for rockfall occurrence probability in Vestland. Models were fit at both the regional and local levels (Figure 3.11). The main goal of the prediction model is to describe whether temperature or precipitation or a combination of these could be used as predictors rockfall occurrence. The following models were constructed for each of the 16 locations in Vestland county and for Vestland County as one:

1. A null model with no predictors.
2. A simple logistic regression with daily mean temperature as a predictor.
3. A simple logistic regression with daily precipitation as a predictor.
4. A multiple logistic regression with daily mean temperature, daily precipitation, and an interaction term of daily temperature an daily precipitation.

The Akaike information criterion was used to estimate to prediction error, the method was used for evaluation of the models (Hastie et al., 2009). The criterion is defined as:

$$AIC = 2k - 2\log(\hat{L}) \tag{3.9}$$

Where $k$ is the number of predictors and $\hat{L}$ is the maximum value of the likelihood function for the model. The method compared the fitted model to the null model in order to evaluate if adding the predictor makes a significant better fit. AIC is used for model selection; the model with the lowest AIC among the compared models is considered the "best fit" model (Hastie et al., 2009).

# Chapter 4

# Results

## 4.1 Machine learning

### 4.1.1 Range of input features

Looking at the range of input features that are a common part of the pre-work or exploratory analysis in machine learning methods, some of them will be presented in this subsection. The peak elevation is around 1500 m.a.s.l (Figure A4a). The peak slope angle for rockfall pixels is around 65-70 degrees and 15 degrees for random pixels (Figure A4b). The shape of the elevation histogram for random pixels can describe the general distribution of elevation in the area. The elevation values for rockfall pixels are more evenly distributed. The histograms show that the slope is skewed to the left for rockfall pixels and to the right for random pixels, which is desirable for the training of ML models for rockfall source area prediction. The slope angles for the mapped rockfall source polygons in the training area are expected to be large, while the slope angles for the randomly selected pixels outside these polygons should be smaller because they represent areas not prone to rockfall occurrence.

Monzonite, Gabbro, Charonockite, Anorthosite, Phyllite, Granitic gneiss, and Orthopyroxene gneiss are the most common bedrock types in the study area (Figure A1). Random pixels have the highest frequency of Charonockite, Phyllite, Anorthosite, Granitic Gneiss, and Orthopyroxene gneiss. Rockfall pixels are most represented by rock type Monzonite, which is over-represented for rockfall pixels compared to the other common bedrocks types in the area. The mean distance to roads for rockfall pixels is 670 m and 2068 for random pixels, and the most common aspect direction for both random and rockfall pixels in the study area is West and South West (Figure A3a).

The frequency distribution plots of slope, elevation, bedrock, and distance to roads in the calibration and validation sets show that the whole range of values of each feature is represented in both the calibration and the validation of the models (Figure A2).

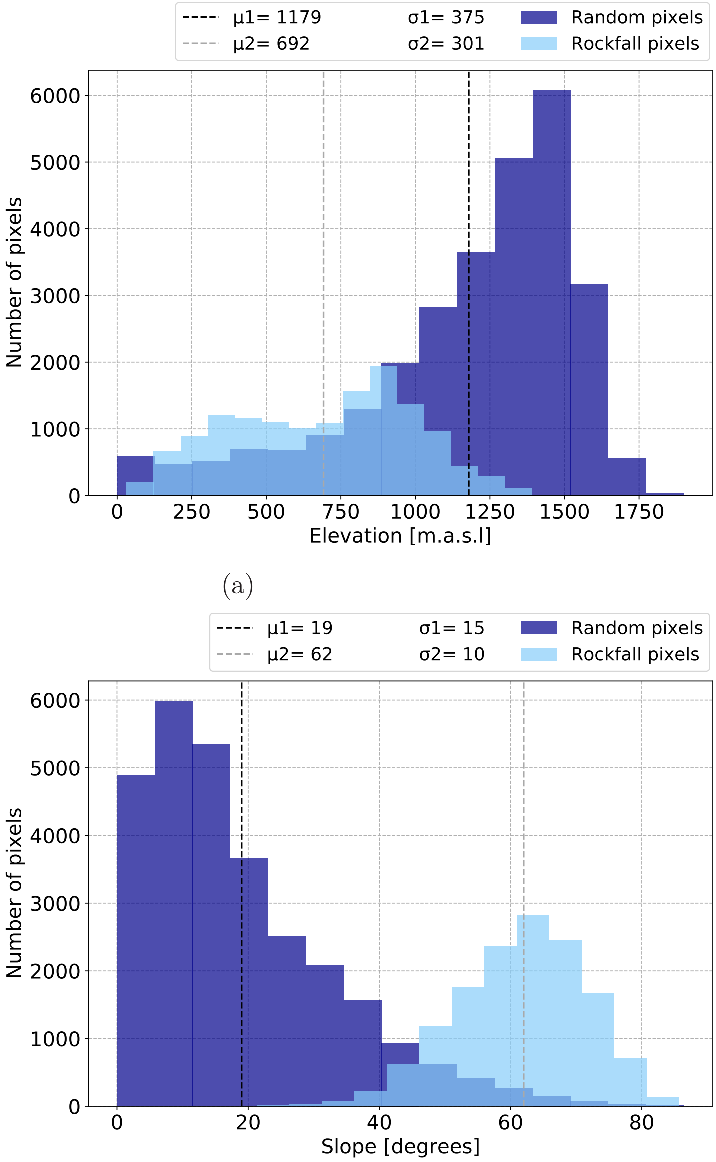

(a)

(b)

Figure 4.1: Histograms showing (a) elevation and (b) slope angles for random and rockfall pixels. For rockfall pixels, elevation ranges from 0 to 1400 m.a.s.l., and for random pixels, elevation ranges from 0 to 1800 m.a.s.l. Slope angle ranges from 30 to 90 for rockfall pixels and 0 to 70 for random pixels. The legend displays the mean ($\mu_1$ for random pixels and $\mu_2$ for rockfall pixels) and standard deviation ($\sigma_1$ for random and $\sigma_2$ for rockfall). Bins = 15.

### 4.1.2 Random Forest feature importance's

The relative importance of features (Table 4.1) helps to understand which features have the most predictive power for rockfall source areas. Bedrock types had a total of zero relative importance in feature combination *pc*8 and are therefore not included.

Slope angle is the most important feature in all subsequent combinations in which it was included, Liu et al. (2020) obtained the same result for shallow landslides in Kvam. The highest relative importance for slope is 1 in *pc*1, because it is the only feature in that combination. The next highest relative future importance of slope angle is in *pc*3 in combination with aspect. Elevation was not included in *pc*3, showing that slope angle is more important when elevation is absent due to the observed correlation between the two features (Section 3.2.8). The lowest relative importance for slope is observed in feature combination *pc*8 and *pc*4 (Table 4.1). Without the relatively most important input feature, slope angle, feature combination *pc*7 demonstrates that profile curvature is the most important feature in that combination. This outcome is unexpected. Based on the results for all other feature combinations where the elevation was ranked as more important than profile curvature, it was therefore expected that elevation would be the most important feature in this combination.

For the feature combinations that include them, all categorical aspect features have low relative importance. West is the aspect category with the highest relative importance. The total relative feature importance for the aspect categories in *pc*3 is 0.025. TRI, flow direction, and aspect have in general the lowest relative feature importance.

Table 4.2: The relative importance of each feature in the eight Random Forest feature combinations. The importances are ranked from 0 to 1, with 1 representing the total importance of all features in each combination. Grey cells are features that are not part of that feature combination. This table does not include bedrock.

| | **pc1** | **pc2** | **pc3** | **pc4** | **pc5** | **pc6** | **pc7** | **pc8** |
|---|---|---|---|---|---|---|---|---|
| **Slope** | 1 | 0.758 | 0.972 | 0.492 | 0.494 | 0.598 | | 0.436 |
| **Elevation** | | 0.241 | | 0.174 | 0.119 | 0.222 | 0.227 | 0.138 |
| **Profile Curvature** | | | | 0.112 | 0.101 | 0.093 | 0.236 | 0.081 |
| **Plan curvature** | | | | 0.081 | 0.106 | 0.070 | 0.202 | 0.074 |
| **TRI** | | | | 0.022 | 0.022 | 0.017 | 0.050 | 0.017 |
| **Distance to roads** | | | | 0.119 | 0.129 | | 0.199 | 0.103 |
| **Flow accumulation** | | | | | 0.145 | | 0.036 | 0.013 |
| **Flow direction** | | | | | 0.014 | | 0.017 | 0.013 |
| **West** | | | 0.014 | | | | 0.010 | 0.006 |
| **South West** | | | 0.005 | | | | 0.004 | 0.004 |
| **East** | | | 0.004 | | | | 0.004 | 0.003 |
| **North West** | | | 0.002 | | | | 0.004 | 0.003 |
| **South East** | | | 0.000 | | | | 0.002 | 0.002 |
| **North East** | | | 0.000 | | | | 0.003 | 0.002 |
| **South** | | | 0.000 | | | | 0.002 | 0.002 |
| **North** | | | 0.000 | | | | 0.002 | 0.002 |

### 4.1.3 Performance of models

The values from the confusion matrix of selected models show the percentage of correctly and wrongly classified predictions and if they belong to the positive or negative class (Table 4.3). The evaluation metrics accuracy, precision, recall, F1-score, and AUC-ROC from the validation of models are used to evaluate model performances (Table 4.4). The distinctions between metrics scores are minor, particularly between RF, GBRT, and MLP. The feature combination *pc*8, which includes all input features, yields the highest metric scores for all the algorithms. The LR *pc*7 model does not perform well in the feature combination without slope angle, as evidenced by the ROC curve (Figure A6 and Figure A7). The performance of the RF, GBRT and MLP models with feature combination *pc*7 is unsatisfactory compared to the other feature combinations, but the difference is not as significant as that of the LR model. This result demonstrates that slope angle as the sole predictor for rockfall source areas outperforms using all other input features except slope with a Logistic Regression model.

The Logistic Regression *pc*1, *pc*2, and *pc*3 models perform as well as or better than the more complex models RF, GBRT, and MLP (Table 4.4). Logistic Regression metrics are very similar to MLP metrics for feature combination *pc*5. The difference in performance between Logistic Regression and RF, GBRT, and MLP is more noticeable for feature combinations *pc*6, *pc*7, and *pc*8, which have a greater number of input features than the previous combinations.

Recall, or the sensitivity, is, in general, higher than precision for all four algorithms (Table 4.4). The recall is often higher than precision in models trained on data sets where the positive class is the minority class (Géron, 2019) because it shows the ratio of correctly classified predictions in the positive (TP) class and actual values belonging in the positive class (TP and FN) (Section 2.5.5).

Table 4.3: Values from the confusion matrix of three selected models for each ML algorithm. Feature combinations are listed in Table 3.4.

| | **True Negatives (TN)** | | | **False Positives (FP)** | | |
|---|---|---|---|---|---|---|
| | *pc*1 | *pc*7 | *pc*8 | *pc*1 | *pc*7 | *pc*8 |
| **RF** | 62.94% | 63.34% | 65.25% | 4.05% | 1.73% | 3.64% |
| **MLP** | 62.92% | 63.21% | 65.61% | 4.06% | 3.77% | 1.38% |
| **GBRT** | 62.87% | 63.77% | 65.64% | 4.12% | 3.21% | 1.34% |
| **LR** | 63.66% | 58.04% | 64.28% | 3.31% | 8.94% | 2.70% |
| | **False Negatives (FN)** | | | **True Positives (TP)** | | |
| **RF** | 1.92% | 2.47% | 0.58% | 31.10% | 30.55% | 32.44% |
| **MLP** | 1.81% | 4.26% | 0.62% | 31.21% | 28.75% | 32.40% |
| **GBRT** | 1.82% | 2.02% | 0.47% | 31.19% | 31.00% | 32.55% |
| **LR** | 2.48% | 13.95% | 1.61% | 30.54% | 19.07% | 31.41% |

Table 4.4: Validation metrics for each feature combination and ML-algorithm (Table 3.4 and 4.1).

| | **Feature combination** | **Accuracy** | **Precision** | **Recall** | **F1** | **AUC-ROC** |
|---|---|---|---|---|---|---|
| **RF** | pc1 | 0.940 | 0.885 | 0.942 | 0.934 | 0.941 |
| | pc2 | 0.948 | 0.895 | 0.951 | 0.941 | 0.948 |
| | pc3 | 0.941 | 0.887 | 0.941 | 0.934 | 0.941 |
| | pc4 | 0.964 | 0.922 | 0.974 | 0.960 | 0.967 |
| | pc5 | 0.964 | 0.922 | 0.974 | 0.960 | 0.967 |
| | pc6 | 0.952 | 0.900 | 0.964 | 0.948 | 0.956 |
| | pc7 | 0.939 | 0.894 | 0.925 | 0.932 | 0.935 |
| | pc8 | 0.977 | 0.949 | 0.982 | 0.974 | 0.978 |
| **MLP** | pc1 | 0.941 | 0.885 | 0.945 | 0.935 | 0.942 |
| | pc2 | 0.947 | 0.897 | 0.949 | 0.941 | 0.949 |
| | pc3 | 0.944 | 0.893 | 0.942 | 0.937 | 0.944 |
| | pc4 | 0.951 | 0.907 | 0.948 | 0.945 | 0.947 |
| | pc5 | 0.964 | 0.926 | 0.967 | 0.959 | 0.963 |
| | pc6 | 0.949 | 0.903 | 0.945 | 0.943 | 0.947 |
| | pc7 | 0.920 | 0.884 | 0.871 | 0.909 | 0.902 |
| | pc8 | 0.980 | 0.959 | 0.981 | 0.978 | 0.980 |
| **GBRT** | pc1 | 0.941 | 0.883 | 0.945 | 0.934 | 0.942 |
| | pc2 | 0.948 | 0.897 | 0.952 | 0.942 | 0.949 |
| | pc3 | 0.944 | 0.885 | 0.952 | 0.937 | 0.944 |
| | pc4 | 0.966 | 0.928 | 0.973 | 0.962 | 0.947 |
| | pc5 | 0.970 | 0.935 | 0.978 | 0.967 | 0.963 |
| | pc6 | 0.950 | 0.810 | 0.954 | 0.944 | 0.947 |
| | pc7 | 0.948 | 0.906 | 0.939 | 0.941 | 0.902 |
| | pc8 | 0.982 | 0.961 | 0.986 | 0.980 | 0.980 |
| **LR** | pc1 | 0.942 | 0.902 | 0.925 | 0.935 | 0.938 |
| | pc2 | 0.943 | 0.903 | 0.927 | 0.936 | 0.939 |
| | pc3 | 0.944 | 0.907 | 0.926 | 0.937 | 0.939 |
| | pc4 | 0.947 | 0.908 | 0.935 | 0.941 | 0.944 |
| | pc5 | 0.943 | 0.908 | 0.935 | 0.941 | 0.944 |
| | pc6 | 0.943 | 0.903 | 0.926 | 0.936 | 0.939 |
| | pc7 | 0.771 | 0.681 | 0.577 | 0.730 | 0.721 |
| | pc8 | 0.957 | 0.921 | 0.951 | 0.952 | 0.955 |

Validation results for RF, GBRT, and MLP with feature combinations *pc*1 and *pc*8 plotted in the training area further demonstrate the small differences in model performance (Figure 4.2 and Figure 4.3). The maps show that the majority of pixels predicted as rockfall source areas (TP and FP) in the training area are located along the two valleys.

The models with feature combination *pc*1 have a higher number of false-positive predictions than the models with feature combination *pc*8. A closer examination of the validation results from the GBRT *pc*1 and *pc*8 models in a selection of the training area (4.4) reveals that false-positive predictions are located on steep slopes that were not mapped as rockfall source areas for the training set, but could potentially be actual rockfall source areas. The rockfall source areas that have been mapped for training are well predicted.

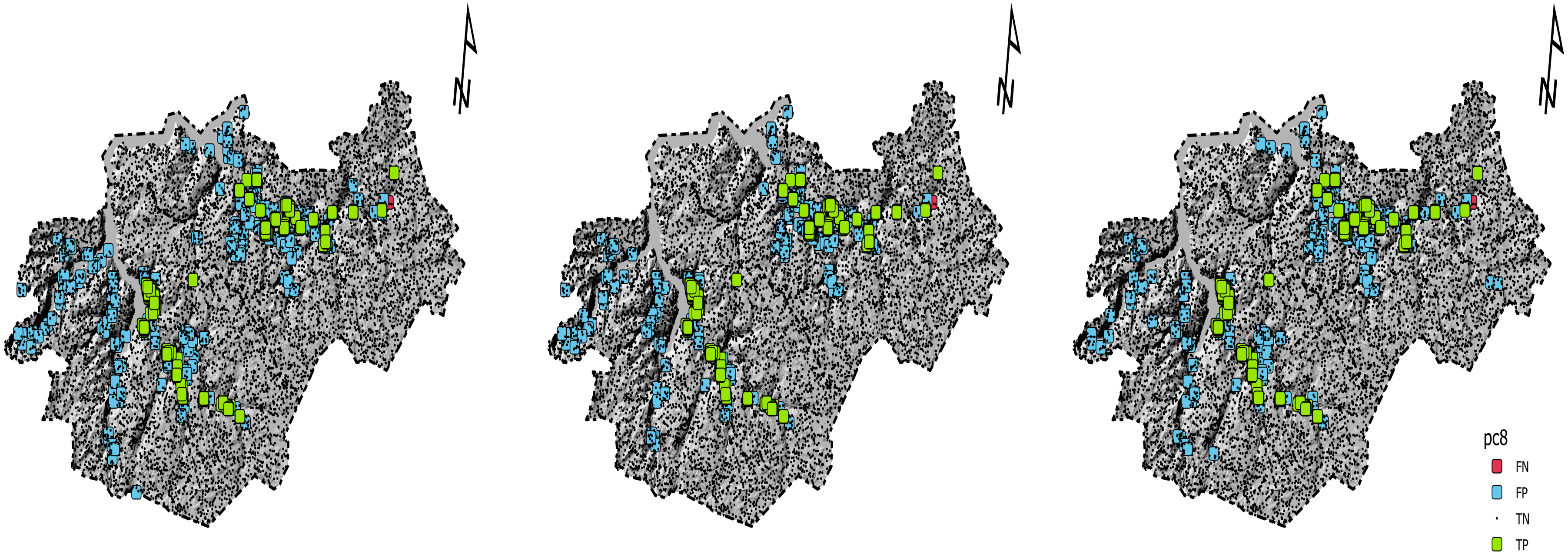

(a) RF (b) MLP (c) GBRT

Figure 4.2: Validation results from feature combination *pc*8 for the three models. Locations is shown in Figure 3.2.

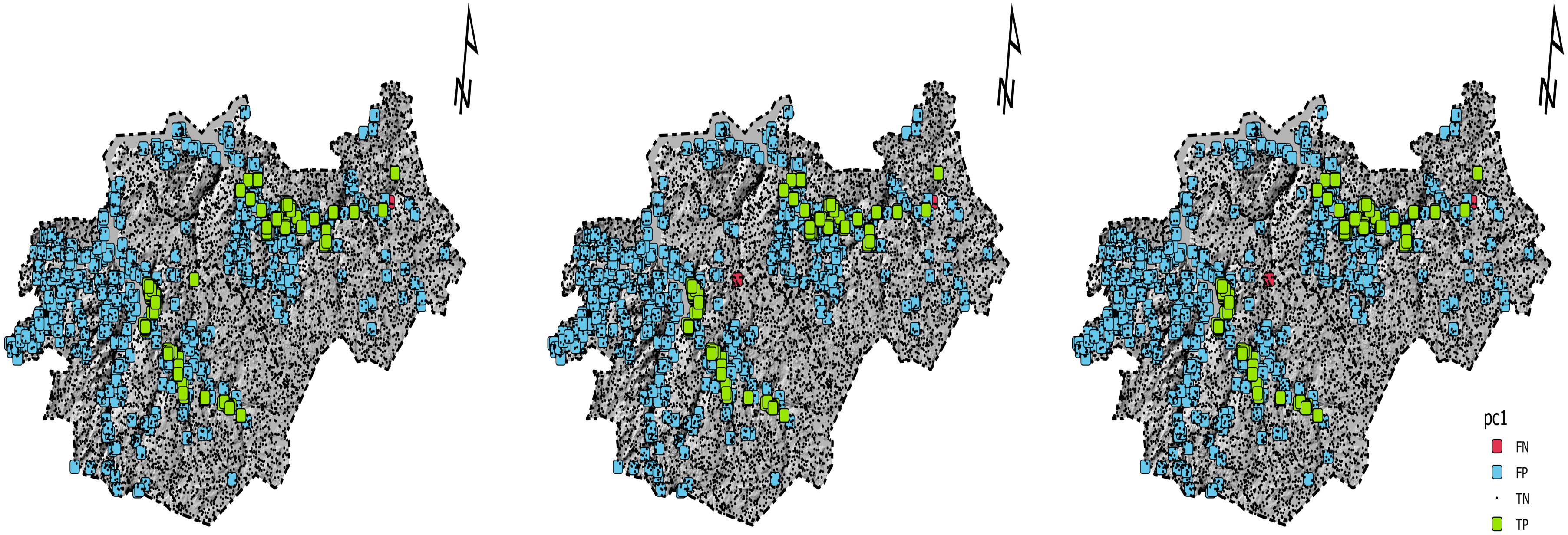

(a) RF (b) MLP (c) GBRT

Figure 4.3: Validation results from feature combination $pc1$ for the three models. Locations is shown in Figure 3.2.

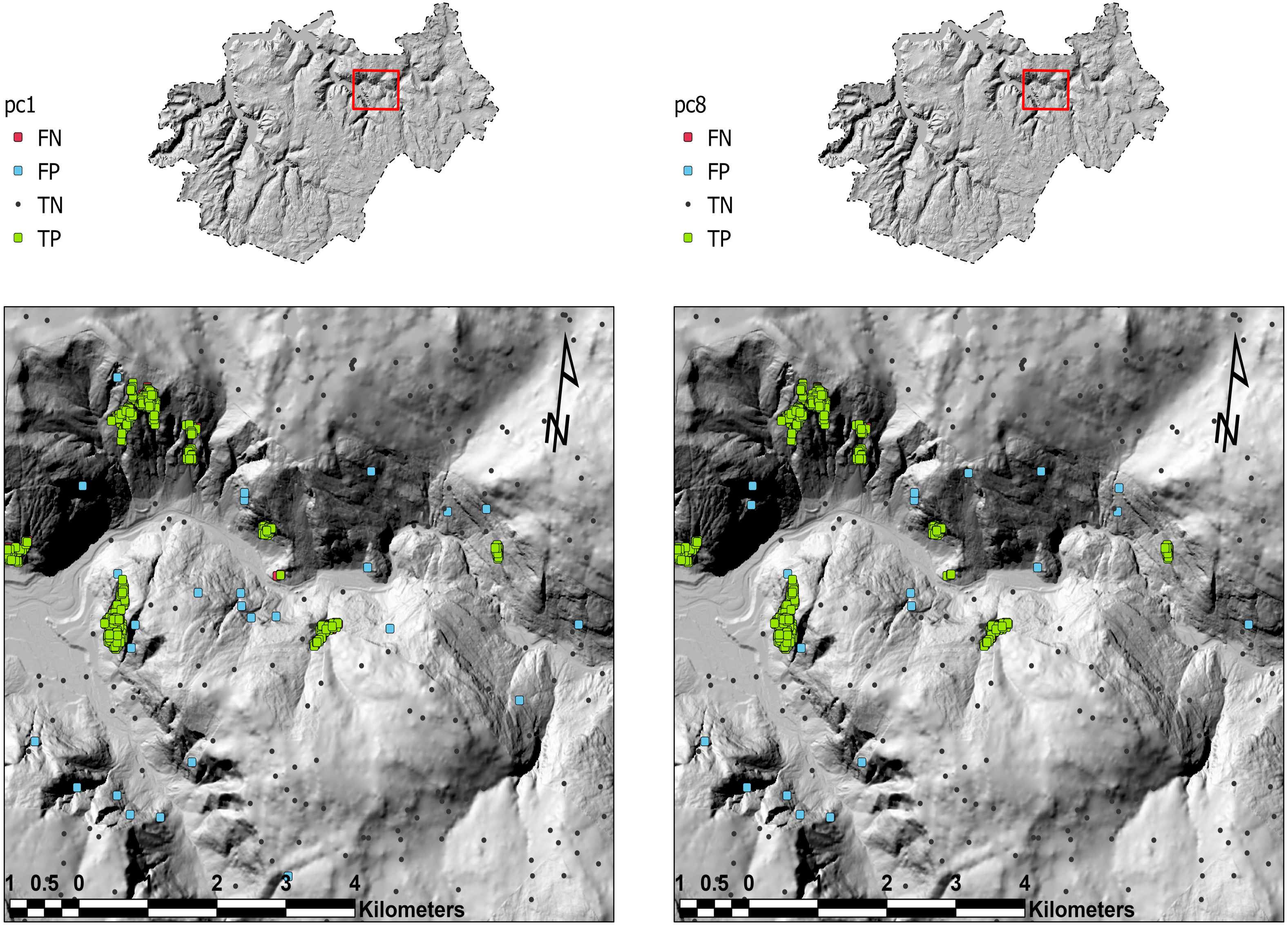

(a) MLP *pc*1. (b) GBRT *pc*8.

Figure 4.4: Map displaying the MLP *pc*1 and GBRT *pc*8 model prediction results for a selected area in the training area (Figure 3.2.

### 4.1.4 Potential rockfall source areas

The machine learning models compute the probabilities that a pixel will be classified as 1 or 0, as well as the actual classification result. This probability was used to identify potential rockfall source areas ranging from low to high susceptibility. Using the Natural Breaks (Jenks) method in ArcGISPro, the values were classified as very low, low, moderate, and high (Table 4.5). In ArcGISPro (2.7.1), an inverse distance weighting (IDW) interpolation was performed to generate continuous susceptibility maps from the predicted probabilities (Figure 4.5, Figure 4.6b, Figure 4.7)b, and Figure 4.8b). The rockfall source areas predicted by ML algorithms follow the same pattern as the L. Dorren and Berger (2010) map, which is to be expected given that slope angle is the most predictive feature. This is especially true for the MLP *pc*1 map, with only slope angle as a predictor, and the LR *pc*8 map. When the L. Dorren and Berger (2010) new 2010 map is compared to the predicted rockfall source areas in this study, it is clear that the maps predicted with ML algorithms are more detailed than the national potential rockfall source areas. The GBRT *pc*7 map stands out due to its more fragmented division of areas within the different susceptibility classes (Figure 4.6).

Table 4.5: Susceptibility classes defined in ArcGISPro 2.7.1 from probability maps from the GBRT *pc*8 model using the Natural Breaks (Jenks) method. In this study, these classes are used for all susceptibility maps.

| **Susceptibility class** | **Upper probability value** |
|---|---|
| Low | 0.15 |
| Moderate | 0.478 |
| High | 0.82 |
| Very high | 0.99 |

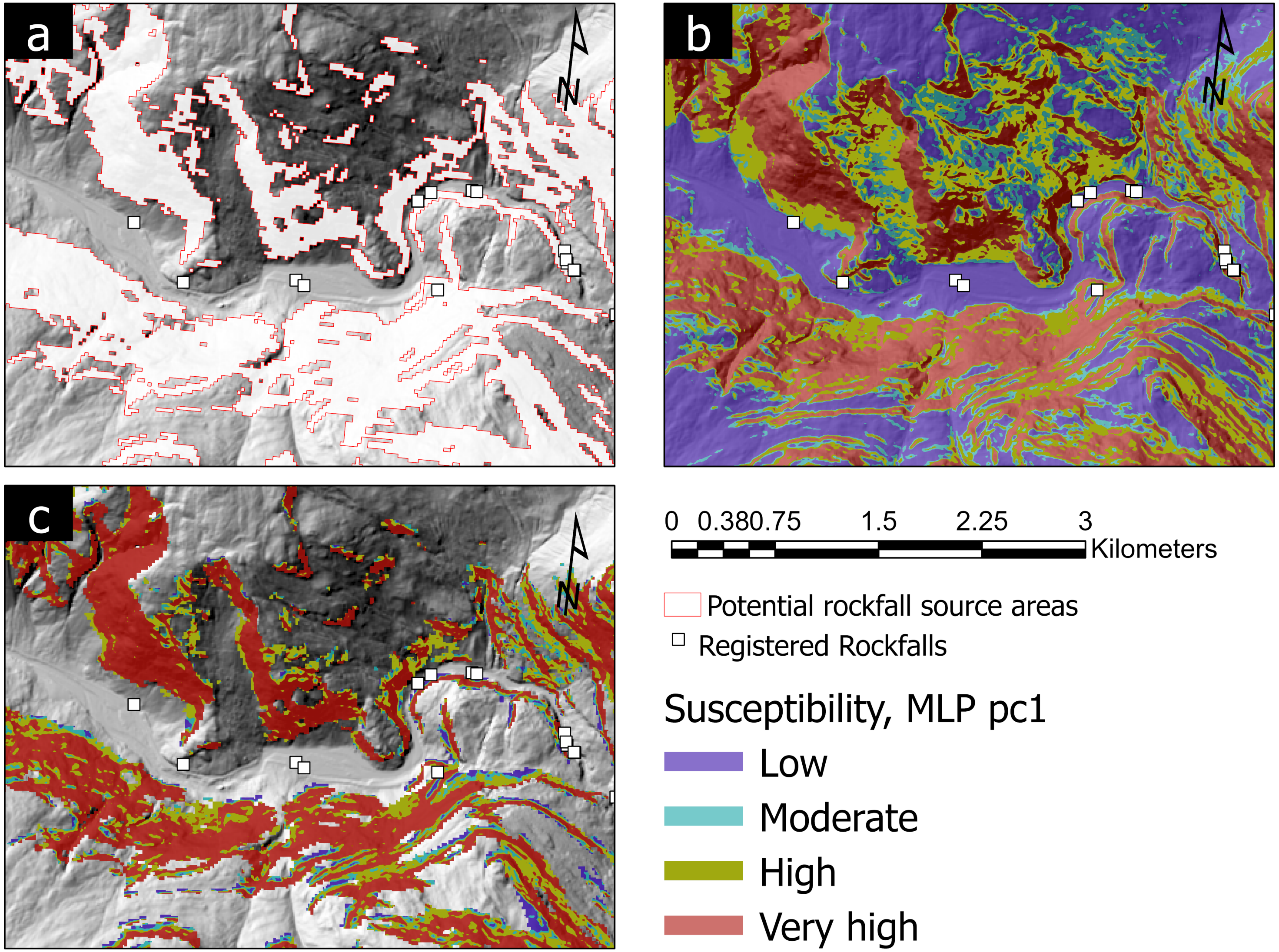

Figure 4.5: Map showing low, moderate, high, and very high rockfall source area susceptibility modeled with the MLP *pc*1 model in a selected part of the training area (Figure 4.4). Classes are defined in Table 4.5. Resolution 10x10m. a) Potential rockfall source areas from the national susceptibility map (Derron, 2010). b) Modelled rockfall susceptibility for the entire selected area. c) Modelled rockfall susceptibility clipped to the extent of the national potential rockfall source areas from Derron (2010).

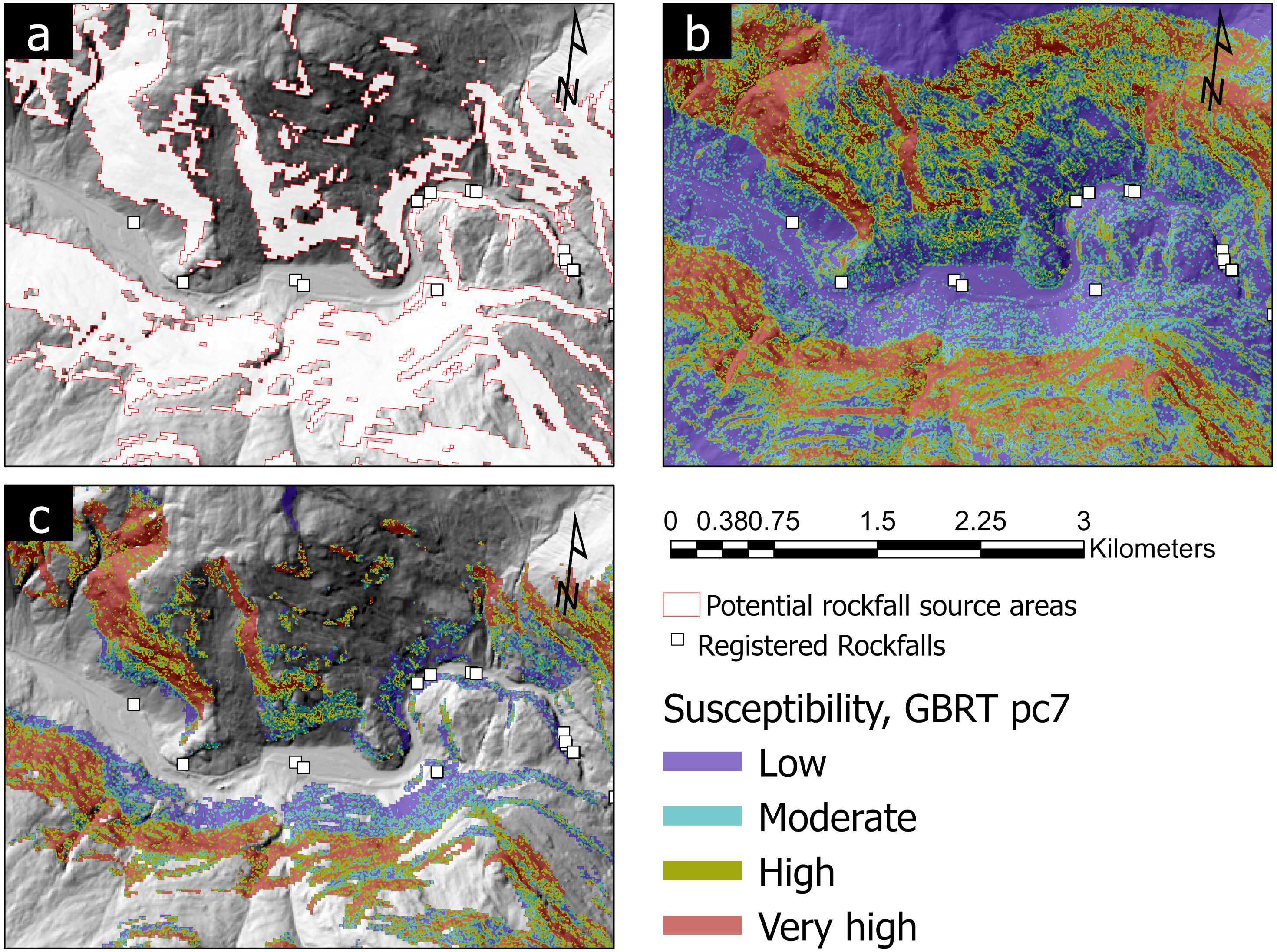

Figure 4.6: Map showing low, moderate, high, and very high rockfall source area susceptibility modeled with the GBRT *pc*7 model in a selected part of the training area (Figure 4.4). Classes are defined in Table 4.5. Resolution 10x10m. (a) Potential rockfall source areas from the national susceptibility map (Derron, 2010). (b) Modeled rockfall susceptibility for the entire selected area. (c) Modeled rockfall susceptibility clipped to the extent of the national potential rockfall source areas from Derron (2010).

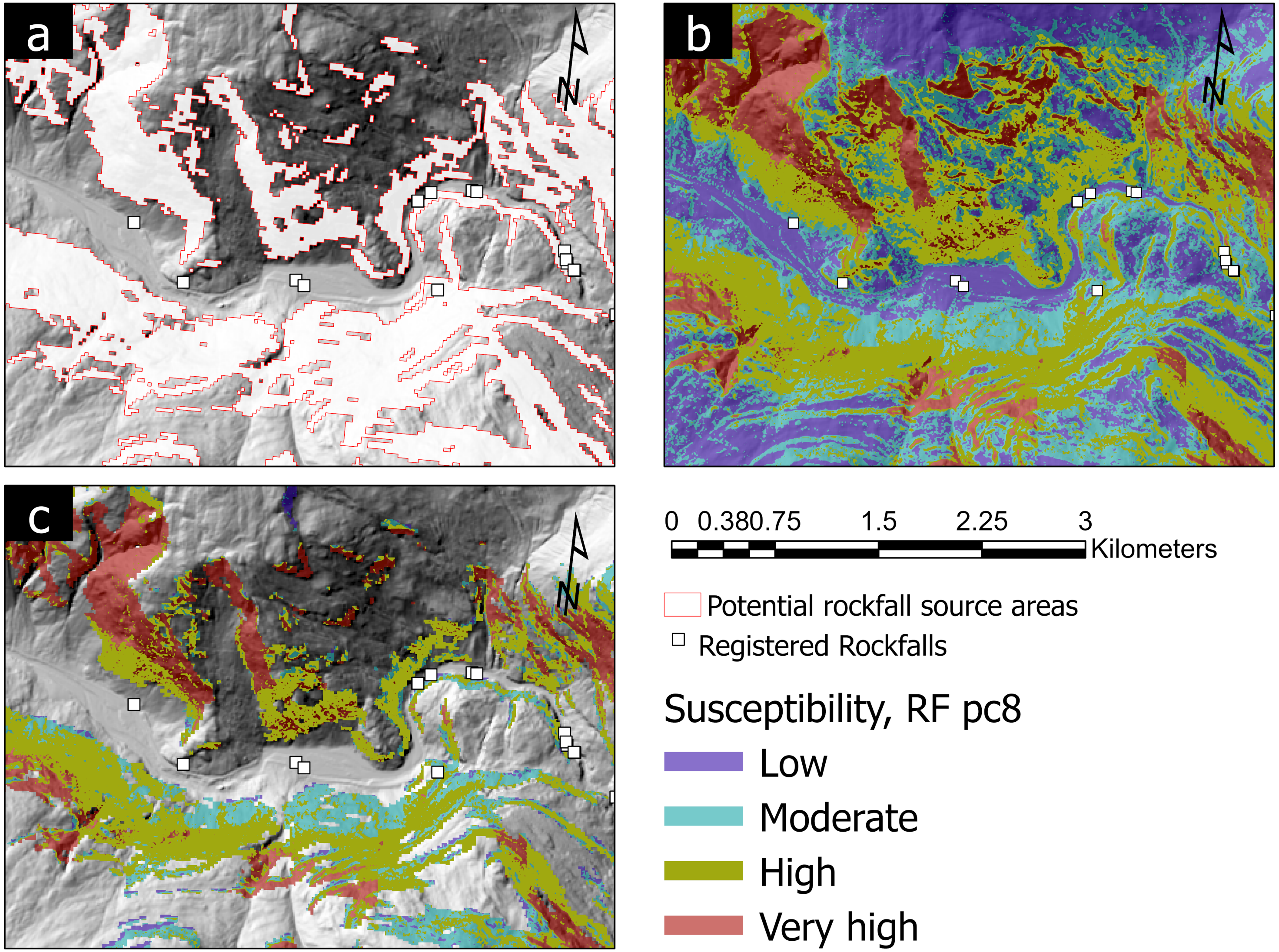

Figure 4.7: Map showing low, moderate, high, and very high rockfall source area susceptibility modeled with the RF *pc*8 model in a selected part of the training area (Figure 4.4). Classes are defined in Table 4.5. Resolution 10x10m. (a) Potential rockfall source areas from the national susceptibility map (Derron, 2010). (b) Modeled rockfall susceptibility for the entire selected area. (c) Modeled rockfall susceptibility clipped to the extent of the national potential rockfall source areas from Derron (2010).

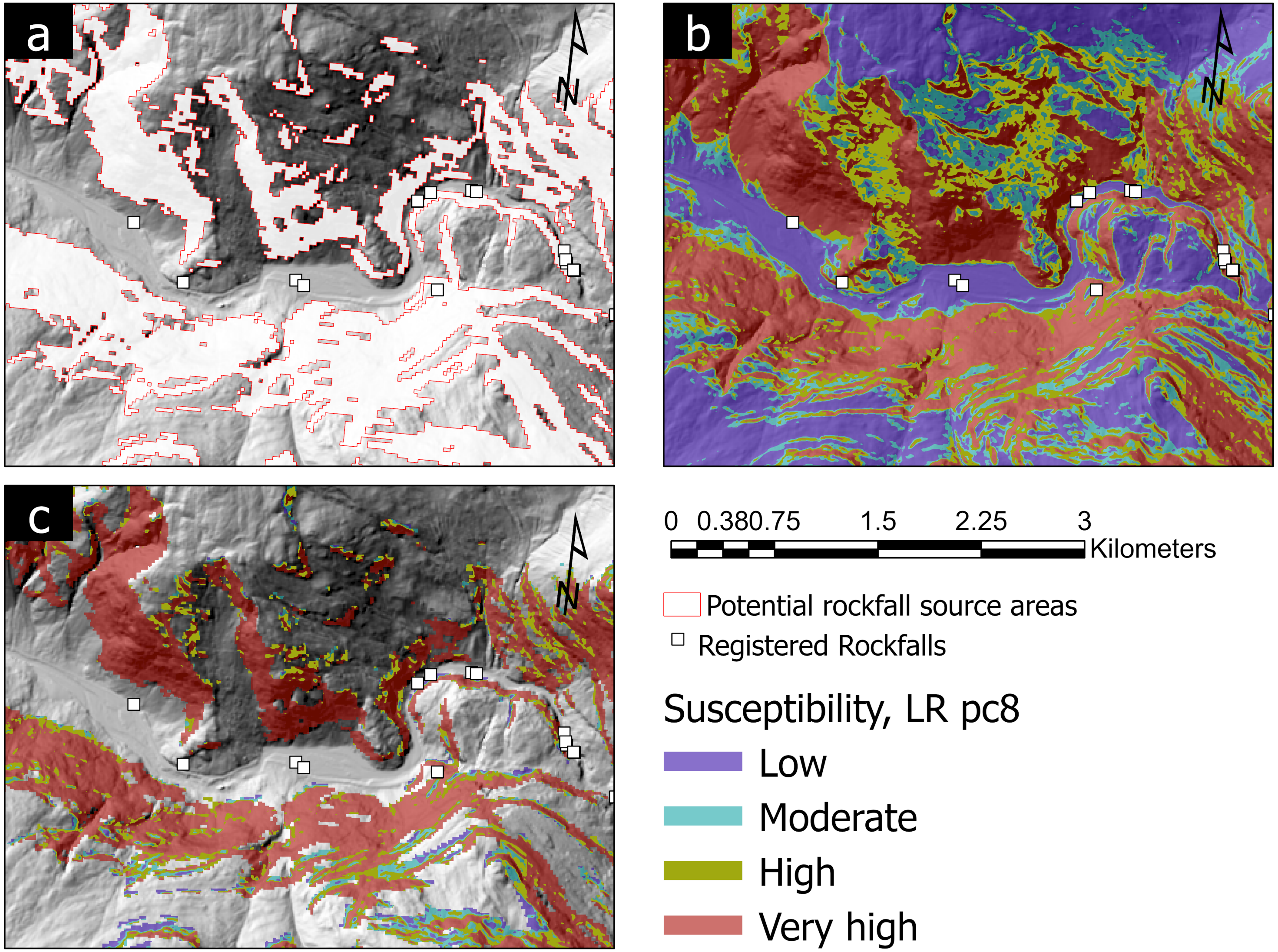

Figure 4.8: Map showing low, moderate, high, and very high rockfall source area susceptibility modeled with the LR *pc*8 model in a selected part of the training area (Figure 4.4). Classes are defined in Table 4.5. Resolution 10x10m. (a) Potential rockfall source areas from the national susceptibility map (Derron, 2010). (b) Modeled rockfall susceptibility for the entire selected area. (c) Modeled rockfall susceptibility clipped to the extent of the national potential rockfall source areas from Derron (2010).

### 4.1.5 Regional implementation: Vestland susceptibility maps

A random area in Vestland County was selected in order to show the performance of the models in other parts of the county (Figure 3.9). The resulting maps (Figure 4.9 4.10, Figure 4.11 and 4.12) show that *pc*4 is the most conservative model of the three and *pc*8 the least conservative model of the three. The *pc*8 susceptibility map has an area of "very high" susceptibility almost exclusively to areas where rockfalls have been registered, while the *pc*4 susceptibility map has large areas of the "very high" class, also where there have not been any registered rockfalls.

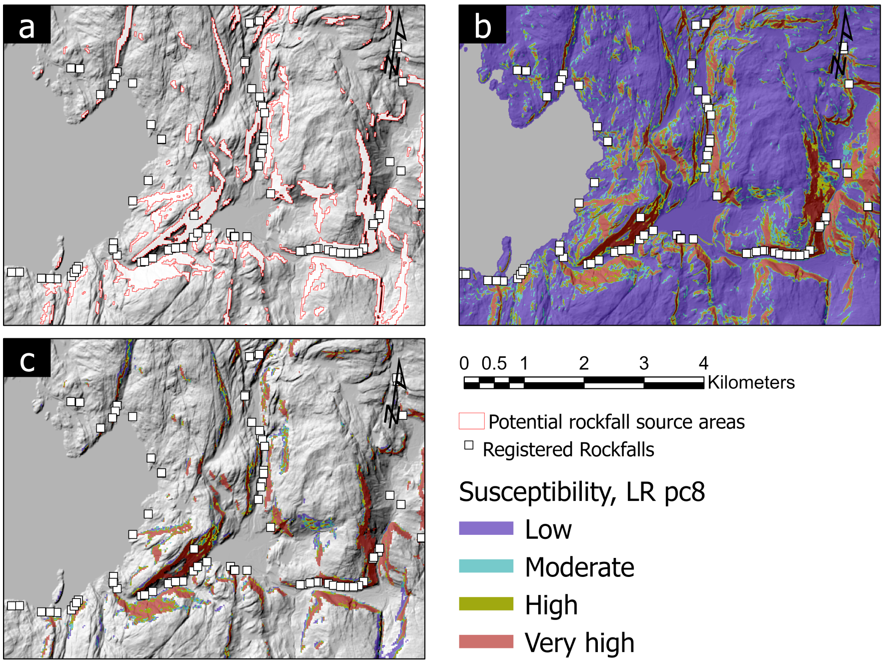

Figure 4.9: Map showing low, moderate, high, and very high rockfall source area susceptibility modeled with the RF *pc*4 model in a selected validation area in Vestland County (Figure 3.9). Classes are defined in Table 4.5. Resolution 10x10m. (a) Potential rockfall source areas from the national susceptibility map (Derron, 2010). (b) Modeled rockfall susceptibility for the selected area. (c) Modeled rockfall susceptibility clipped to the extent of the national potential rockfall source areas from Derron (2010)

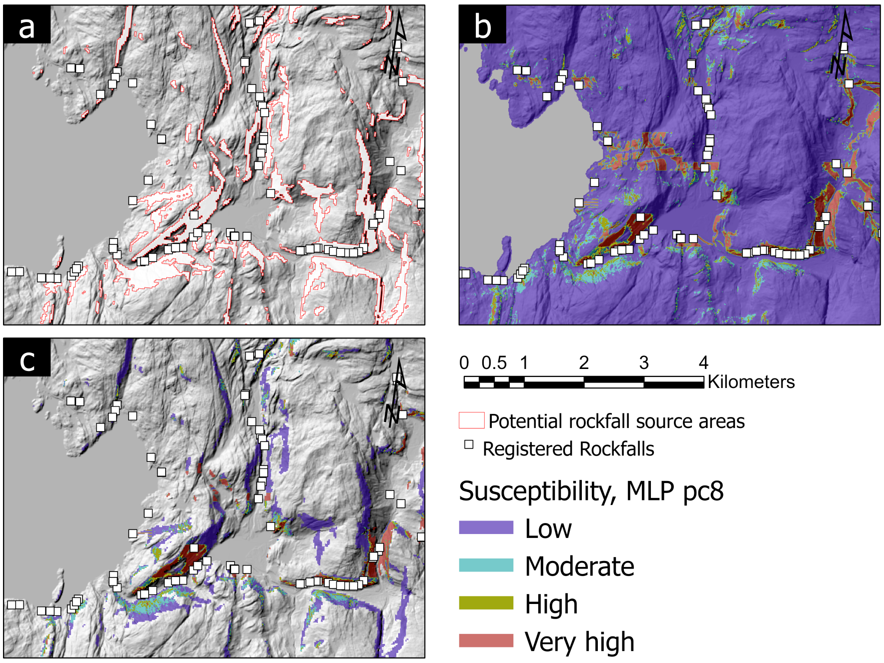

Figure 4.10: Map showing low, moderate, high, and very high rockfall source area susceptibility modeled with the RF *pc*7 model in a selected validation area in Vestland County (Figure 3.9). Classes are defined in Table 4.5. Resolution 10x10m. (a) Potential rockfall source areas from the national susceptibility map (Derron, 2010). (b) Modeled rockfall susceptibility for the selected area. (c) Modeled rockfall susceptibility clipped to the extent of the national potential rockfall source areas from Derron (2010)

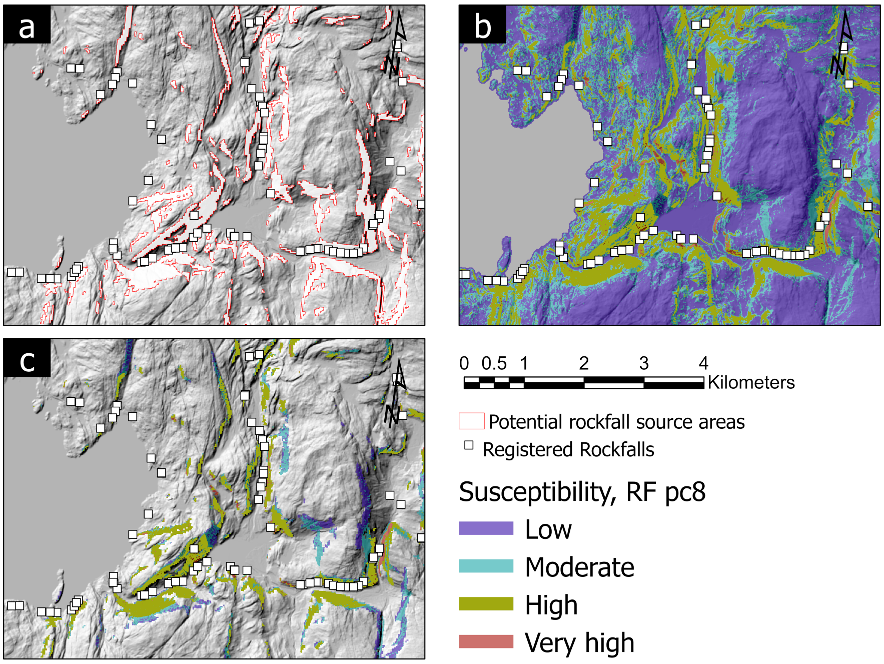

Figure 4.11: Map showing low, moderate, high, and very high rockfall source area susceptibility modeled with the RF *pc7* model in a selected validation area in Vestland County (Figure 3.9). Classes are defined in Table 4.5. Resolution 10x10m. (a) Potential rockfall source areas from the national susceptibility map (Derron, 2010). (b) Modeled rockfall susceptibility for the selected area. (c) Modeled rockfall susceptibility clipped to the extent of the national potential rockfall source areas from Derron (2010)

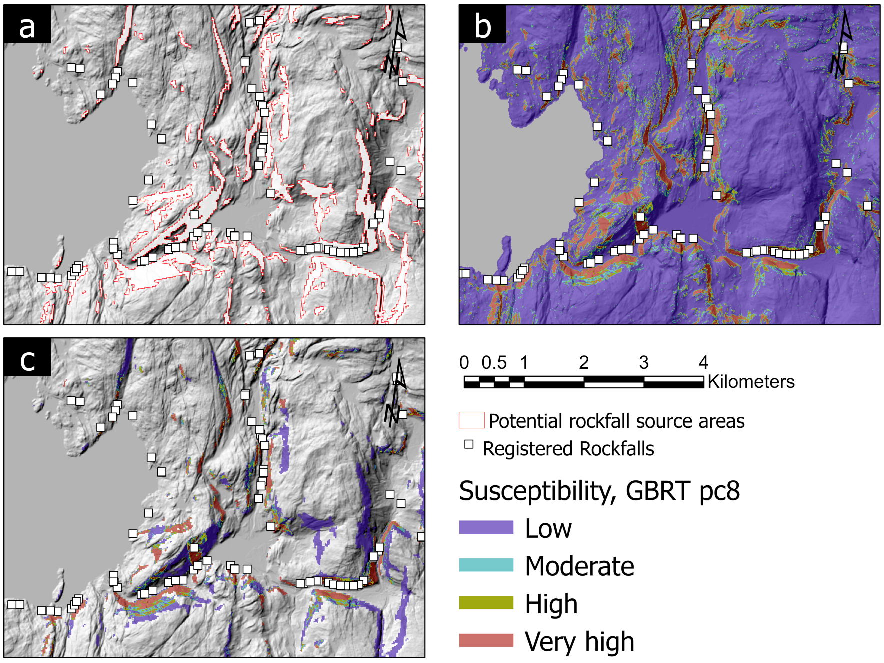

Figure 4.12: Map showing low, moderate, high, and very high rockfall source area susceptibility modeled with the GBRT *pc8* model in a selected validation area in Vestland County (Figure 3.9). Classes are defined in Table 4.5. Resolution 10x10m. (a) Potential rockfall source areas from the national susceptibility map (Derron, 2010). (b) Modeled rockfall susceptibility for the selected area. (c) Modeled rockfall susceptibility clipped to the extent of the national potential rockfall source areas from Derron (2010)

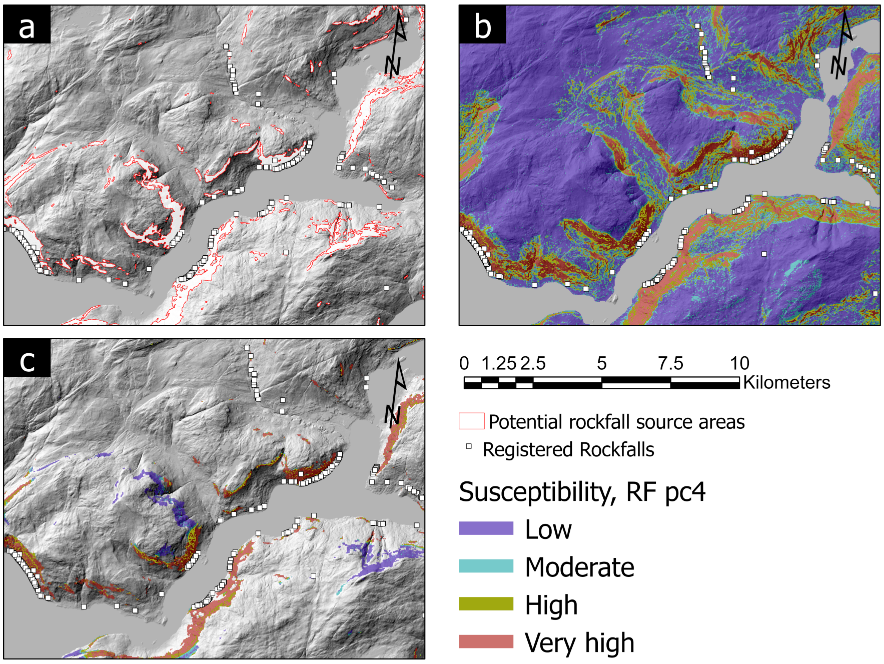

Figure 4.13: Map showing low, moderate, high, and very high rockfall source area susceptibility modeled with the RF *pc7* model in the area from Böhme et al. (2013) (Figure 3.9). Classes are defined in Table 4.5. Resolution 10x10m. (a) Potential rockfall source areas from the national susceptibility map (Derron, 2010). (b) Modeled rockfall susceptibility for the selected area. (c) Modeled rockfall susceptibility clipped to the extent of the national potential rockfall source areas from Derron (2010)

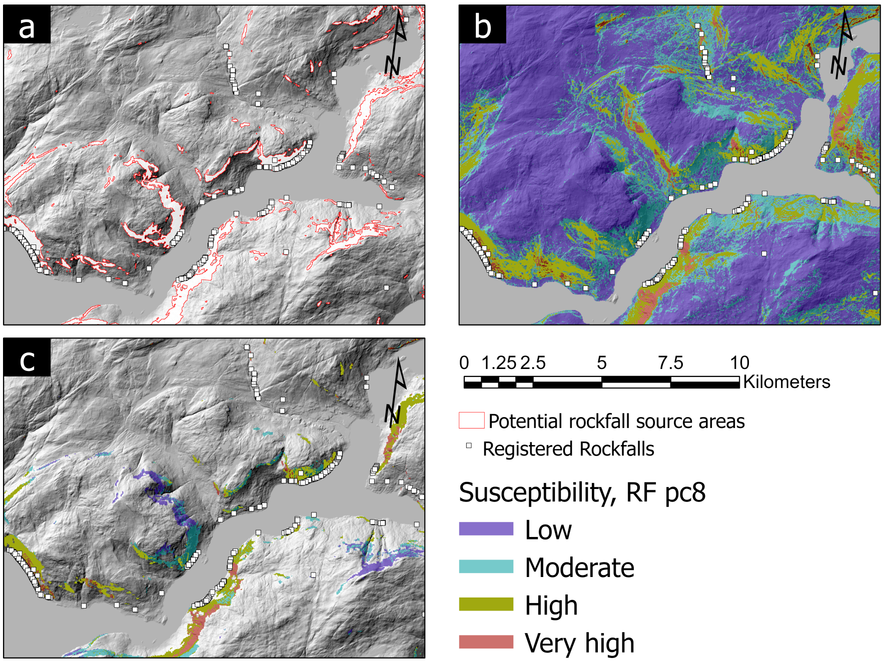

Figure 4.14: Map showing low, moderate, high, and very high rockfall source area susceptibility modeled with the RF *pc8* model in the area from Böhme et al. (2013) (Figure 3.9). Classes are defined in Table 4.5. Resolution 10x10m. (a) Potential rockfall source areas from the national susceptibility map (Derron, 2010). (b) Modeled rockfall susceptibility for the selected area. (c) Modeled rockfall susceptibility clipped to the extent of the national potential rockfall source areas from Derron (2010)

## 4.2 Meteorological analysis

### 4.2.1 The differences between the "rockfall climate" and "reference climate" in Vestland

These results do not account for whether the precipitation falls as rain or snow. The maximum daily precipitation value for the rockfall climate is 176.55 mm, compared to 87.29 mm for the reference climate (Table 4.6). The mean temperature of the rockfall database is 0.4 °C higher than the reference climate (Table 4.6). The standard deviation for daily precipitation in the rockfall climate is almost twice as large as in the reference climate. The difference in variation statistics is larger for daily precipitation than for daily mean temperature.

Table 4.6: Variations in SeNorge2 daily mean temperature and daily precipitation for the rockfall and reference climates. Given as mean, minimum, maximum, and standard deviation. Databases are described in Section 3.3.2 and 3.3.3. A skewness value $> 0$ shows that the tail is to the right of the distribution, while a skewness value $< 0$ shows that the tail is to the left of the distribution (Zwillinger and Kokoska, 2000).

| | **Mean** | **Minimum** | **Maximum** | **Standard deviation** | **Skewness** |
|---|---|---|---|---|---|
| | **Daily precipitation [mm]** | | | | |
| **Rockfall climate** | 10.58 | 0 | 176.55 | 15.48 | 2.922 |
| **Reference climate** | 6.58 | 0.26 | 87.29 | 8.44 | 2.38 |
| | **Daily mean temperature [°C]** | | | | |
| **Rockfall climate** | 3.58 | -22.83 | 23.87 | 5.42 | 0.295 |
| **Reference climate** | 4.33 | -17.6 | 22.788 | 6.44 | -0.11 |

For both the rockfall climate data and the reference climate data, the distributions of daily precipitation, accumulated precipitation 3 days, accumulated precipitation 14 days, and the 14-day mean precipitation have a right-skewed shape (Figure 4.15).

The peaks for daily precipitation and accumulated 3 days precipitation is around zero for both rockfall climate and the reference climate. The peaks around 0 show that most days have low or no precipitation in Vestland. However, the peaks are higher in the reference climate than in the rockfall climate. The 90th percentile for daily precipitation in the rockfall climate is 28.94 mm, while the 99th percentile for daily precipitation in the reference climate is 38.56 mm (Table 4.7), showing that the approximately the 1% highest daily precipitation values in the reference climate are 9.62 mm higher than approximately the 10% highest daily precipitation values in the rockfall climate. The 3-days accumulated precipitation 99th percentile for reference climate is 87.40 mm, which nearly matches the 90th percentile for no rockfall climate, which is 84.92 mm (Table 4.7). Compared to the reference climate, the cumulative distribution function for rockfall climate is shifted to the right on the x-axis.

Peaks in both the reference and rockfall climates for accumulated precipitation 14 days are more evenly distributed, with values ranging between 50 and 100 mm. The 99th percentile for reference climate and the 90th percentile for rockfall climate are nearly identical (Figure 4.15c). The 99th percentile for the reference climate is 284.50 mm, while the 90th percentile for the rockfall climate is 292.29 mm (Table 4.7). Compared to the reference climate, the cumulative

Table 4.7: 90th, 95th and 99th percentiles of precipitation variables

| | | **Daily [mm]** | **Acc 3 days [mm]** | **Acc 14 days [mm]** | **Mean 14 days [mm]** |
|---|---|---|---|---|---|
| 90th percentile | Rockfall | 38.94 | 84.92 | 292.29 | 19.47 |
| | Reference | 17.39 | 46.93 | 174.45 | 12.46 |
| 95th percentile | Rockfall | 39.75 | 108.76 | 364.40 | 24.29 |
| | Reference | 23.64 | 60.12 | 215.77 | 15.41 |
| 99th percentile | Rockfall | 69.48 | 164.81 | 506.43 | 33.76 |
| | Reference | 38.55 | 87.49 | 284.50 | 20.32 |

distribution function for rockfall climate is shifted to the right on the x-axis. The peaks for the mean daily precipitation for a 14-days period are at lower precipitation values (Figure 4.15d). The peaks range from 0 to 10 mm of precipitation. The reference climate's 99th percentile nearly coincided with the rockfall climate's 90th percentile. They are respectively at 20.32 mm and 19.47 mm (Table 4.7). Compared to the reference climate, the cumulative distribution function for rockfall climate is shifted to the right on the x-axis.

All chosen precipitation variable empirical distributions have the same right-skewed shape for both the reference climate and the rockfall climate, indicating that they come from the same distributions. For all four precipitation variables, the tale is longer for rockfall climate than for reference climate, and all of the CDFs for rockfall are shifted right on the x-axis compared to the CDFs for reference climate. For accumulated precipitation 3 days, accumulated precipitation 14 days, and mean precipitation 14 days, the distance between the CDFs is more significant than for daily precipitation.

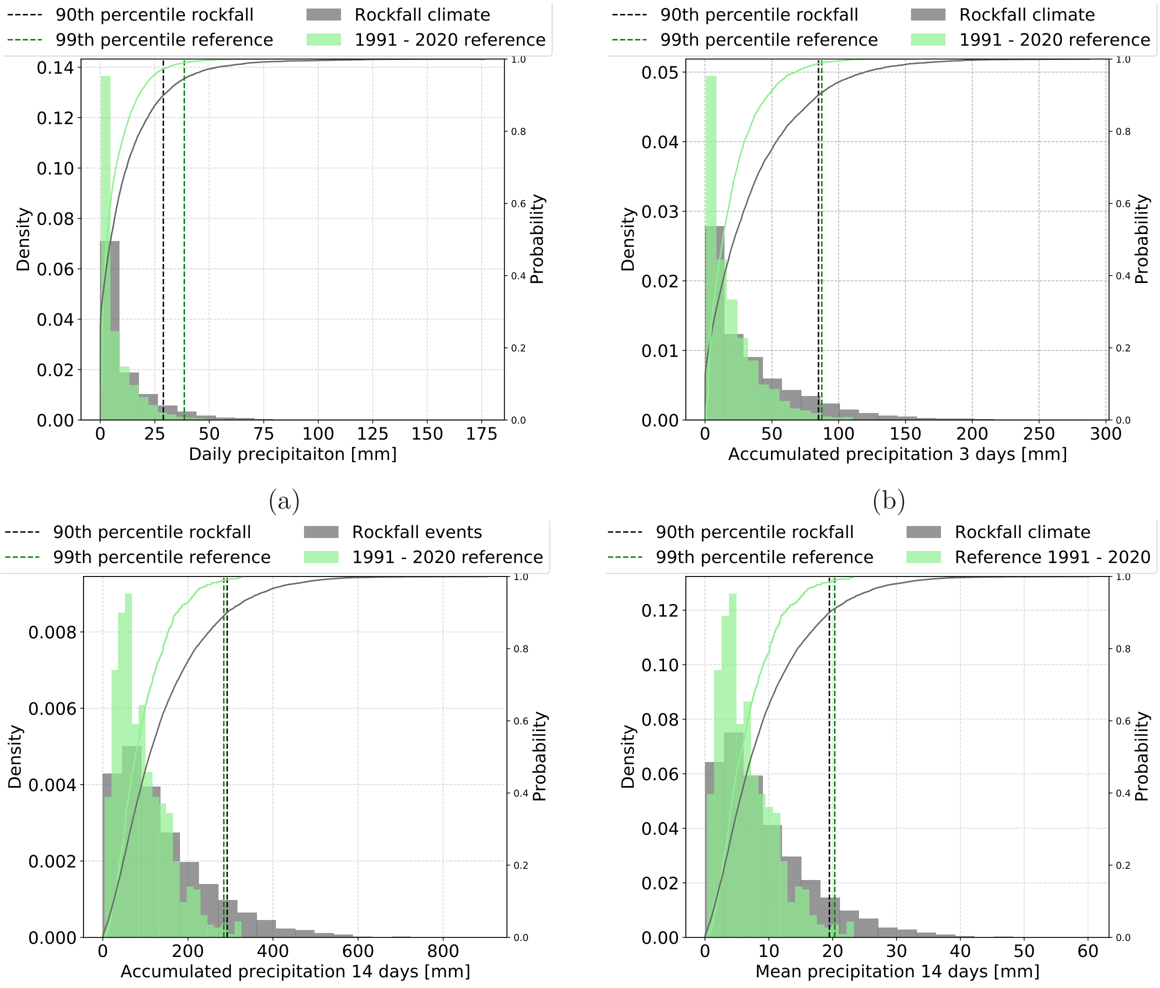

(a) (b)

(c) (d)

Figure 4.15: Histograms showing a) daily precipitation, b) 3 days accumulated precipitation, c) 14 days accumulated precipitation and d) mean precipitating for 14 days for the rockfall climate and reference climate. The total area of each histogram is equal to 1. Bins = 20

The difference between rockfall and reference climate was investigated for each season (Figure 4.16). Higher daily precipitation values are more likely in winter and autumn than in spring and summer, according to both databases. In autumn, 60% of rockfall events have daily precipitation of 10.6 mm or less, whereas 60% of days on the reference climate have daily precipitation of 5.9 mm or less (Table 4.8).

Table 4.8: Some selected cumulative probabilities for daily precipitation in autumn for reference climate and rockfall climate.

| | **Daily precipitation autumn [mm]** | | |
|---|---|---|---|
| **Cumulative probability** | **0.5** | **0.6** | **0.8** |
| **Reference climate** | 6.83 | 5.94 | 14.39 |
| **Rockfall climate** | 3.80 | 10.59 | 24.20 |

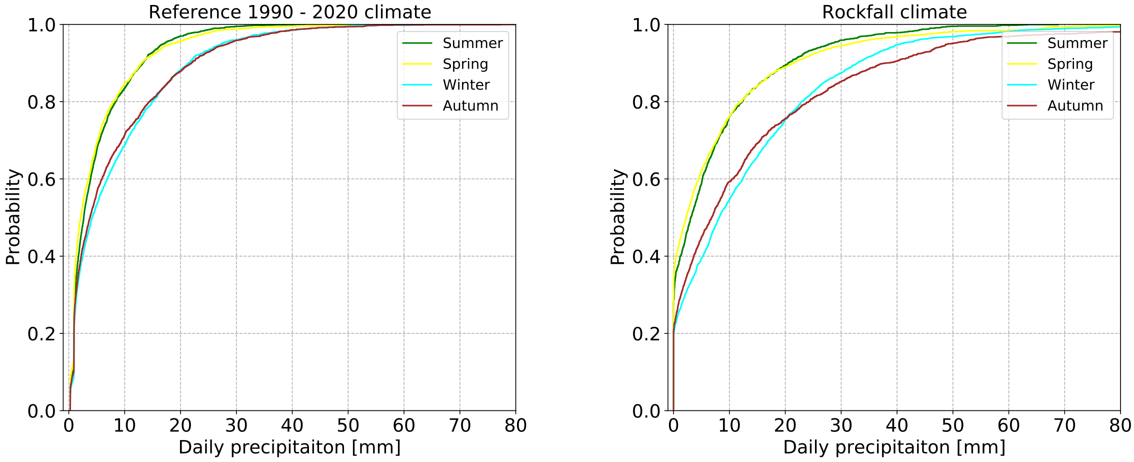

(a)

(b)

Figure 4.16: a) The cumulative probability function curve for daily precipitation for four seasons for the reference climate. b) The cumulative probability function curve for daily precipitation for four seasons for the rockfall climate.

The distributions for daily mean temperature and mean temperature for 14 days have a bimodal shape, where the distributions have two peaks (Figure 4.17). However, the second peak around 10 ◦C for daily mean temperature is significantly smaller for the rockfall climate than the reference climate. The peaks are around zero degrees and approximately 10 ◦C for daily mean temperature and around zero ◦C and 12 ◦C for mean temperature 14 days (Figure 4.17a,b). The peak around zero ◦C is higher for rockfall climate relative to the reference climate and the second peak around 10 - 12 ◦C is lower for rockfall climate relative to the reference climate. This is true for both daily mean temperature and mean temperature 14 days.

The differences in the temperature range 14 days and temperature variance 14 days distributions between reference climate and rockfall climate are small (Figure 4.17c, d). Both distributions are skewed to the right. The distributions of rockfall climate are slightly shifted to the right of the x-axis, as are the peaks. The mean daily temperature values for cumulative probabilities of 0.5, 0.6, and 0.8 for the four seasons are shown in Table 4.18 temp. Summer values are more similar between reference climate and rockfall climate than the other seasons. In spring, the daily mean temperature values for the rockfall climate are lower than the reference climate, and in winter, summer, and autumn, the daily mean temperature values for rockfall climate are higher than the reference climate. The 0.8 probability is an exception in summer when the mean daily temperature for the reference climate is higher than for the rockfall climate.

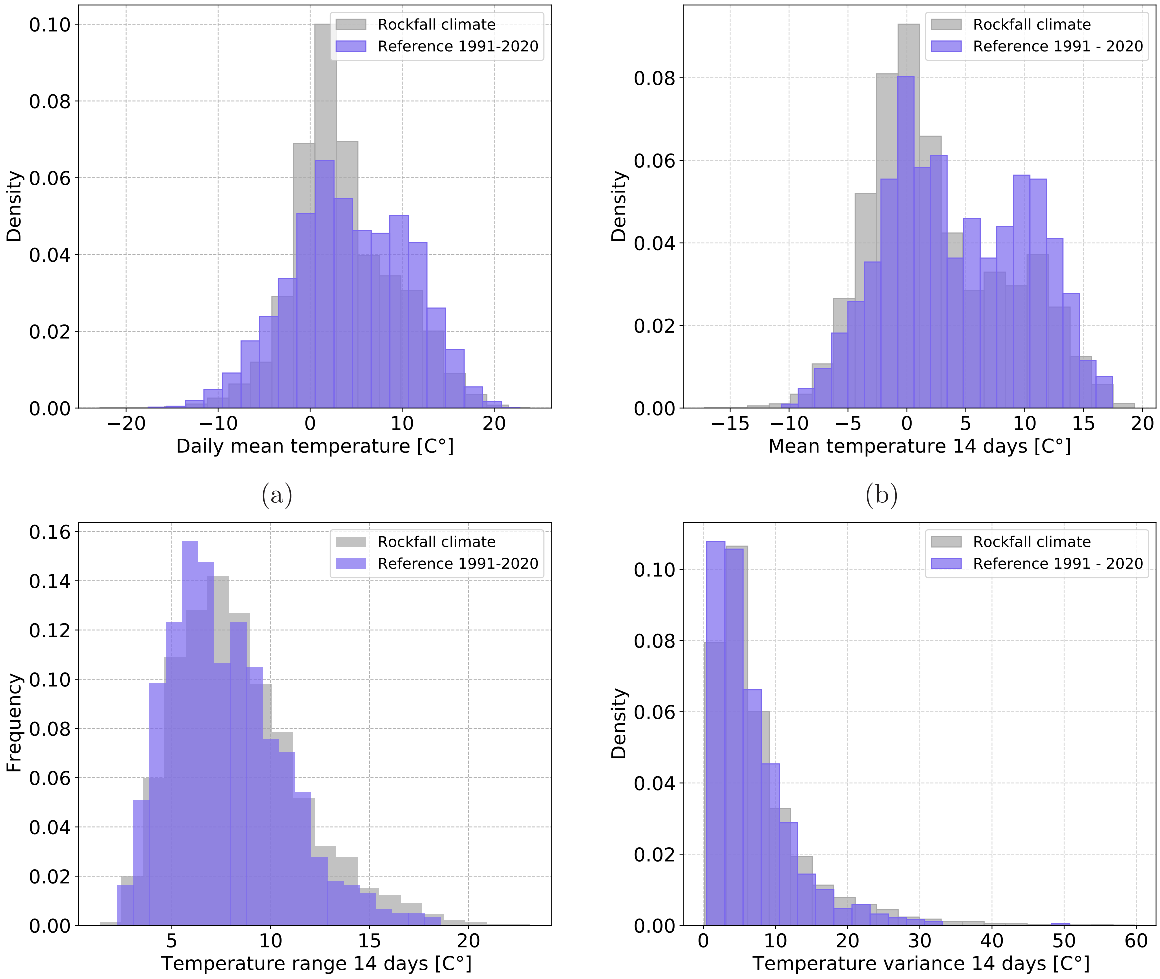

(a) (b) (c) (d)

Figure 4.17: Histograms showing daily mean temperature, mean temperature 14 days, temperature range 14 days and temperature variance 14 days for the rockfall climate and reference climate. The total area of each histogram is equal to 1. Bins = 20

The cumulative density function displays the probability of having any value up to each value at the x-axis. The gradient of the CDF curve at that value equals the probability density (Section 3.3.4). The CDFs for each season (summer, spring, winter, and autumn) are plotted to observe seasonal temperature variation (4.18), these distributions can be identified as normal distributions. The CDFs for winter and spring in the rockfall climate are steeper around zero °C than in the reference climate. This means, that the peak of the probability density function is higher around zero for the rockfall climate than the reference climate for winter and spring.

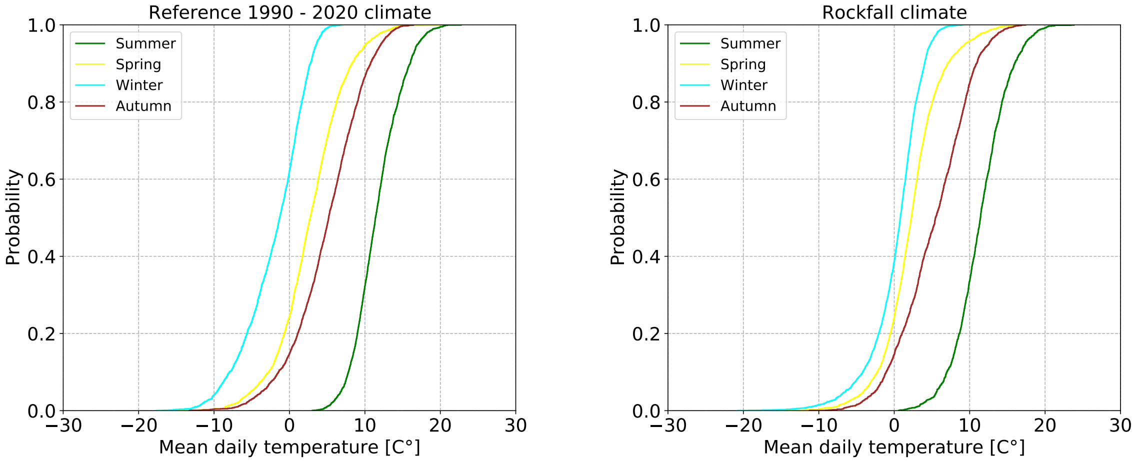

(a)

(b)

Figure 4.18: a). The cumulative probability function curve for mean daily temperature for summer, spring, winter, autumn for the reference climate. b)The cumulative probability function curve for mean daily temperature for summer, spring, winter, autumn for the rockfall climate.

### 4.2.2 The Kruskal-Wallis H-test

The Kruskal-Wallis test results show that the difference in median daily precipitation between the reference climate and the rockfall climate is not significant at a significance level of 0.05 (Table 4.9). While there is a significant difference in the median between the other variables accumulated precipitation 3 and 14 days, mean precipitation 14 days, daily mean temperature, mean 14 temperature 14 days, temperature range 14 days, and temperature variance 14 days between the rockfall and reference climates.

P-values less than the significance level reject the null hypothesis, whereas a p-value greater than the significance level fails to reject the null hypothesis. A rejected null hypothesis demonstrates that reference climate and rockfall climate are derived from two different populations of data, which holds true for all variables except daily precipitation. However, the failure of a test to reject the null hypothesis does not necessarily imply that the null hypothesis is correct, or that the samples come from the same population of data. It means that with the chosen significance level, it is impossible to say with certainty that the medians of the two samples are different.

### 4.2.3 Estimated triggering weather types

The definition from D'Amato et al. (2016) (Section 2.4.1) was used to calculate freeze-thaw periods, negative cooling, and negative warming. Table 4.10 divides weather types into three major categories: freeze-thaw, freeze, and no freeze, as well as the percentage of events in each

Table 4.9: Results from the Kruskal-Wallis test.

| Variable | Chi-squared | df | p-value | test results |
|---|---|---|---|---|
| | | Precipitation | | |
| **Daily** | 0.935 | 1 | 0.33 | No significant difference |
| **Accumulated 3 days** | 198.75 | 1 | $3.91 * 10^{-45}$ | Significant difference |
| **Accumulated 14 days** | 103.75 | 1 | $2.3 * 10^{-24}$ | Significant difference |
| **Mean 14 days** | 65.92 | 1 | $4.40 * 10^{-16}$ | Significant difference |
| | | Temperature | | |
| **Daily mean** | 125.17 | 1 | $4.67 * 10^{-29}$ | Significant difference |
| **Mean 14 days** | 60.79 | 1 | $6.36 * 10^{-15}$ | Significant difference |
| **Range 14 days** | 25.91 | 1 | $3.58 * 10^{-7}$ | Significant difference |
| **Variance 14 days** | 14.53 | 1 | $1.38 * 10^{-4}$ | Significant difference |

category. In Vestland, 57.7 % of rockfall events occurred during a Freeze-thaw period with mean daily temperatures above and below zero degrees. 39.1% of events (during a freeze-thaw period) experienced thawing on the event day. On the event day, 10.8 % of the events experienced negative cooling, while 7.8 % experienced negative warming.

The decision to use the 99th percentile for 14 days accumulated precipitation in the reference climate as a threshold for rockfalls estimated triggered by precipitation (Table 4.10) was made because these values roughly represent the 90th percentile for the rockfall climate, so precipitation values above this threshold are approximately 10% of the highest values for the rockfall climate and approximately 1% of the highest values for the reference climate (Figure 4.15). 3.3 % of the rockfall events were in a freeze period with exclusively negative mean daily temperatures.

Table 4.10: Weather type as the estimated triggering mechanism for rockfall occurrences in Vestland County. Divided into three weather categories: freeze-thaw, freeze and no freeze. Freeze-thaw periods, negative cooling, negative warming, and thawing are defined after D'Amato et al. (2016)).

| **Category** | **Weather type** | **Count** | **Percentage of events [%]** | **Percentage of category [%]** |
|---|---|---|---|---|
| **Freeze-thaw** | Freeze-thaw periods (14 days) | 7807 | 57.7 | 100 |
| | Thawing at event day | 5294 | 39.1 | 67.81 |
| | Negative cooling at event day | 1055 | 10.8 | 13.51 |
| | Negative warming at event day | 1458 | 7.8 | 18.68 |
| | 284.5 mm 14 days accumulated precipitation | 1069 | 7.89 | 13.69 |
| **Freeze** | Freeze periods (14 days) | 675 | 4.98 | 100 |
| | Negative cooling at event day | 422 | 3.3 | 62.52 |
| | Negative warming at event day 233 1.72 | 233 | 1.72 | 34.52 |
| | 284.5 mm 14 days accumulated precipitation | 22 | 0.16 | 3.26 |
| **No freeze** | No-freeze periods (14 days) | 5734 | 37.4 | 100 |
| | 284.5 mm 14 days accumulated precipitation | 381 | 2.68 | 7.53 |
| | Extremely high temperatures (> 20 C) | 15 | 0.11 | 0.30 |
| **Suggested triggering weather type** | Only Freeze-thaw | 6738 | 49.76 | 78.26 |
| | Freeze-thaw and/or rainfall | 1069 | 7.89 | 12.42 |
| | Rainfall in no freeze period | 381 | 2.81 | 4.43 |
| | Freeze period with negative cooling | 422 | 3.12 | 4.90 |
| | Total | 8610 | 63.58 | 100 |
| **Unknown trigger** | | 4931 | 36.42 | 100 |

### 4.2.4 Logistic regression models

*The null model* is a logistic intercept-only model with no predictors (Figure 4.19). It displays the estimated probabilities of rockfall occurrence based on the number of events in the rockfall inventory and shows how they vary by location and month.

These observations can be made from the null model's probabilities:

- January, February, and March are chaotic with a relatively high number of rockfall events and relatively high difference in rockfall probability between locations.
- Months June, July, and August has relatively low rockfall occurrence probability and the probability is more uniform between locations.
- April and May has a higher probability of rockfall occurrence than June, July, and August, but lower than January, February and March. Smaller variation between locations than January, February, and March. Larger variation between locations than June, July, and August.
- The probability of rockfall occurrence and variability between locations increases in September, October, November, and December.

The slope, $b_1$, of the simple logistic regression model with daily mean as a predictor, $LR1$, varies between -0.4 and 0.4 (Figure 4.20, 4.21 and 4.22). It is possible to observe a general pattern in the slopes. $b_1$ has a general pattern of being lower in the spring and early summer than in the winter. The difference in slope between spring and summer varies with the 16 locations. For some locations, the slope in spring is lower than the slope in summer, while for others, the opposite is true. In comparison to the other locations, the standard error for all months in Locations 13 and 16 is large.

The p-value of a slope estimate indicates whether or not the predictor is a meaningful addition to the model (Table 4.11). This means that a change in the value of the predictor changes the response variable and that the predictor improves the model. For some months in each location, the daily mean temperature is a significant predictor. However, there are no locations where the slope is significant for all months. Table B1 and B2 shows the results for the remaining months.

The slope $b_{1_2}$, of the simple logistic regression model with daily precipitation as a predictor, $Lr_2$ varies between -0.1 and 0.1. The effect of precipitation is consistent with no effect because the slopes are close to zero. The general pattern is that the slope is smallest in spring (March, April, and May) and largest in summer (June, July, August), but this pattern varies with locations. Table 4.12 shows the regression results for September to May and Table B3 and B4 shows the results from the remaining months.

A multiple logistic regression model with mean temperature, daily precipitation, and the interaction term of mean temperature and daily precipitation as predictors, $LR_3$, was also fitted for Vestland County as a region, not considering the 16 locations. Table 4.13 show the AIC values from the Akaike information criterion method. The smallest AIC value is for the $Lr_2$ model with daily precipitation as predictor in July.

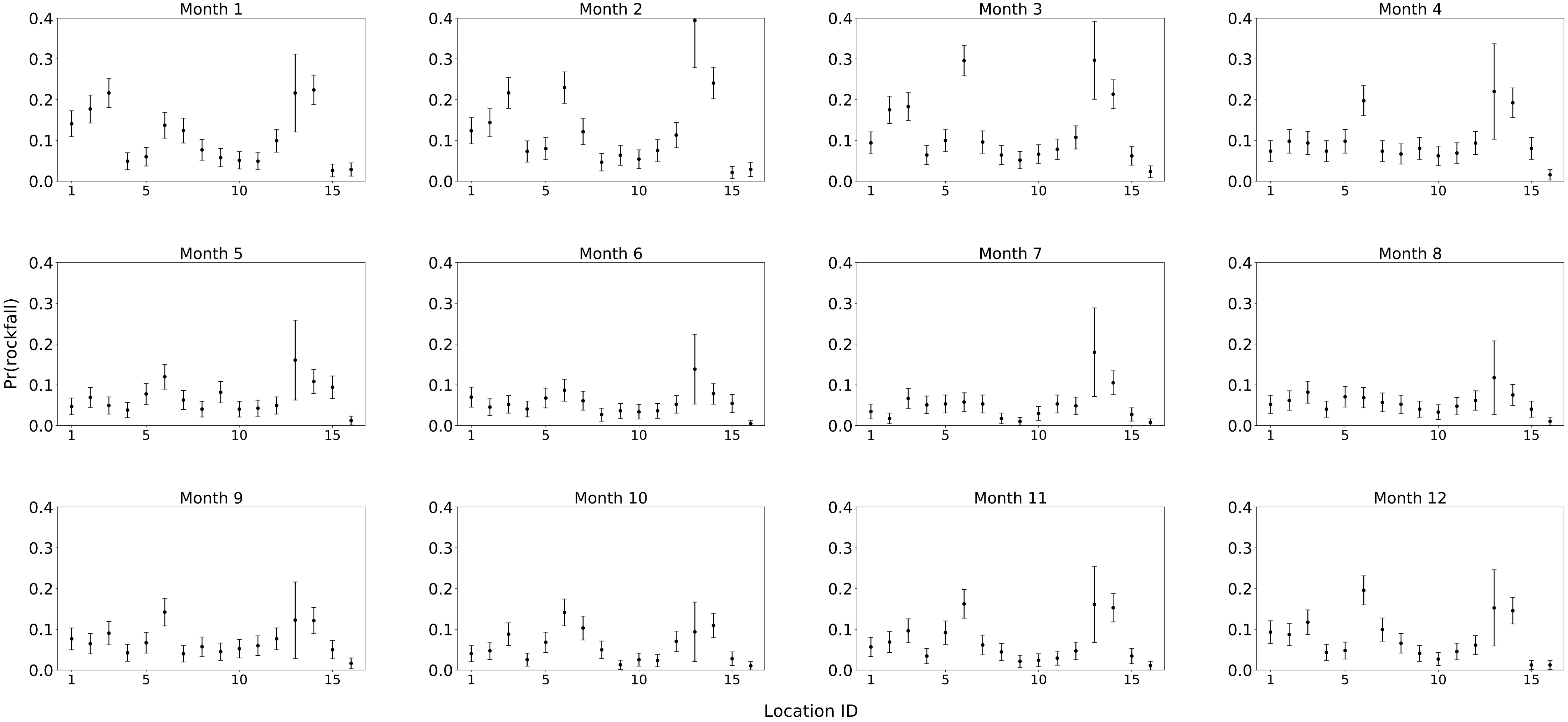

Figure 4.19: Probabilities from the null model with no predictors. Two standard errors (SE) as error bars. Probability is on the y-axis, location ID (1-16) is on the x-axis. Month 1 is January and month 12 is December.

Table 4.11: $LR_1$ model results from January to April. Mean daily temperature as a predictor. The table shows the intercept and slope estimates, as well as the associated standard errors and p-values.

| | **Month** | | | | | | | | | | | |
|---|---|---|---|---|---|---|---|---|---|---|---|---|
| **Location ID** | Jan | | | | | | Feb | | | | | |
| | **Intercept estimate** | **SE** | **p < 0.05** | **Slope estimate** | **SE** | **p < 0.05** | **Intercept estimate** | **SE** | **p < 0.05** | **Slope estimate** | **SE** | **p < 0.05** |
| **1** | -2.204 | 0.175 | yes | 0.037 | 0.009 | yes | -2.201 | 0.194 | yes | 0.029 | 0.013 | yes |
| **2** | -2.090 | 0.168 | yes | 0.065 | 0.012 | yes | -2.161 | 0.184 | yes | 0.053 | 0.014 | yes |
| **3** | -1.730 | 0.149 | yes | 0.033 | 0.007 | yes | -1.667 | 0.150 | yes | 0.031 | 0.007 | yes |
| **4** | -3.095 | 0.269 | yes | 0.015 | 0.016 | no | -3.156 | 0.274 | yes | 0.061 | 0.014 | yes |
| **5** | -2.784 | 0.246 | yes | 0.006 | 0.027 | no | -2.448 | 0.221 | yes | 0.001 | 0.030 | no |
| **6** | -2.209 | 0.172 | yes | 0.062 | 0.015 | yes | -1.473 | 0.134 | yes | 0.061 | 0.016 | yes |
| **7** | -2.423 | 0.192 | yes | 0.057 | 0.013 | yes | -2.609 | 0.212 | yes | 0.080 | 0.015 | yes |
| **8** | -2.647 | 0.208 | yes | 0.064 | 0.035 | no | -3.216 | 0.282 | yes | 0.102 | 0.057 | no |
| **9** | -3.021 | 0.261 | yes | 0.021 | 0.013 | no | -3.315 | 0.283 | yes | 0.047 | 0.011 | yes |
| **10** | -3.157 | 0.285 | yes | 0.019 | 0.012 | no | -2.928 | 0.276 | yes | 0.006 | 0.016 | no |
| **11** | -3.336 | 0.289 | yes | 0.035 | 0.013 | yes | -3.098 | 0.268 | yes | 0.063 | 0.015 | yes |
| **12** | -2.474 | 0.202 | yes | 0.025 | 0.010 | yes | -2.210 | 0.195 | yes | 0.020 | 0.014 | no |
| **13** | -1.488 | 0.358 | yes | 0.017 | 0.017 | no | -0.369 | 0.314 | no | -0.009 | 0.031 | no |
| **14** | -1.690 | 0.142 | yes | 0.043 | 0.008 | yes | -1.194 | 0.126 | yes | 0.008 | 0.011 | no |
| **15** | -3.562 | 0.361 | yes | -0.008 | 0.030 | no | -4.342 | 0.476 | yes | 0.059 | 0.024 | yes |
| **16** | -3.985 | 0.404 | yes | 0.053 | 0.024 | yes | -3.513 | 0.371 | yes | 0.000 | 0.041 | no |
| | March | | | | | | April | | | | | |
| **1** | -2.667 | 0.206 | yes | 0.038 | 0.010 | yes | -2.779 | 0.230 | yes | 0.036 | 0.015 | yes |
| **2** | -1.815 | 0.139 | yes | 0.033 | 0.008 | yes | -2.306 | 0.196 | yes | 0.022 | 0.025 | no |
| **3** | -1.809 | 0.143 | yes | 0.024 | 0.006 | yes | -2.494 | 0.202 | yes | 0.027 | 0.011 | yes |
| **4** | -2.846 | 0.230 | yes | 0.019 | 0.013 | no | -2.714 | 0.222 | yes | 0.032 | 0.017 | no |
| **5** | -2.168 | 0.180 | yes | -0.008 | 0.023 | no | -2.285 | 0.189 | yes | 0.021 | 0.028 | no |
| **6** | -0.892 | 0.103 | yes | 0.007 | 0.013 | no | -1.671 | 0.139 | yes | 0.081 | 0.020 | yes |
| **7** | -2.635 | 0.198 | yes | 0.050 | 0.012 | yes | -2.645 | 0.217 | yes | 0.029 | 0.024 | no |
| **8** | -2.771 | 0.219 | yes | 0.036 | 0.038 | no | -2.736 | 0.214 | yes | 0.052 | 0.033 | no |
| **9** | -3.120 | 0.278 | yes | 0.023 | 0.017 | no | -2.332 | 0.210 | yes | -0.022 | 0.025 | no |
| **10** | -2.539 | 0.224 | yes | -0.013 | 0.017 | no | -2.941 | 0.246 | yes | 0.027 | 0.013 | yes |
| **11** | -2.521 | 0.211 | yes | 0.008 | 0.016 | no | -2.626 | 0.225 | yes | 0.005 | 0.022 | no |
| **12** | -2.234 | 0.180 | yes | 0.015 | 0.012 | no | -2.343 | 0.193 | yes | 0.014 | 0.017 | no |
| **13** | -0.759 | 0.275 | yes | -0.019 | 0.029 | no | -1.391 | 0.409 | yes | 0.023 | 0.038 | no |
| **14** | -1.507 | 0.128 | yes | 0.027 | 0.009 | yes | -1.535 | 0.138 | yes | 0.022 | 0.015 | no |
| **15** | -2.887 | 0.236 | yes | 0.026 | 0.017 | no | -2.413 | 0.209 | yes | -0.006 | 0.026 | no |
| **16** | -3.469 | 0.372 | yes | -0.083 | 0.080 | no | -4.038 | 0.474 | yes | -0.033 | 0.086 | no |

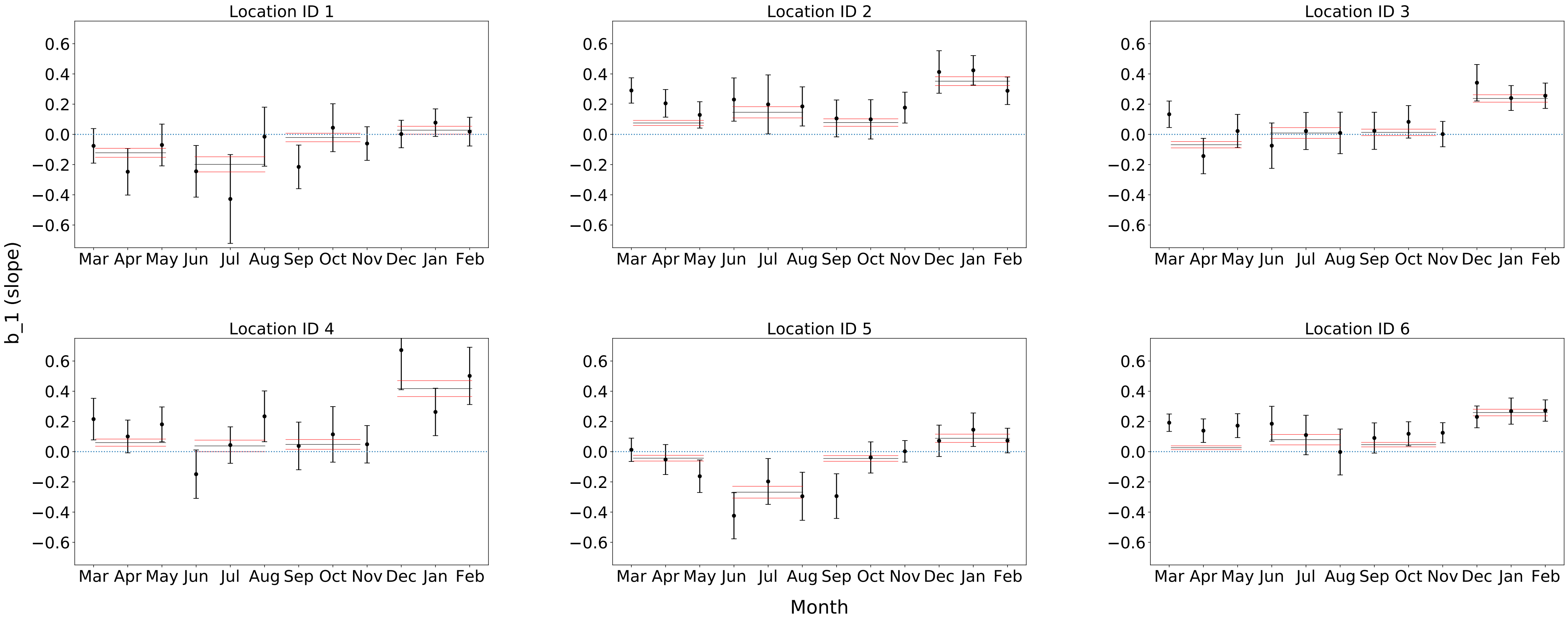

Figure 4.20: The coefficient for each location and month of the year from the logistic regression with daily mean temperature as a predictor. A solid horizontal black line is the estimate from the corresponding season (spring, summer, autumn, and winter). Red lines are the 95% confidence interval for the season. Two standard errors (SE) as error bar. Location 1 - 6.

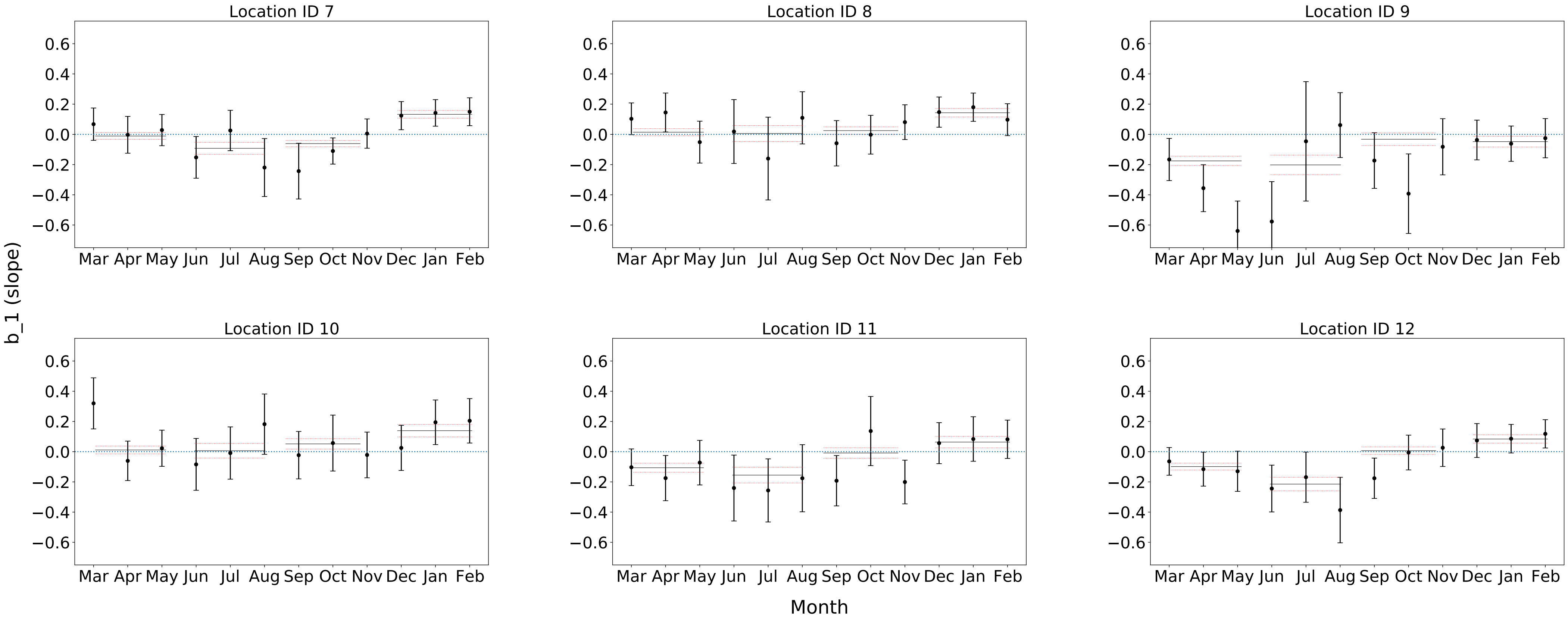

Figure 4.21: The coefficient for each location and month of the year from the logistic regression with daily mean temperature as a predictor. A solid horizontal black line is the estimate from the corresponding season (spring, summer, autumn, and winter). Red lines are the 95% confidence interval for the seasons. Two standard errors (SE) as error bar. Location 7 - 12

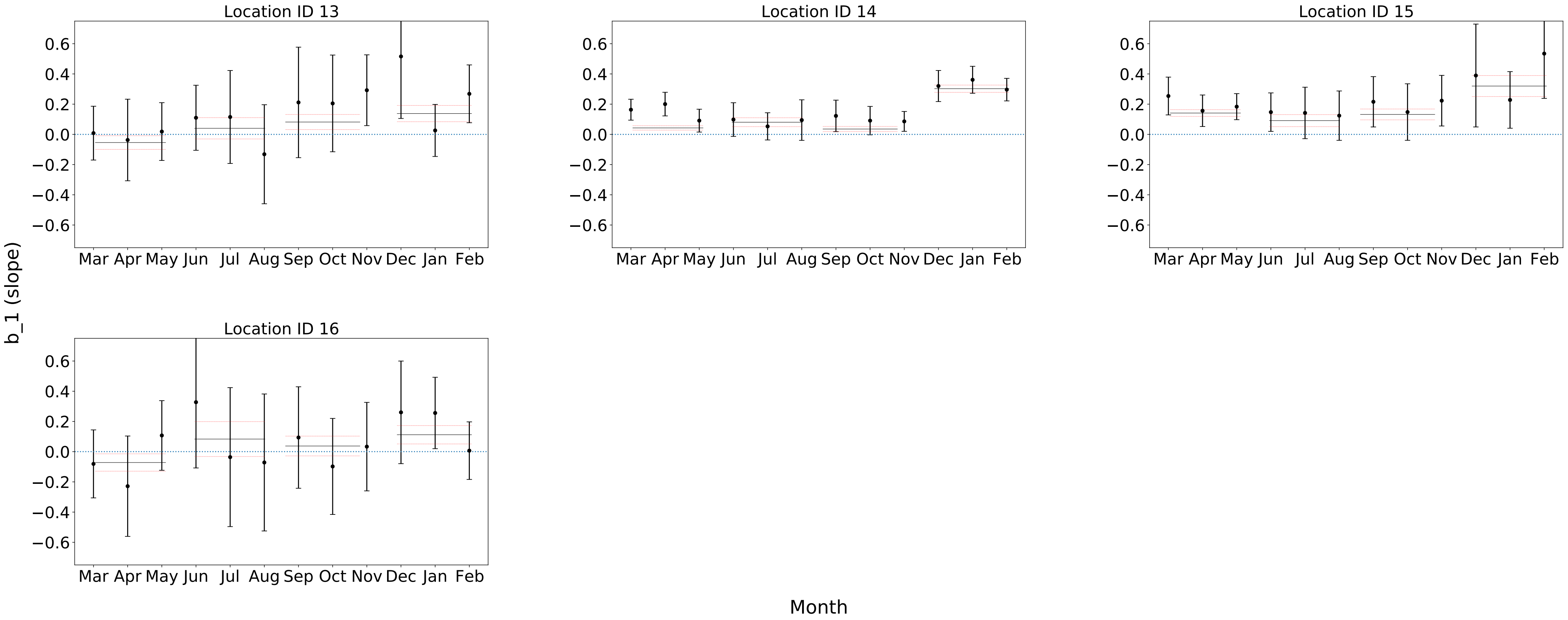

Figure 4.22: The coefficient for each location and month of the year from the logistic regression with daily mean temperature as a predictor. A solid horizontal black line is the estimate from the corresponding season (spring, summer, autumn, and winter). Red lines are the 95% confidence interval for the seasons. Two standard errors (SE) as error bar. Location 13 - 16

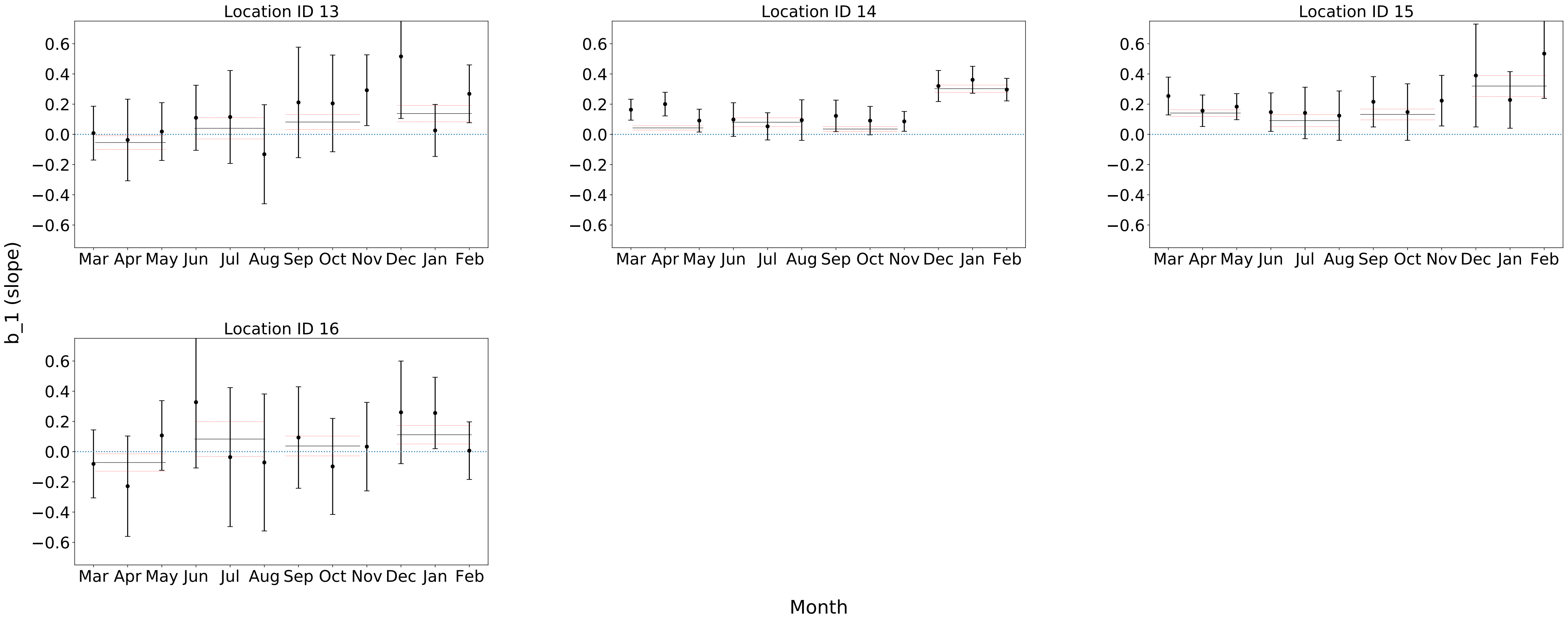

Figure 4.23: The coefficient for each location and month of the year from the logistic regression with daily mean temperature as a predictor. A solid horizontal black line is the estimate from the corresponding season (spring, summer, autumn, and winter). Red lines are the 95% confidence interval for the seasons. Two standard errors (SE) as error bar. Location 13 - 16.

Table 4.12: Model results with daily precipitation as a predictor for September to December.

| | Month | | | | | | | | | | | |
|---|---|---|---|---|---|---|---|---|---|---|---|---|
| **Location ID** | September | | | | | | October | | | | | |
| | **Intercept estimate** | **SE** | **p < 0.05** | **Slope estimate** | **SE** | **p < 0.05** | **Intercept estimate** | **SE** | **p < 0.05** | **Slope estimate** | **SE** | **p < 0.05** |
| **1** | -2.607 | 0.234 | yes | 0.011 | 0.012 | no | -3.478 | 0.345 | yes | 0.023 | 0.015 | no |
| **2** | -2.676 | 0.247 | yes | 0.001 | 0.022 | no | -3.075 | 0.293 | yes | 0.009 | 0.020 | no |
| **3** | -2.780 | 0.234 | yes | 0.028 | 0.007 | yes | -2.952 | 0.257 | yes | 0.033 | 0.008 | yes |
| **4** | -3.176 | 0.309 | yes | 0.007 | 0.020 | no | -3.665 | 0.391 | yes | 0.002 | 0.024 | no |
| **5** | -3.117 | 0.267 | yes | 0.059 | 0.015 | yes | -2.612 | 0.231 | yes | -0.001 | 0.020 | no |
| **6** | -2.338 | 0.190 | yes | 0.081 | 0.016 | yes | -2.233 | 0.184 | yes | 0.058 | 0.014 | yes |
| **7** | -3.200 | 0.311 | yes | 0.003 | 0.029 | no | -2.249 | 0.198 | yes | 0.011 | 0.015 | no |
| **8** | -3.130 | 0.277 | yes | 0.094 | 0.036 | yes | -3.116 | 0.258 | yes | 0.051 | 0.028 | no |
| **9** | -3.442 | 0.316 | yes | 0.028 | 0.011 | yes | -4.602 | 0.607 | yes | 0.020 | 0.026 | no |
| **10** | -4.039 | 0.371 | yes | 0.045 | 0.008 | yes | -3.387 | 0.373 | yes | -0.028 | 0.028 | no |
| **11** | -3.776 | 0.332 | yes | 0.050 | 0.009 | yes | -4.186 | 0.465 | yes | 0.033 | 0.018 | no |
| **12** | -2.563 | 0.231 | yes | 0.009 | 0.016 | no | -2.819 | 0.247 | yes | 0.020 | 0.011 | no |
| **13** | -1.925 | 0.510 | yes | -0.009 | 0.056 | no | -2.800 | 0.579 | yes | 0.048 | 0.026 | no |
| **14** | -2.413 | 0.205 | yes | 0.044 | 0.011 | yes | -2.611 | 0.213 | yes | 0.038 | 0.008 | yes |
| **15** | -2.963 | 0.281 | yes | 0.002 | 0.021 | no | -3.660 | 0.375 | yes | 0.011 | 0.019 | no |
| **16** | -4.262 | 0.518 | yes | 0.021 | 0.036 | no | -4.535 | 0.613 | yes | -0.003 | 0.047 | no |
| | November | | | | | | December | | | | | |
| **1** | -3.017 | 0.275 | yes | 0.018 | 0.012 | no | -2.576 | 0.221 | yes | 0.023 | 0.010 | yes |
| **2** | -3.031 | 0.266 | yes | 0.046 | 0.015 | yes | -2.399 | 0.221 | yes | 0.006 | 0.016 | no |
| **3** | -2.351 | 0.207 | yes | 0.009 | 0.009 | no | -2.383 | 0.198 | yes | 0.021 | 0.007 | yes |
| **4** | -3.069 | 0.322 | yes | -0.047 | 0.039 | no | -3.934 | 0.364 | yes | 0.048 | 0.011 | yes |
| **5** | -2.387 | 0.209 | yes | 0.018 | 0.020 | no | -2.722 | 0.272 | yes | -0.059 | 0.042 | no |
| **6** | -2.186 | 0.175 | yes | 0.075 | 0.013 | yes | -2.018 | 0.163 | yes | 0.070 | 0.011 | yes |
| **7** | -3.101 | 0.280 | yes | 0.046 | 0.018 | yes | -2.851 | 0.236 | yes | 0.057 | 0.012 | yes |
| **8** | -3.738 | 0.338 | yes | 0.151 | 0.034 | yes | -3.298 | 0.272 | yes | 0.155 | 0.030 | yes |
| **9** | -4.786 | 0.541 | yes | 0.049 | 0.013 | yes | -3.825 | 0.359 | yes | 0.039 | 0.011 | yes |
| **10** | -3.867 | 0.430 | yes | 0.013 | 0.019 | no | -3.830 | 0.410 | yes | 0.015 | 0.014 | no |
| **11** | -3.508 | 0.373 | yes | 0.000 | 0.026 | no | -3.469 | 0.316 | yes | 0.031 | 0.012 | yes |
| **12** | -3.363 | 0.313 | yes | 0.031 | 0.014 | yes | -3.084 | 0.274 | yes | 0.025 | 0.010 | yes |
| **13** | -2.125 | 0.435 | yes | 0.064 | 0.028 | yes | -2.151 | 0.491 | yes | 0.038 | 0.023 | no |
| **14** | -1.814 | 0.165 | yes | 0.013 | 0.011 | no | -2.481 | 0.192 | yes | 0.044 | 0.007 | yes |
| **15** | -3.479 | 0.356 | yes | 0.018 | 0.024 | no | -4.757 | 0.593 | yes | 0.030 | 0.023 | no |
| **16** | -4.448 | 0.615 | yes | -0.010 | 0.056 | no | -4.391 | 0.571 | yes | 0.001 | 0.044 | no |

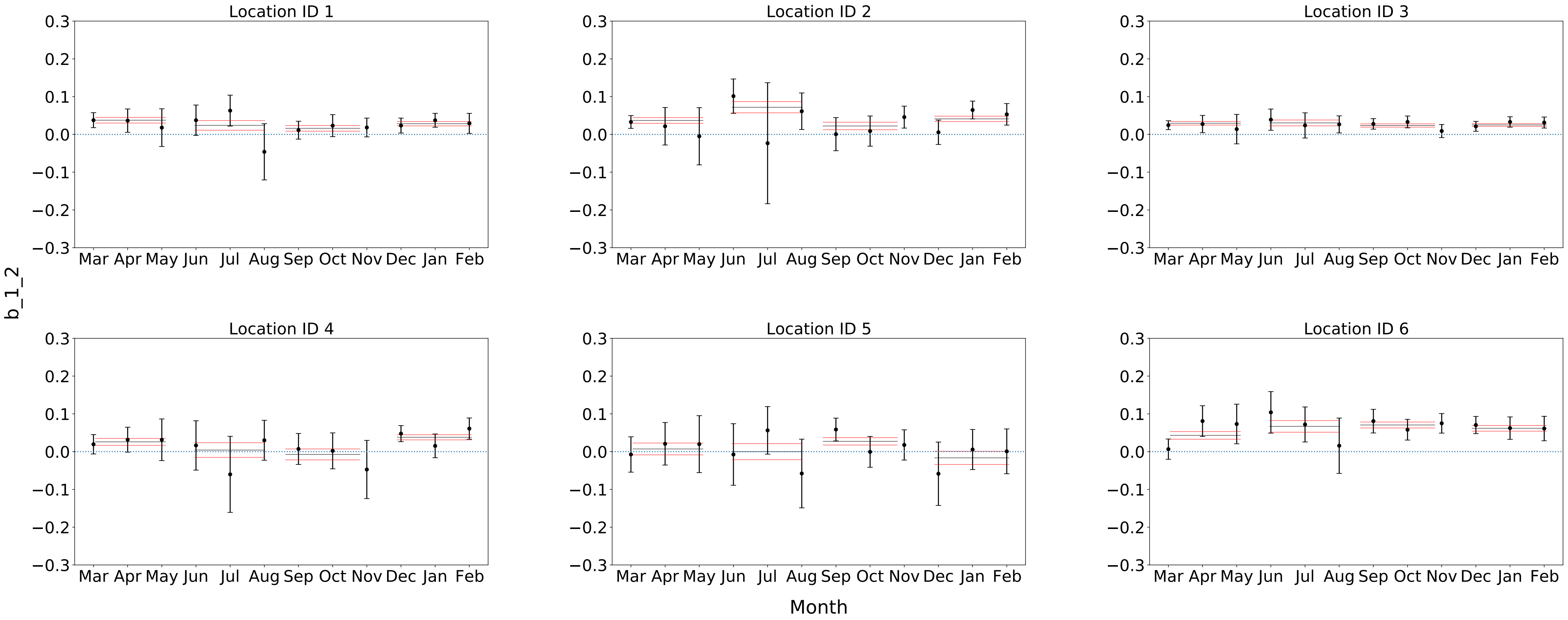

Figure 4.24: The coefficient for each location and month of the year from the logistic regression with daily precipitation as a predictor. A solid horizontal black line is the estimate from the corresponding season (spring, summer, autumn, and winter). Red lines are the 95% confidence interval for the seasons. Two standard errors (SE) as error bar. Location 1 - 6.

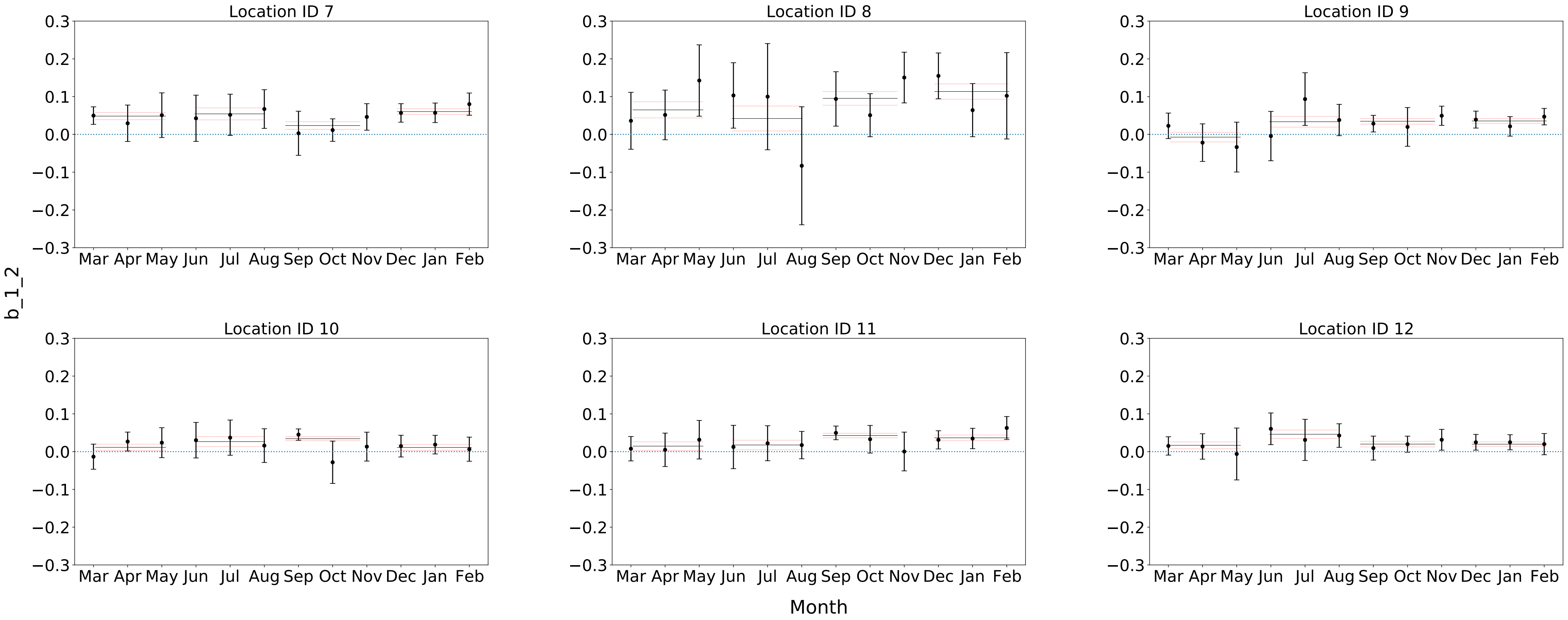

Figure 4.25: The coefficient for each location and month of the year from the logistic regression with daily precipitation as a predictor. A solid horizontal black line is the estimate from the corresponding season (spring, summer, autumn, and winter). Red lines are the 95% confidence interval for the seasons. Two standard errors (SE) as error bar. Location 7 - 12

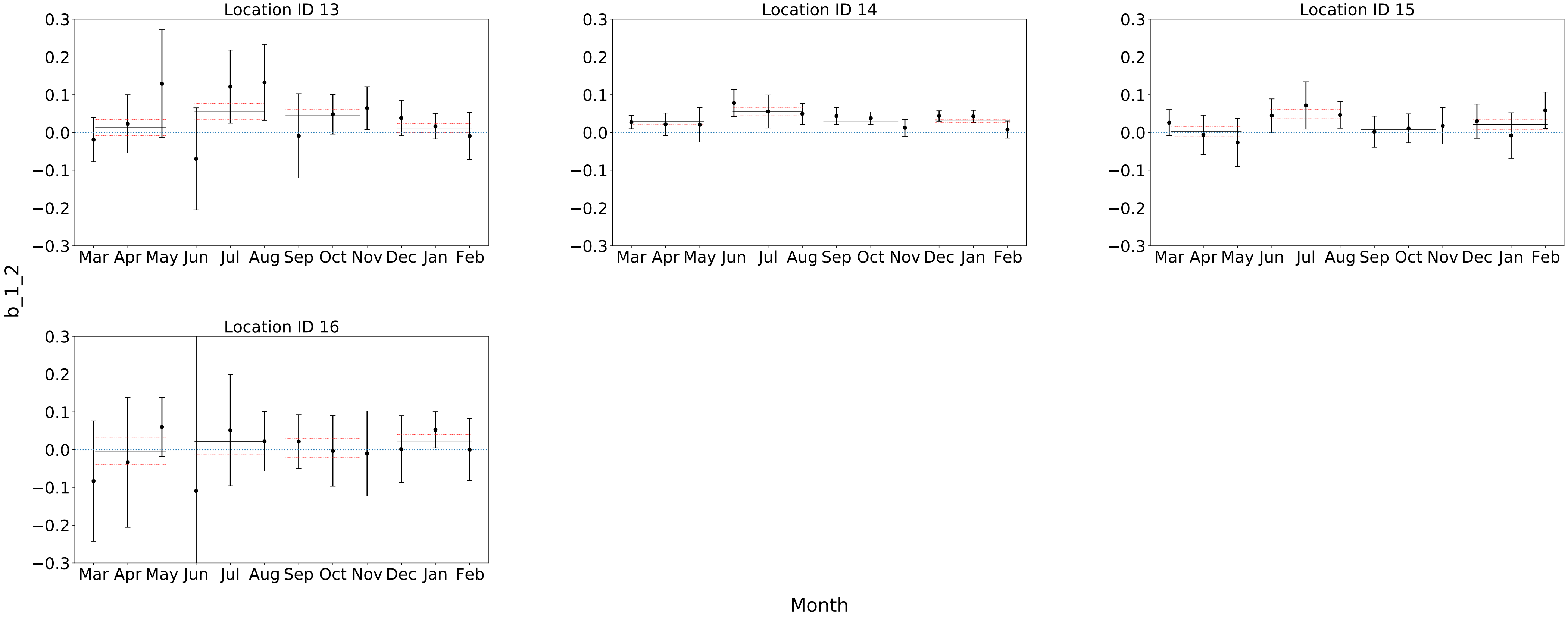

Figure 4.26: The coefficient for each location and month of the year from the logistic regression with daily precipitation as a predictor. A solid horizontal black line is the estimate from the corresponding season (spring, summer, autumn, and winter). Red lines are the 95% confidence interval for the seasons. Two standard errors (SE) as error bar. Location 13 - 16.

Table 4.13: Akaike information criterion (AIC) for the three Logistic Regression prediction models fitted for Vestland County as a region. The smallest AIC value presents the model with "best fit".

| **Model selection with AICc** | | | |
|---|---|---|---|
| | $LR_1$ | $LR_2$ | $LR_3$ |
| Month | AIC | AIC | AIC |
| Jan | 4486 | 4571 | 4444 |
| Feb | 4340 | 4480 | 4323 |
| Mar | 5327 | 5314 | 5296 |
| Apr | 3949 | 3930 | 3932 |
| May | 3104 | 3098 | 3100 |
| Jun | 2568 | 2538 | 2534 |
| Jul | 2235 | 2201 | 2203 |
| Aug | 2552 | 2526 | 2527 |
| Sept | 2925 | 2806 | 2806 |
| Oct | 2735 | 2701 | 2699 |
| Nov | 2873 | 2838 | 2840 |
| Dec | 3400 | 3407 | 3355 |

# Chapter 5

# Discussion

## 5.1 Potential sources of error and limitations in the data

### 5.1.1 Limitations of the rockfall inventory

The national rockfall inventory is a valuable tool for investigating rockfall occurrence, but it has some limitations. The majority of rockfall events in the inventory were observed and recorded due to a rock colliding with a road or railway. Rockfalls occurring further away from infrastructure are rarely observed, resulting in a significant spatial discontinuity or bias in the rockfall inventory. Although some rockfalls occur in road cuts, the focus of this study is on natural slopes. Machine learning algorithms learn by analyzing past rockfall characteristics. Although this is not always the case, the models learn that rockfall does not occur in areas where there have been no observations.

Another source of error is that the accuracy of the timing of the rockfall event varies in the inventory. The inventory includes a column labeled "Accuracy," but it is rarely filled out. Some registrations are direct observations of rockfall events, whereas others are registered hours or days later. The majority of the registered dates do not include the hour and minute of the day. Thus, the common characteristics of all rockfall events are the day, month, and year. Of course, it is possible to filter the data to only include events with hourly accuracy, but this will significantly reduce the data size.

The coordinates recorded in the inventory show where the rock impacted (mostly on roads), but the source areas of the rockfall event is unknown. Typically, the distance between where the rock impacted and the source area is less than one kilometer. Because temperature and precipitation are not spatially independent, the difference in weather conditions between the impact and source areas is expected to be small. Precipitation, however, may vary in intensity very locally. The elevation difference is the most significant factor that can influence temperature and precipitation. This study used two approaches to overcome this limitation: One was mapping source areas in the training area and using these to train the machine learning algorithms. The second method was to correct the lapse rate, in which the highest point in a 500-meter radius around each rockfall impact in Vestland was used in the meteorological analysis as a proxy for the source area elevation.

### 5.1.2 Mapping of source areas

95 rockfall source areas in the training area were mapped in order to use topographic variables as input features in the machine learning models. Slope angle, for example, varies greatly between the location where the rock impacted and where it originated. During fieldwork, it is possible to see the fresh scar from an event in the rock wall, and project reports can indicate where a specific rockfall event originated based on a detailed assessment. However, this approach is time-consuming and would almost certainly result in an insufficient data set. In Lærdalen and Aurlandsdalen, 95 rockfall source areas were thus mapped using knowledge-driven identification. Model performance for geomorphology applications improves significantly with sample sizes ranging from 20 to 100 observations, according to Hjort and Marmion (2008). They recommend a minimum of 100 observations for a medium-scale training area of up to 1 $km2$, with 200 observations providing a robust model. Although the 95 mapped source areas were clearly at the lower scale of sample sizes required for a robust model, the total number of rockfall source area pixels was much higher because the polygons were divided into pixels.

The DEM hillshade and a slope map were the most important data that contributed to mapping the rockfall source areas. The surface model shows historic scars in the terrain as well as fractured rock walls. Aerial photos provided an additional data source that was useful in some areas.. Aerial photographs can reveal the state of vegetation on the slopes as well as features such as fractures and potentially unstable blocks. The primary limitation of aerial photos is their lack of temporal resolution, and it would be ideal to compare a photo taken shortly before and after a rockfall event. Access to higher-resolution aerial images would provide greater certainty in mapping rockfall source areas.

The mapped source areas in this study were not determined using slope a angle threshold, in contrary to Derron (2010). The advantage of not establishing a strict slope angle threshold is that areas with lower slope angles are not ruled out as potential rockfall sources. Natural rockfalls can occur on not-so-steep slopes as well. The machine learning algorithms are expected to perform better as more source areas are mapped, but mapping source areas manually is a time-consuming process. A more precise quantification of the impact of the number of mapped source areas and their spatial distribution is required.

### 5.1.3 Use of meteorological data

The SeNorge2 daily temperature and precipitation data are interpolated between climate stations measuring true values, and the performance is comparable to or better than the pan-European dataset E-OBS (Lussana et al. (2018)). Where the spatial resolution of climate stations is low, the error is larger, but this was not the case in Vestland County. The data was only available at a daily resolution, making it difficult to investigate daily temperature fluctuations or hourly precipitation observations. Temperature and precipitation data from SeNorge2 were extracted from the coordinates of the registered rockfall impact and adjusted for the difference in elevation between that point and the highest point within a 500 m radius of the impact using lapse rate. The fact that the data were not extracted from true rockfall source areas adds to the uncertainty of the analysis. Another consideration is the approach of "pooling" the climate data in the reference database. The reference climate data is an average of data from 16 locations throughout the county; however, averaging data has some disadvantages. Extreme precipitation and temperature events will not be described adequately. Intense rainfall events is an expected triggering weather type for rockfall release probability (Section 2.4.3), but such effects may be difficult to identify.

## 5.2 Potential and limitations of machine Learning methods for rockfall source area classification

### 5.2.1 Machine learning challenges in Geosciences

A disadvantage of machine learning algorithms over classical statistical models is that they can be described as "black boxes." Three of the ML algorithms employed in this thesis are complex models that do not reveal much about the relationships between the input features in the model and rockfall source areas. Ensemble models and neural networks are chosen over simpler models to increase prediction performance (Karpatne et al., 2019). They do not, however, necessarily improve scientific understanding. This limitation should be considered when selecting an ML model.

Another major challenge in machine learning for geosciences is the large variability of characteristics across space and time, making it difficult to generalize models (Karpatne et al., 2019). The processes of interest are commonly low-frequency events with significant societal consequences, resulting in small sample sizes for the class we want to predict. The original plan for this study was to combine the spatial and temporal prediction of rockfall occurrence, but due to the problem's complexity, the decision was made to split the spatial and temporal prediction into two parts. The release of rockfalls is a complex process that extends beyond the Earth's surface into other layers such as the atmosphere in terms of triggering mechanisms. To capture these effects, high-dimensional data with a large number of variables is required (Karpatne et al., 2019).

Input features used in machine learning should be spatially and temporally independent, according to a fundamental assumption in machine learning (Hastie et al., 2009). The majority of phenomena in Geosciences occur in both space and time, resulting in Spatio-temporal auto-correlation between observations (Karpatne et al., 2019). There is a tendency that values that are close are more similar than more distant values are widespread (Roberts et al., 2017). The challenge of spatial dependency in the data is especially relevant for evaluating model performance for ML models used to predict rockfall source areas. The mapped rockfall source area polygons were divided into 10 x 10 m pixels, it is expected that the topographic characteristics of neighboring pixels are highly correlated and that there is a spatial dependent structure in the data violating ML assumptions. The data were randomly split with 70% of the data in the calibration set and 30% for the evaluation set. Both data sets are randomly spread across the training area, which causes dependency between the two data sets. This challenge was previously discussed in Miska and Jan (2005) who used predictive models for geomorphological mapping. Their training and evaluation sets were described as quasi-independent. Furthermore, the models in this study predict the mapped source areas used for training very well (Figure 4.4), indicating that the models are overfitted. The dependency between values results in overfitting the model when predictors allow the model to fit structured patterns (Roberts et al., 2017). Model validation should be performed using data from a different geographic region or spatially distinct subsets of the region (Roberts et al., 2017). This is because when spatially dependent data that are held out for testing are collected from the same area, the independence of evaluation data is compromised (Roberts et al., 2017). Roberts et al. (2017) suggest that "blocking" in the cross-validation could account for spatial and temporal auto-correlation, which should have been implemented.

The data should have been split geographically within the training area rather than randomly across the training area for the calibration and validation of the machine learning algorithms. This would not improve the models, but it would produce more realistic validation results. Marmion et al. (2008), which predicted periglacial landforms in Finland, is an example of a study that uses two spatially independent data sets for calibration and evaluation. The random split-sample approach is currently the most common in mass movement prediction with machine learning algorithms, and it is recommended that "Blocking" in cross-validation be implemented if possible.

### 5.2.2 Selection and performance of models

Three ensemble machine learning algorithms and the Logistic regression algorithm were explored for the objective of predicting rockfall source areas. Once the data processing is complete, the built-in models in Scikit-Learn are simple to implement, allowing for the use of multiple models. The Logistic Regression algorithm is the most basic model for binary classification, and it was chosen to compare the performance of a simple machine learning algorithm to ensemble models.

Metrics from the validation of the models can be used to compare model performance (Table 4.4). Accuracy, defined as the relationship between correctly classified predictions to the total number of predictions, is one of the most common metrics used for evaluation of ML-models. However, it does not indicate how well the models predict the positive class, rockfall source areas, our primary interest. GBRT achieved the highest accuracy score with feature combination $pc8$ in this study. Random Forest, on the other hand, achieves the highest accuracy for feature combination $pc6$. The differences between the ensemble models are minor, and one model cannot be chosen over the other based on this metric. The most considerable difference in accuracy comparing the ensemble models and the Logistic regression model is observed in feature combination $pc7$ and $pc8$ (Table 3.4). The Logistic regression model does not perform well without slope as an input feature. The effect of input features is discussed in Section 5.2.3.

The accuracy scores of all models, except LR *pc*7, are more than acceptable compared to accuracy scores in other studies (Liu et al. (2020), Shirzadi et al. (2012)). Liu et al. (2020) proposed that all three ensemble models are capable of predicting shallow landslides caused by a rainfall event in Kvam. They used the same approach of the random split of data as used in this study, indicating that the accuracy scores obtained in Liu et al. (2020) may are too optimistic because of the spatial dependency discussed above. However, when the accuracy scores are compared, it appears that GBRT, RF, and MLP are equally capable of predicting rockfall source areas and shallow landslides.

Recall, or the sensitivity, is, in general, higher than precision for all four algorithms (Table 4.4). This indicates that a large number of pixels in the training area were incorrectly classified as rockfall source areas. Recall is often higher than precision in models trained on data sets where the positive class is the minority class. Classifying the negative class as positive is more likely than wrongly classifying the positive class as the negative class in these situations. Figure 4.3 and Figure 4.2, show that a large number of the "wrongly" classified pixels in the positive class may be true rockfall source areas in the real world. The AUC-ROC scores are above 0.9 for all models except LR *pc*7, which is very good results. Good AUC-ROC results show that the models are much more likely to correctly predict rockfall source areas than they are likely to incorrectly predict rockfall source areas as areas not prone to rockfalls. This is a desirable result when dealing with dangerous mass movement hazards.

Random Forest, Gradient Boosting Regression Trees, and the Multilayer Perceptron are all complex ensemble models. The models show potential for rockfall source prediction. However, the minor differences in model performance compared to the Logistic regression model suggest that the complexity of ensemble models may not be required for predicting rockfall source areas. Miska and Jan (2005) discovered minor differences between the modeling algorithms they chose for their classification of sorted and non-sorted ground types, demonstrating that minor differences between models are common in the field of Geosciences. The potential of complex, ensemble machine learning algorithms for rockfall source area classification is limited by the uncertainties in data available for this problem, both in terms of quality and quantity. Furthermore, observed or "true" values assist supervised learning models in the learning process. These values are used as ground truth, and there are uncertainties about the quality of these observations, as previously discussed. The small differences between the models show that model selection may not be crucial for this classification problem. Scientists should therefore consider practical aspects when selecting a model. The training time of the three ML algorithms was not systematically registered, but the training time for the MLP classifier was clearly larger than the training time for RF, GBRT, and LR. The same result was shown in Choi et al. (2021) (Figure 5.1).

### 5.2.3 Effect of input features on the model performance

Different methods can be used to obtain the most explanatory input features and the optimal number of features for a machine learning model. Examples are the Integrated Gradient (Park and Kim, 2019), Chi-square statistics (Zhai et al., 2018), the Gini information gain (Liu et al., 2020), LASSO (Lombardo and Mai, 2018), and the built-in Recursive Feature Elimination With Cross-Validation method from `scikit-learn`. These methods were not employed for input

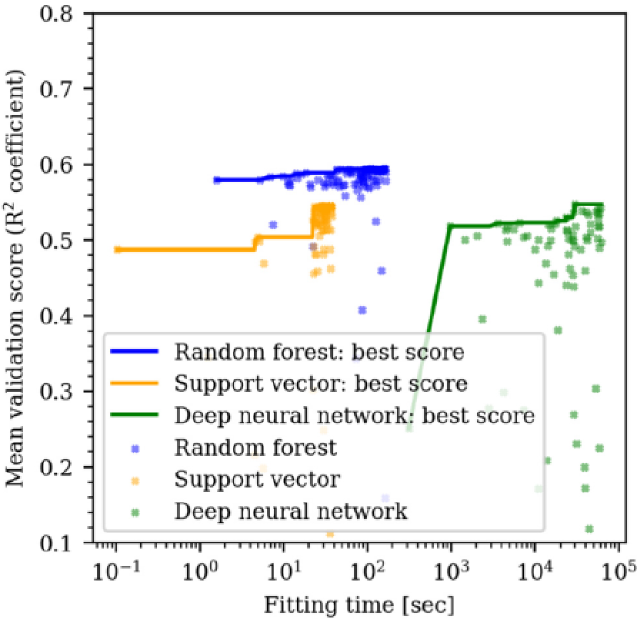

Figure 5.1: Fitting time for different machine learning algorithms by Choi et al. (2021)).

feature selection in this study because a simple sensitivity analysis of input features was of interest.

The Feature Importance's results show that slope angle is the relatively most important feature (Figure 4.1), as expected. Slope angle is a critical factor for the release of all gravity-driven mass movement processes. Böhme et al. (2013) suggests that a quantitative spatial analysis often results in a susceptibility map reproducing a slope-angle map. The Random Forest *pc*8 map (Figure 4.7) were therefore compared to a slope angle-map computed for the same area (Figure 5.2). There is a clear similarity between the two maps, which corresponds to previous knowledge about the strong correlation between rockfall failure and slope angle.

Although slope angle should clearly be included as an input feature, it was left out in *pc*7 to explore if the machine learning algorithms could predict rockfall source areas without it. Despite being the least performing model, the evaluation metrics for *pc*7 are surprisingly good compared to the other feature combinations. This result indicates that one or more of the other features in that combination has good predictive power. The fact that areas far from the road and at high elevations are classified as ”low” probability for rockfall occurrence suggests that elevation and distance to roads are good predictors for the mapped source areas. Natural rockfalls also occur further away from roads, indicating that the models are somewhat over-fitted to the observed rockfall events in the inventory. This result is not surprising because machine learning algorithms are only as good as the data they are fed. It could be interesting to explore how these models would perform without slope, elevation, and distance to roads.

Feature combination *pc*8 with all input features gave the highest evaluation metric scores. However, the *pc*1 models with only slope angle as input feature can also predict rockfall source areas. On the other hand, these models are conservative and less detailed than the other feature combination models. In order to determine the sensitivity of input features, a more extensive sensitivity analysis should be employed. The constant upgrade of GIS and other software gives

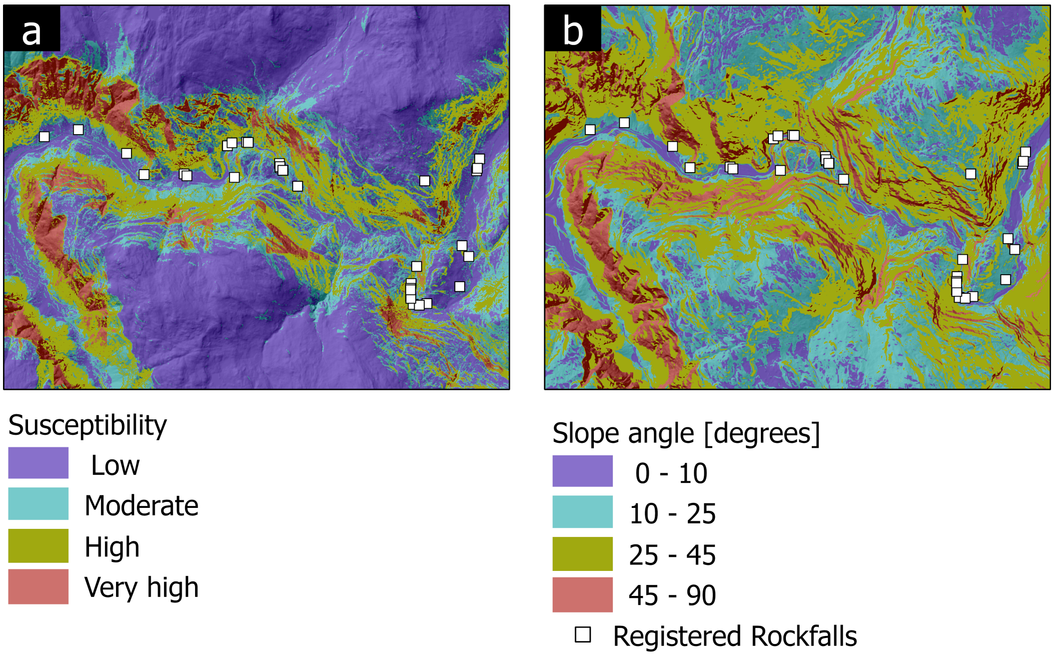

Figure 5.2: (a) The RF *pc*8 susceptibility map. (b) A slope angle map from the same area, calculated in ArcGISPro (2.7.1).

scientists new tools to better calculate surface parameters like slope and curvature. Böhme et al. (2013) found that Quaternary geology, tectonostratigraphic position, and geological lineament density have the strongest spatial correlation with rockfalls in their study area in Vestland County. This study did not include these input features. Another relevant input feature is "bare rock" that Derron (2010) extracted from the "Løsmasser" map from NGU. However, the findings of this study indicate that the addition of new features does not always result in a significant performance improvement. Multiple input features increase data collecting time and model complexity, so it would be beneficial to learn more about the effect of input features on model performance.

For feature combinations *pc*1, *pc*2, *pc*3, and *pc*4, is the performance of the Logistic Regression model very close to that of the ensemble models. Although the Logistic regression models have the lowest evaluation metric scores, the difference is insignificant for some of the eight feature combinations. Multiple input features increase data collecting time and model complexity, so it would be beneficial to learn more about the effect of input features on model performance. This indicates a linear relationship between rockfall source areas, slope, and aspect. The most considerable difference in accuracy comparing the ensemble models and the logistic regression model is feature combination *pc*7 and *pc*8 (Table 3.4). The logistic regression model does not perform well without slope as an input feature. Bedrock does not improve the logistic regression model when included as a feature. The accuracy scores of the ensemble models are decreasing when distance to roads are excluded in *pc*6, while there is no difference between *pc*5 and *pc*6 in the Logistic regression model. The results from the Linear Regression model and the Mulilayer Perceptron neural network should be similar if the relationship between dependent and independent variables is linear (Bagheri et al., 2018).

### 5.2.4 Comparison with susceptibility map in Böhme et al. 2013

The study by Böhme et al. (2013), which is cited throughout this thesis (Section 2.1.2), compared the Weigh-of-Evidence method to the Logistic Regression method for modeling a rockfall susceptibility map. They concluded that using Logistic regression with the same controlling parameters produces a susceptibility map that is very similar to the Weight-of-Evidence method but with larger posterior probabilities. They successfully predicted 70% of registered rockfalls with their susceptibility map in Sogn and Fjordane (Figure 5.3). The final ML models in this study were therefore tested on the same area that Böhme et al. (2013) used for comparison (Figure 4.14). Random Forest *pc4* models predict areas near registered rockfall impacts as either susceptibility class "High" or "Very high", and the map is more conservative than the one proposed in Böhme et al. (2013). A significant difference between this study and Böhme et al. (2013), other than the choice of algorithms, is that Böhme et al. (2013) used the rockfall impact registrations rather than source areas for extracting input features. As a result of this, they did not use slope angle as an input. It is interesting that these two approaches yields such similar maps.

S

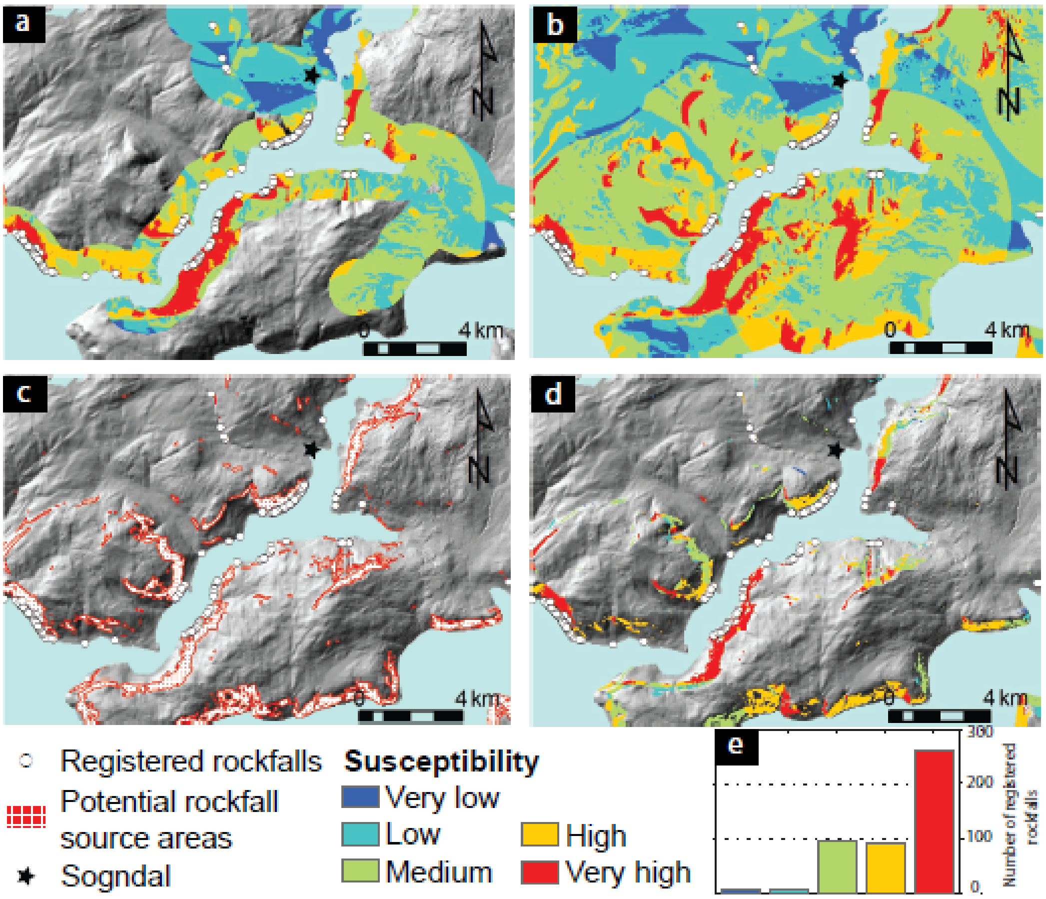

Figure 5.3: Figure from Böhme et al. (2013)). a) Susceptibility within a road buffer of 1 km, which was used for the training area. b) Susceptibility map for the entire land area based on the model set up in a). c) Rockfall susceptibility map based on Derron (2010). d) combined rockfall susceptibility map with the source zones from Derron (2010) updated with probabilistically assessed susceptibilities. e) Distribution of susceptibility for the registered rockfalls within the displayed area.

### 5.2.5 Transferability of ML-models

The regional performance of the machine learning models in this study can, in some ways, describe the models' transferability. The performance, however, can only be described qualitatively by comparing predicted rockfall source areas to registered rockfall events and national potential rockfall source areas (Derron, 2010). It was decided to investigate all four algorithms using feature combination *pc*8 because more complex models with more input features are expected to be less transferable than simple models (Hjort et al., 2014). The predicted source areas from the Logistic Regression model *pc*84 (Figure 4.9) are very similar to those predicted by textcitederron method 2010, indicating that the predictions with Logistic Regression are primarily based on the input feature slope angle, even though all other input features are included. The MLP *pc*8 model classifies most areas as low susceptibility, also areas that are potential rockfall source areas according to Derron (2010). This result contradicts results from the training area (A5), indicating that MLP performs poorly in areas far from the training area. Random forest *pc*8 classifies multiple areas as "high" susceptibility„ but only a few as "very high" susceptibility (Figure 4.11), indicating that the model is less confident in its prediction in this area than in the training area (Figure 4.7). The Derron (2010) map is more conservative than the GBRT map (Figure 4.12, but GBRT predicts many areas as the "Very high" class, indicating that the model is confident in its predictions and can be considered transferable.

Hjort et al. (2014) conducted a thorough study comparing multiple machine learning models for prediction of solifluction occurrence in Finland and discovered that only slightly more than half of the models were transferable. A similar conclusion can be made from the quantitative analysis of regional performance in this study; Logistic Regression and Gradient Boosted Regression Trees are suggested as transferable at a regional level, while Multilayer Perceptron and Random forest are not. While the regional performance of two of the machine learning models in this study is acceptable, more research is needed to determine whether the models could be transferred to, say, Northern Norway or another country.

## 5.3 Regional and local meteorological analysis

### 5.3.1 Difference between "Rockfall climate" and "Reference climate" data

The seasonal effect (Figure 3.1) that is seen in the temporal frequency distribution of rockfall events is expected to be related to the different weather conditions of the seasons (Sandersen et al., 1997). The histograms showing the empirical distributions of reference climate and rockfall climate indicated that there is indeed a difference in temperature and precipitation when rockfall events occur compared to the defined normal situation in Vestland County. The Kruskal-Wallis H-test also concludes with this for various variations of temperature and precipitation parameters, except daily precipitation (Figure 4.9).

Two temperature peaks were observed from the daily mean and mean temperature 14 days histograms for both the reference climate and rockfall climate. The first around zero C and the second around 10-12 C . The interesting part is that the peak around zero C is higher for rockfall climate compared to the reference climate, and the opposite for the peak around 10-12 C . This indicates that rockfalls in Vestland most frequently occur when temperatures are around 0 C , temperatures around 0 C are related to freeze-thaw activity. This finding is consistent with the literature from other regions (Matsuoka and Sakai, 1999, Frayssines and Hantz, 2006, D'Amato et al., 2016,Matsuoka, 2019).

As an example, only 1% of 14 days periods through the year has accumulated precipitation of 284.5 mm for the reference climate, compared to 10% of rockfall events occurring with 14 days accumulated precipitation of 292.29 mm (Table 4.7).

Numbers in Table 4.7 show that 10% of rockfall events have 14 days accumulated precipitation that matches the 14 days accumulated precipitation for the highest 1% of days in the reference climate. The results from the Kruskal-Wallis test suggest that the difference between rockfall climate and the reference climate for accumulated precipitation 3 days and 14 days are more significant than for mean precipitation 14 days. These findings suggest that precipitation does have an effect on rockfall occurrence probability in Vestland County, despite the fact that the results are not entirely clear. Vestland County is dominated by long-term precipitation rather than intense rainfall episodes (Frauenfelder et al., 2013), a study of Vestland might not be appropriate to explore the effects of intense rainfall episodes as a triggering mechanism.

### 5.3.2 Weather events as triggering mechanism

The suggested triggering weather types are an attempt to quantify meteorological triggering effects in Vestland County (Table 4.10). The rockfalls events occurring during freeze-thaw periods were identified from the database, and freeze-thaw is suggested as a potential triggering weather type. Rockfall events occurring in freeze-thaw periods account for 57.7% of all registered rockfall events in Vestland, and most of these events (39% of the events in a freeze-thaw period) occur on a day with positive temperatures that are defined as thawing days (Table 4.10). This is a interesting result that coincides with findings in Matsuoka and Sakai (1999), D'Amato et al. (2016) and Matsuoka (2019).

Rockfalls occurring during warming periods rather than during cooling periods indicate that the triggering mechanism is related to the fact that the cohesion of the ice-rock interface is large enough to compensate for an unstable situation caused by crack propagation because of the expansion of ice, until the ice melts (D'Amato et al., 2016). Thawing is related to the production of water, which means that the effects of thawing may be similar to the effects of precipitation and snow-melt. The number of events with at least 284.5 mm accumulated precipitation the 14 last days before a rockfall event is highest in terms of category percentage (13.69%) for the Freeze-thaw category (Table 4.10). It is not known whether this precipitation falls as snow or rainfall, but since we do know that these periods have days with positive mean temperatures, that some of the precipitation falling as rain is likely. It is also likely that some of the precipitation falling as snow will melt during a freeze-thaw period so that access to water is present during the periods when rockfall occurs in freeze-thaw periods in Vestland County. The lowest percentage of rockfall events occur in freezing periods with daily temperatures below 0 C, with most of the occurrences happening on days with negative cooling (Table 4.10). This suggests that freezing periods are the most stable weather condition, but that periods with negative cooling, when sub-zero temperatures are decreasing, might initiate some processes that can trigger rockfall events. These observations can be connected to the "frost-cracking" theory in Hales and Roering (2007). The optimal temperature range for frost cracking is between -3 and -10 C. Temperatures just below zero can thus cause stable conditions until the temperature decreases and reach the frost cracking window. Frost-cracking is dependent on the access of water, which may be the limitation regarding frost cracking as a triggering mechanism in the freezing periods with small amounts of precipitation. 37.4 % of all registered rockfall events occurred in a period of no freezing (Table 4.10), these events should therefore either be related to precipitation as a meteorological triggering mechanism, extremely high temperatures, or an unknown trigger not related to temperature or precipitation.

Matsuoka (2019) showed that rockfalls in frost-free periods mostly followed a certain amount of rainfall, while only 7.53 % of the rockfall events in the Vestland inventory occurred after 14 days with more than 284.5 mm precipitation. However, the low number of rockfall events directly related to heavy precipitation in the Vestland database cannot rule out that heavy precipitation increases the probability of rockfall occurrence in Vestland. It could simply indicate that heavy rainfall events in Vestland are uncommon. The findings in this study indicate that other, non-precipitation-related triggering mechanisms are more critical for rockfall occurrence in Vestland County for the current climate, which will probably change during the next century. Sandersen et al. (1997) states that precipitation is one of the most significant triggering factors for rockfalls after freeze-thaw cycles. The conclusion is based on the annual distribution of rockfall events in the studied database, with a peak of rockfall activity in spring, late autumn, and the beginning of winter. This is annual frequency is observed in the national rockfall inventory as well (3.1). However, this study shows that it is difficult to see confirm this finding from a statistical analysis of daily precipitation data.

Although there have been 15 rockfalls in Vestland on days with a mean daily temperature of 20 °C, the uncertainty surrounding high temperatures as a triggering effect in Vestland led to the decision to exclude extremely warm temperatures as a potential triggering category. However, rockfalls caused by extremely high temperatures in Vestland, while not statistically significant, are an intriguing phenomenon that should be investigated further in the future. The results show that at least 33.73 % of all rockfall occurrences in Vestland are not related to meteorological triggering mechanisms. A suggestion to relate 66.27 % of rockfall events from the Vestland inventory to meteorological triggering mechanisms is a good result that should be tested and validated through more studies.

### 5.3.3 Prediction models for temporal occurrence

Predictions models have been fit for other types of landslides multiple times. One of the objectives was to explore if it is possible to use temperature and precipitation as predictors for rockfall occurrence in logistic regression models. The earlier results showed a significant difference between the rockfall and reference climate in Vestland County, but local effects were not explored. The local effects will be discussed in terms of the performance of prediction models and the significance of temperature and precipitation as predictors for the 16 locations in Vestland County.

*Daily temperature* is considered a significant predictor for 9 to 11 locations from January to April. 5-9 locations from May to August and 3 -9 locations from September to December (Figure 4.11,B1,B2). Figure B2 showed that daily temperature was finding shows that daily temperature are considered a significant predictor for only 3 out of 16 locations on October, while 9 out of 16 locations in December. There is a seasonal pattern where the slope is lower for spring, summer, and autumn than for winter. This suggests that temperature has more predictive power during the winter months.

These findings suggest that daily mean temperatures are more likely to significantly predict rockfall occurrence in spring and winter than in summer and autumn. Spring and winter are prone to periods with freeze-thaw, and these results confirm that temperature as a meteorological triggering variable is most likely related to freeze-thaw weather events in Vestland County, rather than, for example, extremely high temperatures, which were discussed in Allen and Huggel (2013)). Slopes (Figure 4.20,4.21,4.22).) varies between locations and between months, which means that change in temperature in, for example, January has a different effect than the change in temperature in July. This effect also varies by location. These results show that it would be challenging to fit a prediction model based on the temperature at a regional level in Vestland County, even if said models were fit for each month of the year.

*Daily precipitation* is considered a significant predictor for a high number of locations in December, January, and February. The most surprising result is that daily precipitation is only considered a significant predictor for 3 of 16 locations in October and 6 of 16 locations in November because rockfalls and other landslides during these months are often linked to heavy rainfall in Norway (Kristensen et al., 2021). It is more difficult to observe a seasonal pattern in the slopes of the prediction models with daily precipitation as a predictor than for the model with daily mean temperature as a predictor (Figure **??**, Figure **??**, Figure 4.23). The slopes are mostly positive, implying that the log-likelihood of rockfall occurrence increases with increasing precipitation, but the error bars are large for some locations.

Precipitation is clearly a triggering mechanism for some rockfall events, and it should be included in prediction models. However, daily precipitation measurements may not be the best format to include as a predictor. In 2003, Bakkehøi (2003) studied the triggering mechanisms of a debris flow in Sunndal, Møre og Romsdal. Local sources reported cloudbursts and thunder, but the meteorological station in the area recorded only 0.1 mm of daily precipitation, implying that the heavy rainfall episodes were very local. The Norwegian Meteorological Institute later provided radar images showing that 50 mm of precipitation fell in approximately one hour that evening, clearly triggering the debris flow (Bakkehøi, 2003). It is reasonable to believe that hourly precipitation is a more significant trigger than daily precipitation for rockfall occurrence as well because the release of rockfalls due to precipitation is related to pore water pressure and pressure in joints and fractures (Matsuoka, 2019).

Fitting a model with temperature and precipitation improved most of the logistic regression models fitted for each month of the year, but the differences between log-likelihoods are small. The finding that the $Lr_2$ model for July, with daily precipitation as the predictor, is the best fitted model for Vestland as a Country appears to be based on chance. The results show that temperature and precipitation should be included in prediction models for the temporal occurrence of rockfall events, but it is not yet possible to conclude with what form they should be included or if logistic regression models are the best-suited model. The results also show that models should be fitted for smaller locations and each season or month of the year.

## 5.4 Application for spatial and temporal prediction

The susceptibility maps that show potential rockfall source areas are based on the input features slope angle, elevation, aspect, profile and plan curvature, TRI, distance to roads, flow accumulation, flow direction, and bedrock. All of these features are included in the GBRT *pc*8 model that yielded the most promising results. However, other factors, such as block size and fracture orientation, are not considered. The susceptibility map should be used as the first step in assessing the risk of rockfall hazards (L. K. Dorren, 2003, Volkwein et al., 2011). It provides a broad overview of areas that could be potential rockfall source areas. They can be used to prioritize areas for further hazard mapping, such as identifying unstable blocks, modeling run-out lengths, estimating the magnitude of potential events, estimating return periods, and planning mitigation measures (Volkwein et al., 2011). Prioritization should thus be based on susceptibility classes, but it is suggested that consequences and weather type be included in the first step of prioritizing areas in Vestland County for a detailed assessment(Figure 5.4). The weather type freeze is considered the lowest risk for rockfall release, while the weather type freeze-thaw is considered the highest risk for rockfall release in Vestland.

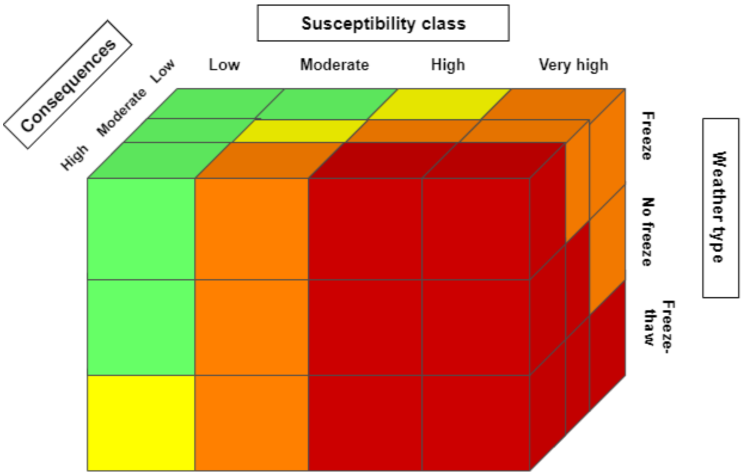

Figure 5.4: A diagram illustrating a preliminary proposal for a potential 3D risk matrix for Vestland County. Susceptibility classes, consequences, and three weather types are included. Green denotes low risk. Yellow denotes a moderate risk, orange a high risk, and red a very high risk.

# Chapter 6

# Conclusions and Future work

## 6.1 Conclusions

Three ensemble machine learning algorithms and the more simple Logistic regression algorithm were evaluated for rockfall source area prediction across Vestland County. All machine learning models are capable of predicting rockfall source areas, but only half of the models are considered transferable within Vestland. The combination of input features influences model performance and the final susceptibility maps derived from predicted probabilities. When more input features are included, and the relatively most important feature slope angle is excluded, the ensemble models outperform the Logistic regression model, demonstrating that the ensemble models can find patterns in data that the Logistic regression model cannot. However, these results show that the Logistic regression model should be chosen over the complex ensemble models when using input features slope angle, elevation, aspect, plan curvature, profile curvature, TRI, and distance to roads. The random selection of pixels for the calibration and validation sets was demonstrated to be disadvantageous. When dealing with spatially dependent data in machine learning, cross-validation with "blocking" is suggested as a more robust validation strategy.

The "normal" climate in Vestland was compared to the climate when rockfalls occur. It was discovered that rockfalls occur more frequently in wetter weather than in dry weather, and results indicate that temperatures around zero are the most significant triggering weather condition for rockfalls in Vestland County. Logistic regression prediction models using temperature and precipitation as predictors show no to little effect on rockfall probability, but revealed a variation in the effect of temperature and precipitation with both location and month, implying that prediction models should be local rather than regional, and fitted for each month of the year. The data show a seasonal effect on rockfall release probability related to temperature and precipitation; while these variables may not be able to be used to obtain day-by-day predictions, they should be included in prediction models.

This project demonstrates the potential of using machine learning algorithms to predict rockfall sources while also highlighting the challenges of spatially and temporally structured data that violates machine learning assumptions. It shows that temperature and precipitation should be included in temporal prediction models for rockfall occurrence, but more research is needed to determine how and which prediction models to use.

## 6.2 Future Work

### 6.2.1 Using back-analysis of run-out lengths to validate predicted rockfall source areas

Evaluating predicted rockfall source areas outside the training area is a challenge in the spatial prediction of rockfall source areas proposed in this study. Uncertainty about the validation metrics is also challenging. As a result, the predicted source areas should be investigated further.

The next logical step would be to validate the susceptibility maps derived from prediction probabilities and then evaluate the trained models for other regions in Norway or other countries if the validation results are promising. Böhme et al. (2013) validated their map by counting the number of recorded rockfall events in each susceptibility class. As a result, the highest susceptibility class should have the most registered rockfall events. This method cannot be directly applied to this study because their map displays areas impacted by the rockfall as susceptibility classes rather than delimited source areas. An intriguing idea for a future approach that emerged during this project is to evaluate the rockfall source areas using back-analysis of the registered rockfall areas' run-out lengths.

Modeling of run-out lengths can be conducted by using dynamic models, such as RAMMS rockfall (Christen et al., 2012) or Rockyfor3D (L. Dorren and Berger, 2010), or empirical models such as the alpha-beta model (Lied and Bakkehøi, 1980, Derron, 2010). The level of confidence in the predicted rockfall areas can be increased if the run-out lengths of rock fragments originating from the predicted rockfall source areas are realistic compared to the registered rockfall impacts.

### 6.2.2 Hierarchical Bayesian Models for temporal prediction of rockfall occurrence

Pooling (combining) data from multiple sources into one large dataset is a common approach for statistical analysis in geosciences. In Vestland, this method was used to compare the distributions of "normal climate" and "rockfall climate" This information can be useful. However, a closer examination of the data often reveals that the data can be divided into smaller subgroups based on location, measurement methods, and material types. (Bozorgzadeh et al., 2019,Bozorgzadeh and Bathurst, 2020).

The "poor" results obtained from this study's predictive logistic regression models formed an idea that future research should adopt a hierarchical Bayesian model for rockfall occurrence prediction. Let us say we want to fit a model that estimates the mean temperature for days with rockfall events for each of the 16 locations in this study. A model can either estimate the mean across all values and provide the overall temperature pattern but ignore variations across locations. It can also be fitted to each location, capturing the variability but not the overall pattern. Bayesian Hierarchical models are the statistical "middle-ground" between these two approaches. They are written in multiple levels that can deal with the shortcoming described above (Bozorgzadeh et al., 2019,Bozorgzadeh and Bathurst, 2020).

Statistical parameters of different groups are assumed to be similar but not identical. They can describe the overall pattern in the data as well as differences between different measurement sources, such as different locations or months The parameters (for example mean effect of temperature) are allowed to vary by group (for example location) and thus capturing the between-group variations. Simultaneously, they are linked together by another statistical model that allows capturing the overall pattern. Hierarchical models are useful because they quantify uncertainty in multiple levels, borrow information from different subgroups, and prevent over/under fitting to data ((Gelman et al., 2013, Bozorgzadeh et al., 2019, Bozorgzadeh and Bathurst, 2020).

Yang et al. (2019) used hierarchical Bayesian models for spatial susceptibility mapping of landslides. The models successfully fused regional trends and local spatial heterogeneity of control factors, demonstrating the potential of hierarchical models in the field of natural hazards.

# Appendix A

# Machine learning figures

## A.1 Range of input features

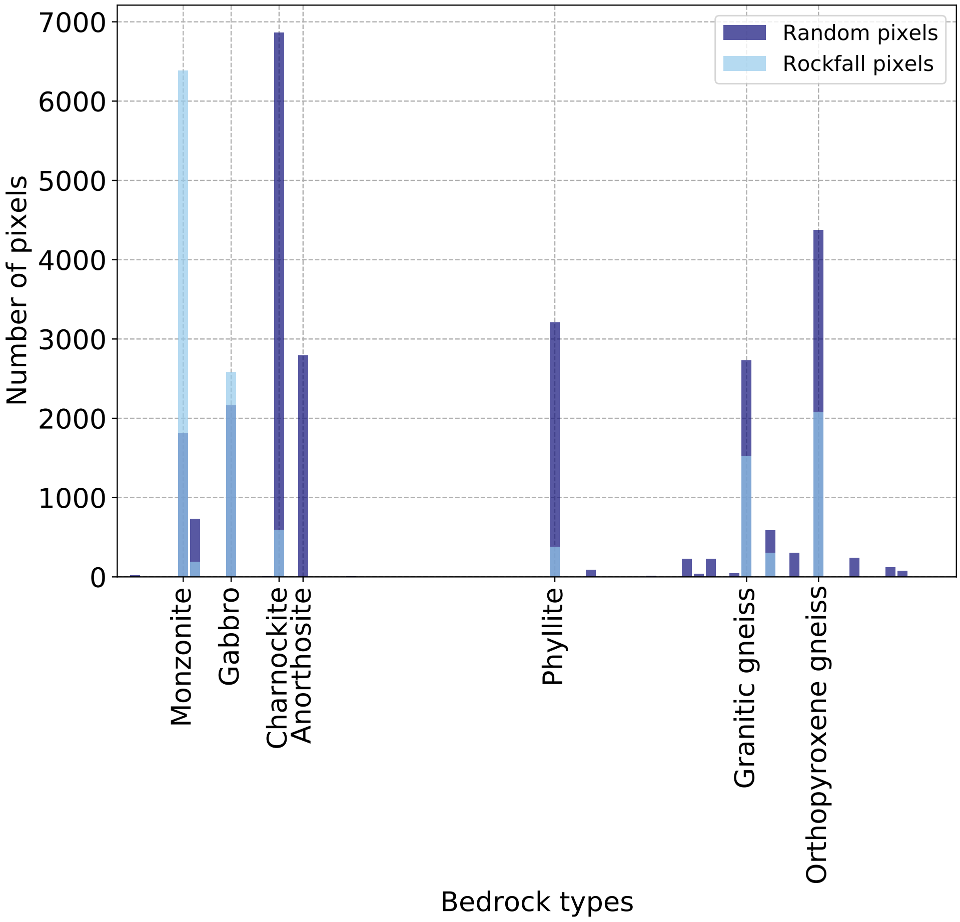

Figure A1: Distribution of bedrock types for random and rockfall pixels.

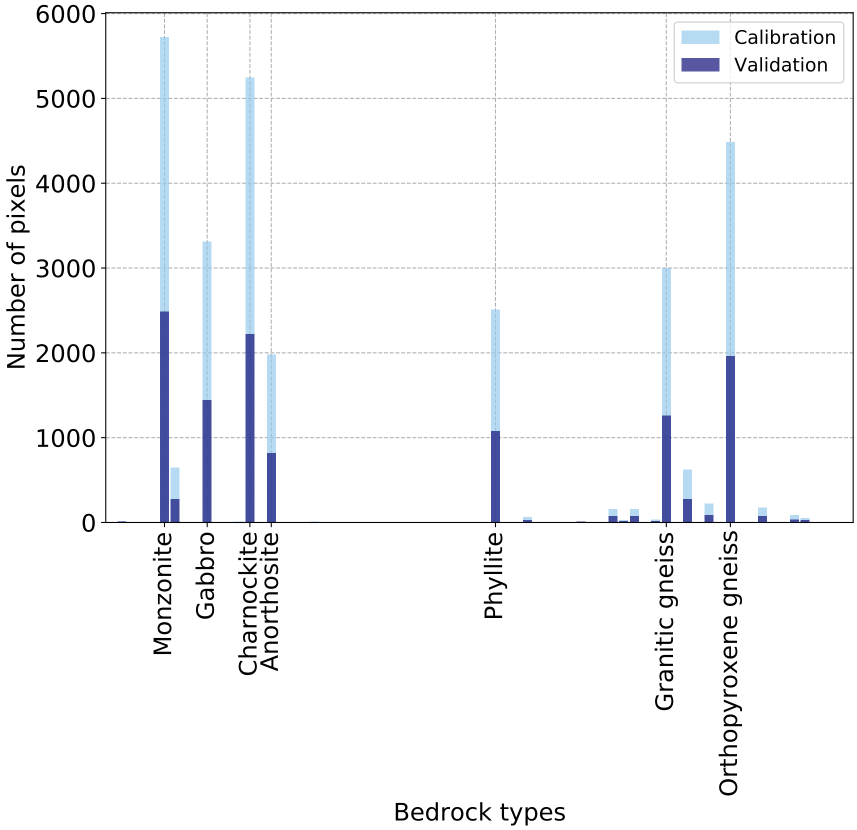

Figure A2: Distribution of bedrock types for the calibration and validation sets.

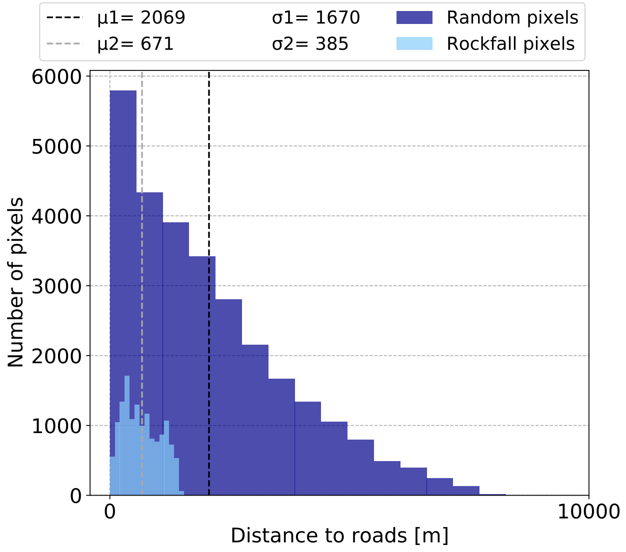

(a)

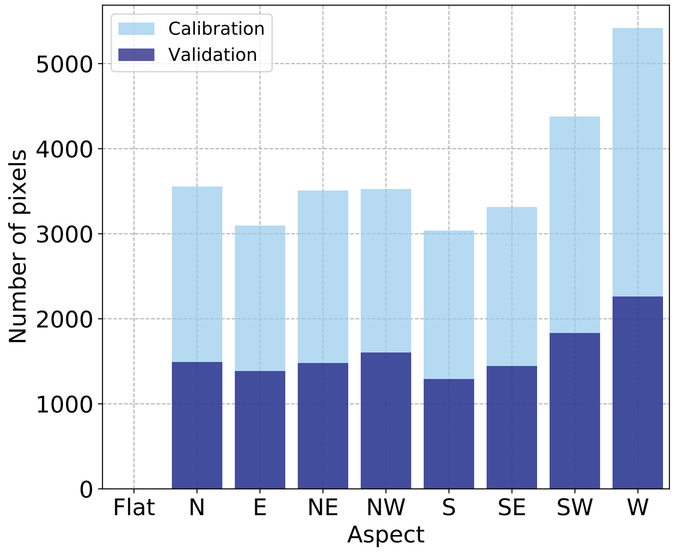

(b)

Figure A3: Histograms showing (a) elevation and (b) slope angles for random and rockfall pixels. For rockfall pixels, elevation ranges from 0 to 1400 m.a.s.l., and for random pixels, elevation ranges from 0 to 1800 m.a.s.l. Slope angle ranges from 30 to 90 for rockfall pixels and 0 to 70 for random pixels. The legend displays the mean ($\mu_1$ for random pixels and $\mu_2$ for rockfall pixels) and standard deviation ($\sigma_1$ for random and $\sigma_2$ for rockfall). Bins = 15.

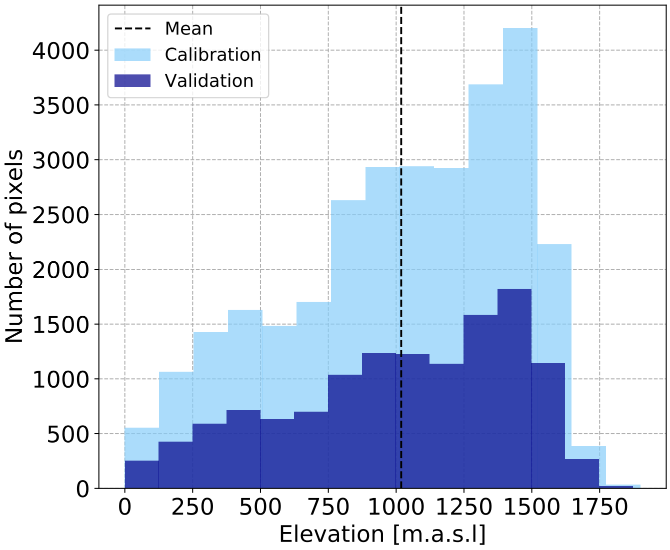

(a)

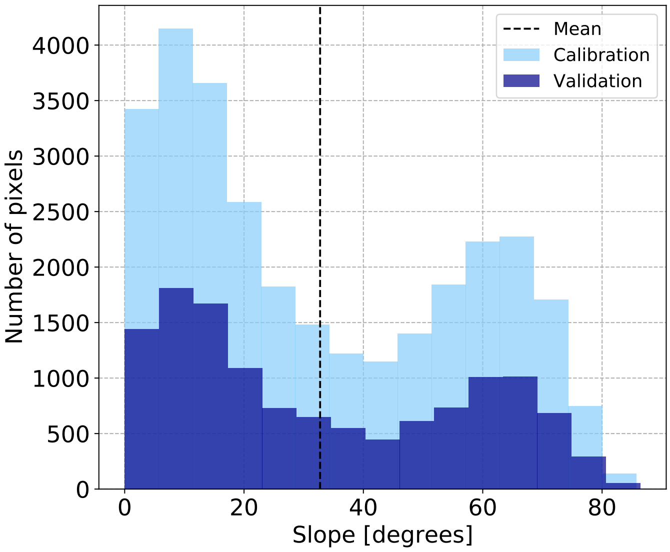

(b)

Figure A4: Histograms showing (a) elevation and (b) slope angles for random and rockfall pixels. For rockfall pixels, elevation ranges from 0 to 1400 m.a.s.l., and for random pixels, elevation ranges from 0 to 1800 m.a.s.l. Slope angle ranges from 30 to 90 for rockfall pixels and 0 to 70 for random pixels. The legend displays the mean ($\mu_1$ for random pixels and $\mu_2$ for rockfall pixels) and standard deviation ($\sigma_1$ for random and $\sigma_2$ for rockfall). Bins = 15.

## A.2 MLP $pc8$ susceptibility map

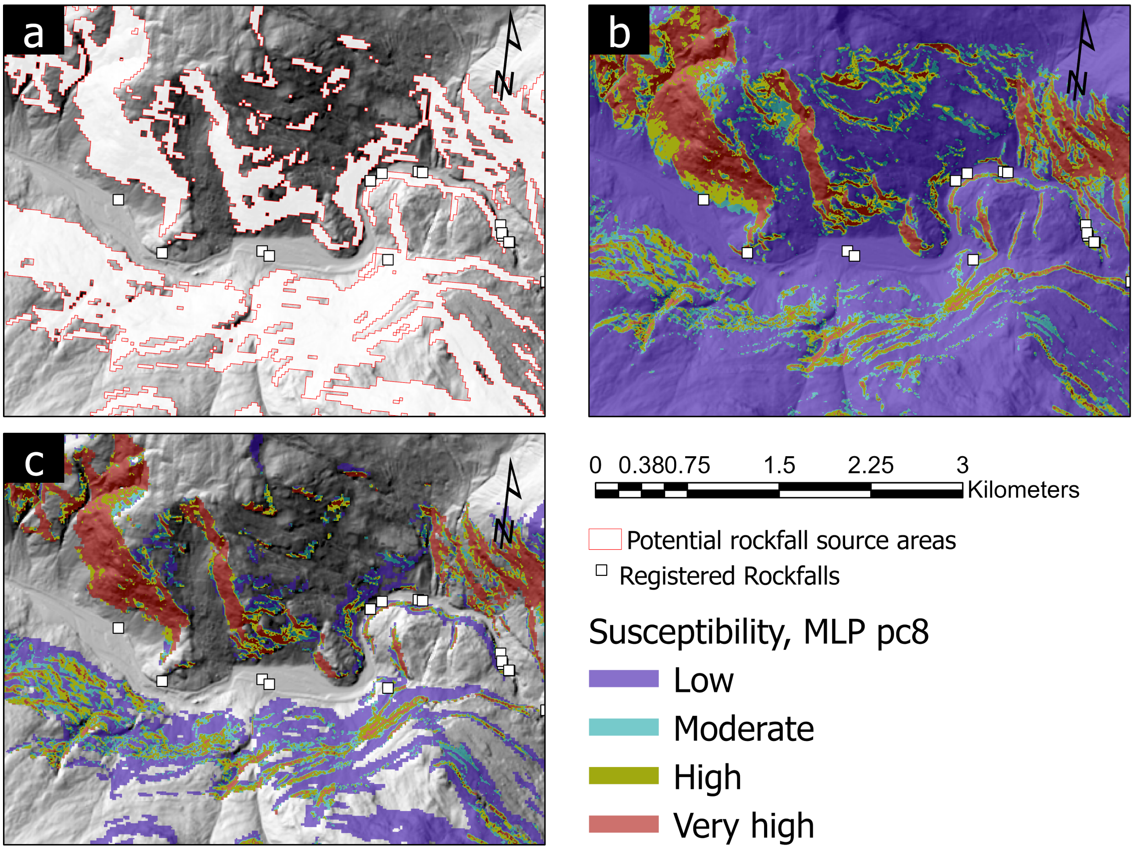

Figure A5: Map showing low, moderate, high and very high rockfall source area susceptibility modelled with the MLP $pc8$ model in a selected part of the training area (Figure 4.4). Classes are defined in Table 4.5. Resolution 10x10m. (a) Potential rockfall source areas from the national susceptibility map (Derron, 2010). (b) Modelled rockfall susceptibility for the entire selected area. (c) Modelled rockfall susceptibility clipped to the extent of the national potential rockfall source areas from Derron (2010).

## A.3 ROC-curves

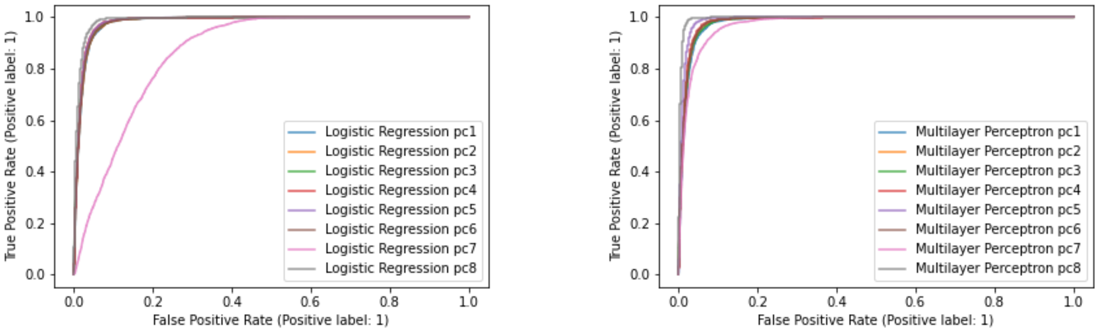

(a) (b)

Figure A6: a) ROC curve of the Logistic Regression models. (b) ROC curve of the Multilayer Perceptron Models.

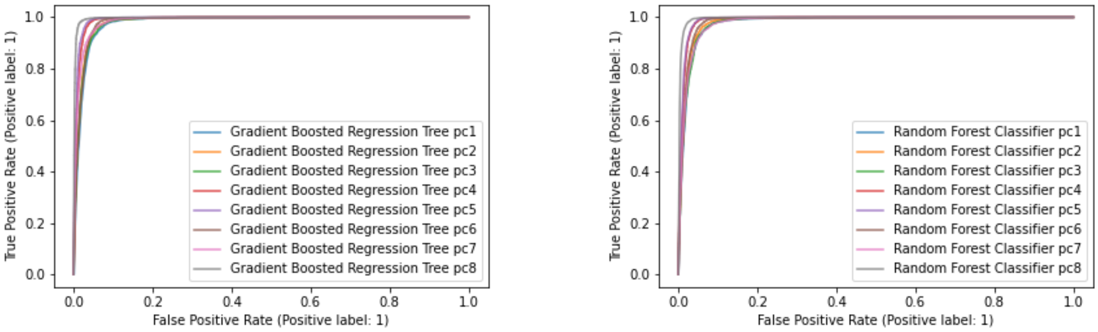

(a) (b)

Figure A7: a) ROC curve of the Gradient Boosted Regression Tree models. (b) ROC curve of the Random Forest models.

# Appendix B

# Logistic regression results

## B.1 Tables with logistic regression results for $Lr_1$ and $Lr_2$

Table B1: $Lr_1$ model results with daily mean temperature as predictor for May to August.

| | Month | | | | | | | | | | | |
|---|---|---|---|---|---|---|---|---|---|---|---|---|
| **Location ID** | May | | | | | | June | | | | | |
| | **Intercept estimate** | **SE** | **p < 0.05** | **Slope estimate** | **SE** | **p < 0.05** | **Intercept estimate** | **SE** | **p < 0.05** | **Slope estimate** | **SE** | **p < 0.05** |
| **1** | -2.405 | 0.612 | yes | -0.070 | 0.069 | no | 0.071 | 0.904 | no | -0.244 | 0.085 | yes |
| **2** | -3.224 | 0.319 | yes | 0.129 | 0.044 | yes | -4.973 | 0.720 | yes | 0.231 | 0.072 | yes |
| **3** | -3.136 | 0.503 | yes | 0.022 | 0.055 | no | -2.116 | 0.798 | yes | -0.075 | 0.075 | no |
| **4** | -4.533 | 0.569 | yes | 0.181 | 0.058 | yes | -1.941 | 0.647 | yes | -0.149 | 0.080 | no |
| **5** | -1.667 | 0.286 | yes | -0.163 | 0.054 | yes | 0.744 | 0.546 | no | -0.424 | 0.076 | yes |
| **6** | -3.255 | 0.356 | yes | 0.172 | 0.040 | yes | -4.374 | 0.690 | yes | 0.185 | 0.058 | yes |
| **7** | -2.924 | 0.453 | yes | 0.028 | 0.052 | no | -1.169 | 0.699 | no | -0.152 | 0.069 | yes |
| **8** | -2.865 | 0.462 | yes | -0.051 | 0.069 | no | -3.787 | 1.137 | yes | 0.019 | 0.106 | no |
| **9** | 1.519 | 0.515 | yes | -0.639 | 0.099 | yes | 2.400 | 1.165 | yes | -0.577 | 0.132 | yes |
| **10** | -3.331 | 0.510 | yes | 0.022 | 0.060 | no | -2.510 | 0.866 | yes | -0.084 | 0.086 | no |
| **11** | -2.454 | 0.680 | yes | -0.073 | 0.074 | no | -0.533 | 1.198 | no | -0.241 | 0.109 | yes |
| **12** | -1.931 | 0.526 | yes | -0.130 | 0.067 | no | -0.218 | 0.810 | no | -0.244 | 0.077 | yes |
| **13** | -1.801 | 0.846 | yes | 0.019 | 0.096 | no | -3.116 | 1.353 | yes | 0.110 | 0.108 | no |
| **14** | -2.666 | 0.294 | yes | 0.091 | 0.038 | yes | -3.396 | 0.580 | yes | 0.098 | 0.056 | no |
| **15** | -2.945 | 0.264 | yes | 0.184 | 0.043 | yes | -3.869 | 0.530 | yes | 0.147 | 0.064 | yes |
| **16** | -5.452 | 1.306 | yes | 0.107 | 0.115 | no | -9.658 | 3.302 | yes | 0.327 | 0.218 | no |
| | July | | | | | | August | | | | | |
| **1** | 2.188 | 1.794 | no | -0.428 | 0.147 | yes | -2.683 | 1.395 | no | -0.015 | 0.098 | no |
| **2** | -6.381 | 1.358 | yes | 0.199 | 0.098 | yes | -4.687 | 0.769 | yes | 0.185 | 0.065 | yes |
| **3** | -2.941 | 0.853 | yes | 0.022 | 0.061 | no | -2.542 | 0.908 | yes | 0.010 | 0.069 | no |
| **4** | -3.454 | 0.780 | yes | 0.043 | 0.060 | no | -6.011 | 1.136 | yes | 0.234 | 0.084 | yes |
| **5** | -0.582 | 0.849 | no | -0.197 | 0.076 | yes | 0.529 | 0.798 | no | -0.295 | 0.080 | yes |
| **6** | -4.266 | 0.932 | yes | 0.110 | 0.065 | no | -2.583 | 0.896 | yes | -0.002 | 0.076 | no |
| **7** | -3.234 | 0.953 | yes | 0.026 | 0.067 | no | -0.172 | 1.120 | no | -0.219 | 0.096 | yes |
| **8** | -2.067 | 1.631 | no | -0.160 | 0.137 | no | -4.207 | 1.083 | yes | 0.110 | 0.086 | no |
| **9** | -3.949 | 2.754 | no | -0.046 | 0.198 | no | -4.034 | 1.546 | yes | 0.062 | 0.107 | no |
| **10** | -3.365 | 1.158 | yes | -0.009 | 0.087 | no | -5.720 | 1.381 | yes | 0.182 | 0.100 | no |
| **11** | 0.660 | 1.393 | no | -0.257 | 0.104 | yes | -0.563 | 1.511 | no | -0.176 | 0.111 | no |
| **12** | -0.664 | 1.106 | no | -0.169 | 0.083 | yes | 2.096 | 1.287 | no | -0.387 | 0.108 | yes |
| **13** | -3.060 | 2.123 | no | 0.115 | 0.154 | no | -0.225 | 2.212 | no | -0.131 | 0.164 | no |
| **14** | -2.777 | 0.571 | yes | 0.053 | 0.045 | no | -3.559 | 0.788 | yes | 0.095 | 0.067 | no |
| **15** | -5.007 | 0.982 | yes | 0.142 | 0.085 | no | -4.288 | 0.821 | yes | 0.124 | 0.082 | no |
| **16** | -4.356 | 3.297 | no | -0.036 | 0.230 | no | -3.541 | 3.209 | no | -0.072 | 0.227 | no |

Table B2: $Lr_1$ model results with daily mean temperature as predictor for September to December

| | **Month** | | | | | | | | | | | |
|---|---|---|---|---|---|---|---|---|---|---|---|---|
| **Location ID** | September | | | | | | October | | | | | |
| | **Intercept estimate** | **SE** | **p < 0.05** | **Slope estimate** | **SE** | **p < 0.05** | **Intercept estimate** | **SE** | **p < 0.05** | **Slope estimate** | **SE** | **p < 0.05** |
| **1** | -0.086 | 0.787 | no | -0.215 | 0.072 | yes | -3.538 | 0.715 | yes | 0.044 | 0.079 | no |
| **2** | -3.469 | 0.534 | yes | 0.106 | 0.061 | no | -3.274 | 0.321 | yes | 0.100 | 0.065 | no |
| **3** | -2.559 | 0.681 | yes | 0.024 | 0.061 | no | -2.897 | 0.420 | yes | 0.083 | 0.054 | no |
| **4** | -3.441 | 0.734 | yes | 0.038 | 0.079 | no | -4.138 | 0.561 | yes | 0.114 | 0.092 | no |
| **5** | -0.505 | 0.502 | no | -0.294 | 0.074 | yes | -2.494 | 0.248 | yes | -0.038 | 0.052 | no |
| **6** | -2.567 | 0.460 | yes | 0.090 | 0.050 | no | -2.205 | 0.208 | yes | 0.118 | 0.040 | yes |
| **7** | -1.055 | 0.770 | no | -0.243 | 0.092 | yes | -1.697 | 0.227 | yes | -0.110 | 0.043 | yes |
| **8** | -2.327 | 0.628 | yes | -0.059 | 0.075 | no | -2.946 | 0.291 | yes | -0.002 | 0.064 | no |
| **9** | -1.136 | 1.004 | no | -0.173 | 0.092 | no | -2.210 | 0.622 | yes | -0.392 | 0.132 | yes |
| **10** | -2.674 | 0.775 | yes | -0.023 | 0.078 | no | -3.951 | 0.619 | yes | 0.057 | 0.093 | no |
| **11** | -0.567 | 0.929 | no | -0.193 | 0.083 | yes | -4.915 | 1.098 | yes | 0.136 | 0.114 | no |
| **12** | -0.721 | 0.659 | no | -0.176 | 0.067 | yes | -2.545 | 0.400 | yes | -0.006 | 0.057 | no |
| **13** | -4.433 | 2.256 | yes | 0.212 | 0.183 | no | -3.715 | 1.321 | yes | 0.205 | 0.160 | no |
| **14** | -3.044 | 0.497 | yes | 0.122 | 0.052 | yes | -2.470 | 0.262 | yes | 0.091 | 0.047 | no |
| **15** | -4.422 | 0.679 | yes | 0.216 | 0.083 | yes | -3.864 | 0.409 | yes | 0.148 | 0.094 | no |
| **16** | -5.271 | 2.188 | yes | 0.094 | 0.168 | no | -3.795 | 1.274 | yes | -0.098 | 0.159 | no |
| | November | | | | | | December | | | | | |
| **1** | -2.546 | 0.312 | yes | -0.061 | 0.056 | no | -2.282 | 0.205 | yes | 0.002 | 0.046 | no |
| **2** | -2.628 | 0.218 | yes | 0.177 | 0.051 | yes | -1.898 | 0.189 | yes | 0.413 | 0.070 | yes |
| **3** | -2.245 | 0.206 | yes | 0.002 | 0.042 | no | -2.822 | 0.261 | yes | 0.342 | 0.060 | yes |
| **4** | -3.342 | 0.285 | yes | 0.049 | 0.062 | no | -3.635 | 0.421 | yes | 0.672 | 0.131 | yes |
| **5** | -2.290 | 0.175 | yes | 0.002 | 0.036 | no | -2.798 | 0.252 | yes | 0.072 | 0.052 | no |
| **6** | -1.567 | 0.132 | yes | 0.125 | 0.033 | yes | -0.965 | 0.123 | yes | 0.230 | 0.036 | yes |
| **7** | -2.730 | 0.218 | yes | 0.005 | 0.049 | no | -2.130 | 0.160 | yes | 0.124 | 0.047 | yes |
| **8** | -3.007 | 0.249 | yes | 0.081 | 0.058 | no | -2.265 | 0.209 | yes | 0.147 | 0.050 | yes |
| **9** | -3.507 | 0.471 | yes | -0.082 | 0.093 | no | -3.088 | 0.269 | yes | -0.037 | 0.066 | no |
| **10** | -3.684 | 0.343 | yes | -0.022 | 0.076 | no | -3.560 | 0.316 | yes | 0.025 | 0.075 | no |
| **11** | -2.913 | 0.327 | yes | -0.201 | 0.072 | yes | -3.186 | 0.304 | yes | 0.056 | 0.068 | no |
| **12** | -3.080 | 0.297 | yes | 0.026 | 0.062 | no | -2.752 | 0.207 | yes | 0.074 | 0.056 | no |
| **13** | -2.578 | 0.613 | yes | 0.292 | 0.117 | yes | -3.032 | 0.829 | yes | 0.516 | 0.205 | yes |
| **14** | -1.744 | 0.138 | yes | 0.086 | 0.033 | yes | -1.525 | 0.143 | yes | 0.320 | 0.051 | yes |
| **15** | -3.156 | 0.291 | yes | 0.223 | 0.084 | yes | -3.459 | 0.461 | yes | 0.390 | 0.170 | yes |
| **16** | -4.685 | 0.923 | yes | 0.033 | 0.146 | no | -5.374 | 0.957 | yes | 0.260 | 0.170 | no |

Table B3: $Lr_2$ model results with daily mean temperature as predictor for May to August.

| | Month | | | | | | | | | | | |
|---|---|---|---|---|---|---|---|---|---|---|---|---|
| **Location ID** | Jan | | | | | | Feb | | | | | |
| | **Intercept estimate** | **SE** | **p < 0.05** | **Slope estimate** | **SE** | **p < 0.05** | **Intercept estimate** | **SE** | **p < 0.05** | **Slope estimate** | **SE** | **p < 0.05** |
| **1** | -2.204 | 0.175 | yes | 0.037 | 0.009 | yes | -2.201 | 0.194 | yes | 0.029 | 0.013 | yes |
| **2** | -2.090 | 0.168 | yes | 0.065 | 0.012 | yes | -2.161 | 0.184 | yes | 0.053 | 0.014 | yes |
| **3** | -1.730 | 0.149 | yes | 0.033 | 0.007 | yes | -1.667 | 0.150 | yes | 0.031 | 0.007 | yes |
| **4** | -3.095 | 0.269 | yes | 0.015 | 0.016 | no | -3.156 | 0.274 | yes | 0.061 | 0.014 | yes |
| **5** | -2.784 | 0.246 | yes | 0.006 | 0.027 | no | -2.448 | 0.221 | yes | 0.001 | 0.030 | no |
| **6** | -2.209 | 0.172 | yes | 0.062 | 0.015 | yes | -1.473 | 0.134 | yes | 0.061 | 0.016 | yes |
| **7** | -2.423 | 0.192 | yes | 0.057 | 0.013 | yes | -2.609 | 0.212 | yes | 0.080 | 0.015 | yes |
| **8** | -2.647 | 0.208 | yes | 0.064 | 0.035 | no | -3.216 | 0.282 | yes | 0.102 | 0.057 | no |
| **9** | -3.021 | 0.261 | yes | 0.021 | 0.013 | no | -3.315 | 0.283 | yes | 0.047 | 0.011 | yes |
| **10** | -3.157 | 0.285 | yes | 0.019 | 0.012 | no | -2.928 | 0.276 | yes | 0.006 | 0.016 | no |
| **11** | -3.336 | 0.289 | yes | 0.035 | 0.013 | yes | -3.098 | 0.268 | yes | 0.063 | 0.015 | yes |
| **12** | -2.474 | 0.202 | yes | 0.025 | 0.010 | yes | -2.210 | 0.195 | yes | 0.020 | 0.014 | no |
| **13** | -1.488 | 0.358 | yes | 0.017 | 0.017 | no | -0.369 | 0.314 | no | -0.009 | 0.031 | no |
| **14** | -1.690 | 0.142 | yes | 0.043 | 0.008 | yes | -1.194 | 0.126 | yes | 0.008 | 0.011 | no |
| **15** | -3.562 | 0.361 | yes | -0.008 | 0.030 | no | -4.342 | 0.476 | yes | 0.059 | 0.024 | yes |
| **16** | -3.985 | 0.404 | yes | 0.053 | 0.024 | yes | -3.513 | 0.371 | yes | 0.000 | 0.041 | no |
| | March | | | | | | April | | | | | |
| **1** | -2.667 | 0.206 | yes | 0.038 | 0.010 | yes | -2.779 | 0.230 | yes | 0.036 | 0.015 | yes |
| **2** | -1.815 | 0.139 | yes | 0.033 | 0.008 | yes | -2.306 | 0.196 | yes | 0.022 | 0.025 | no |
| **3** | -1.809 | 0.143 | yes | 0.024 | 0.006 | yes | -2.494 | 0.202 | yes | 0.027 | 0.011 | yes |
| **4** | -2.846 | 0.230 | yes | 0.019 | 0.013 | no | -2.714 | 0.222 | yes | 0.032 | 0.017 | no |
| **5** | -2.168 | 0.180 | yes | -0.008 | 0.023 | no | -2.285 | 0.189 | yes | 0.021 | 0.028 | no |
| **6** | -0.892 | 0.103 | yes | 0.007 | 0.013 | no | -1.671 | 0.139 | yes | 0.081 | 0.020 | yes |
| **7** | -2.635 | 0.198 | yes | 0.050 | 0.012 | yes | -2.645 | 0.217 | yes | 0.029 | 0.024 | no |
| **8** | -2.771 | 0.219 | yes | 0.036 | 0.038 | no | -2.736 | 0.214 | yes | 0.052 | 0.033 | no |
| **9** | -3.120 | 0.278 | yes | 0.023 | 0.017 | no | -2.332 | 0.210 | yes | -0.022 | 0.025 | no |
| **10** | -2.539 | 0.224 | yes | -0.013 | 0.017 | no | -2.941 | 0.246 | yes | 0.027 | 0.013 | yes |
| **11** | -2.521 | 0.211 | yes | 0.008 | 0.016 | no | -2.626 | 0.225 | yes | 0.005 | 0.022 | no |
| **12** | -2.234 | 0.180 | yes | 0.015 | 0.012 | no | -2.343 | 0.193 | yes | 0.014 | 0.017 | no |
| **13** | -0.759 | 0.275 | yes | -0.019 | 0.029 | no | -1.391 | 0.409 | yes | 0.023 | 0.038 | no |
| **14** | -1.507 | 0.128 | yes | 0.027 | 0.009 | yes | -1.535 | 0.138 | yes | 0.022 | 0.015 | no |
| **15** | -2.887 | 0.236 | yes | 0.026 | 0.017 | no | -2.413 | 0.209 | yes | -0.006 | 0.026 | no |
| **16** | -3.469 | 0.372 | yes | -0.083 | 0.080 | no | -4.038 | 0.474 | yes | -0.033 | 0.086 | no |

Table B4: $Lr_2$ model results with daily mean temperature as predictor for September to December

| | **Month** | | | | | | | | | | | |
|---|---|---|---|---|---|---|---|---|---|---|---|---|
| **Location ID** | May | | | | | | June | | | | | |
| | **Intercept estimate** | **SE** | **p < 0.05** | **Slope estimate** | **SE** | **p < 0.05** | **Intercept estimate** | **SE** | **p < 0.05** | **Slope estimate** | **SE** | **p < 0.05** |
| **1** | -3.088 | 0.263 | yes | 0.018 | 0.025 | no | -2.778 | 0.226 | yes | 0.037 | 0.020 | no |
| **2** | -2.586 | 0.216 | yes | -0.005 | 0.038 | no | -3.716 | 0.328 | yes | 0.101 | 0.023 | yes |
| **3** | -3.038 | 0.257 | yes | 0.014 | 0.019 | no | -3.220 | 0.271 | yes | 0.039 | 0.014 | yes |
| **4** | -3.371 | 0.297 | yes | 0.031 | 0.028 | no | -3.235 | 0.298 | yes | 0.016 | 0.033 | no |
| **5** | -2.533 | 0.213 | yes | 0.020 | 0.038 | no | -2.603 | 0.224 | yes | -0.008 | 0.041 | no |
| **6** | -2.196 | 0.169 | yes | 0.073 | 0.026 | yes | -2.751 | 0.220 | yes | 0.104 | 0.027 | yes |
| **7** | -2.879 | 0.235 | yes | 0.051 | 0.030 | no | -2.893 | 0.243 | yes | 0.043 | 0.031 | no |
| **8** | -3.518 | 0.298 | yes | 0.143 | 0.047 | yes | -3.926 | 0.369 | yes | 0.103 | 0.043 | yes |
| **9** | -2.303 | 0.199 | yes | -0.034 | 0.033 | no | -3.262 | 0.303 | yes | -0.004 | 0.033 | no |
| **10** | -3.308 | 0.286 | yes | 0.024 | 0.020 | no | -3.568 | 0.340 | yes | 0.030 | 0.023 | no |
| **11** | -3.242 | 0.274 | yes | 0.032 | 0.025 | no | -3.348 | 0.310 | yes | 0.012 | 0.029 | no |
| **12** | -2.936 | 0.251 | yes | -0.006 | 0.034 | no | -3.288 | 0.286 | yes | 0.060 | 0.021 | yes |
| **13** | -2.090 | 0.472 | yes | 0.129 | 0.071 | no | -1.520 | 0.424 | yes | -0.070 | 0.068 | no |
| **14** | -2.189 | 0.179 | yes | 0.020 | 0.023 | no | -2.973 | 0.241 | yes | 0.078 | 0.018 | yes |
| **15** | -2.180 | 0.186 | yes | -0.026 | 0.032 | no | -3.108 | 0.267 | yes | 0.045 | 0.022 | yes |
| **16** | -4.680 | 0.532 | yes | 0.060 | 0.039 | no | -5.034 | 0.773 | yes | -0.109 | 0.217 | no |
| | July | | | | | | August | | | | | |
| **1** | -3.807 | 0.356 | yes | 0.063 | 0.020 | yes | -2.681 | 0.263 | yes | -0.046 | 0.037 | no |
| **2** | -3.952 | 0.445 | yes | -0.023 | 0.080 | no | -3.076 | 0.272 | yes | 0.061 | 0.024 | yes |
| **3** | -2.811 | 0.241 | yes | 0.024 | 0.017 | no | -2.687 | 0.227 | yes | 0.027 | 0.011 | yes |
| **4** | -2.719 | 0.263 | yes | -0.060 | 0.050 | no | -3.358 | 0.320 | yes | 0.030 | 0.026 | no |
| **5** | -3.120 | 0.274 | yes | 0.056 | 0.031 | no | -2.381 | 0.230 | yes | -0.058 | 0.045 | no |
| **6** | -3.100 | 0.250 | yes | 0.072 | 0.023 | yes | -2.667 | 0.239 | yes | 0.016 | 0.037 | no |
| **7** | -3.107 | 0.265 | yes | 0.052 | 0.027 | no | -3.168 | 0.279 | yes | 0.067 | 0.026 | yes |
| **8** | -4.307 | 0.468 | yes | 0.100 | 0.070 | no | -2.723 | 0.261 | yes | -0.083 | 0.078 | no |
| **9** | -5.572 | 0.790 | yes | 0.093 | 0.035 | yes | -3.524 | 0.350 | yes | 0.038 | 0.021 | no |
| **10** | -3.767 | 0.370 | yes | 0.037 | 0.023 | no | -3.512 | 0.352 | yes | 0.016 | 0.022 | no |
| **11** | -3.001 | 0.262 | yes | 0.022 | 0.023 | no | -3.142 | 0.290 | yes | 0.017 | 0.018 | no |
| **12** | -3.125 | 0.276 | yes | 0.031 | 0.027 | no | -3.062 | 0.263 | yes | 0.043 | 0.016 | yes |
| **13** | -2.365 | 0.554 | yes | 0.121 | 0.048 | yes | -3.204 | 0.753 | yes | 0.133 | 0.050 | yes |
| **14** | -2.420 | 0.202 | yes | 0.056 | 0.022 | yes | -2.890 | 0.234 | yes | 0.049 | 0.014 | yes |
| **15** | -3.977 | 0.392 | yes | 0.072 | 0.031 | yes | -3.576 | 0.332 | yes | 0.046 | 0.018 | yes |
| **16** | -5.133 | 0.745 | yes | 0.052 | 0.074 | no | -4.724 | 0.616 | yes | 0.022 | 0.039 | no |

## B.2 GitHub Repository

Scripts developed for this study can be found here in this GitHub repository:

`https://github.com/Emhjellen-UiO/Emhjellen_masteroppgave.git`

# Bibliography

Alkhasawneh, M. S., Ngah, U. K., Tay, L. T. & Isa, N. A. M. (2014). Determination of importance for comprehensive topographic factors on landslide hazard mapping using artificial neural network. *Environmental earth sciences*, vol. 72no. 3, 787–799.

Allen, S. & Huggel, C. (2013). Extremely warm temperatures as a potential cause of recent high mountain rockfall [Place: Amsterdam Publisher: Elsevier B.V]. *Global and planetary change*, vol. 107, 59–69.

Anderson, R. S. (1998). Near-Surface Thermal Profiles in Alpine Bedrock: Implications for the Frost Weathering of Rock [Place: BOULDER Publisher: Institute of Arctic and Alpine Research]. *Arctic and alpine research*, vol. 30no. 4, 362–372.

Bagheri, V., Uromeihy, A. & Fatemi Aghda, S. M. (2018). Predicting the probability of rockfalls occurrence caused by the earthquake of Changureh-Avaj in 2002 using LR, MLP, and RBF methods [Place: Berlin/Heidelberg Publisher: unav]. *Bulletin of engineering geology and the environment*, vol. 78no. 5, 3119–3141.

Bakkehøi, S. (2003). Utløsende årsak til flomskred i sandvikselva, sunndal og skiftingsgrova, eikedalsvatnet. NGI.

Blikra, L., Longva, O., Braathen, A., Anda, E., Dehls, J. & Stalsberg, K. (2006). Rock slope failures in norwegian fjord areas: Examples, spatial distribution and temporal pattern, In *Landslides from massive rock slope failure*. Springer.

Bozorgzadeh, N. & Bathurst, R. J. (2020). Hierarchical Bayesian approaches to statistical modelling of geotechnical data [Place: ABINGDON Publisher: TAYLOR & FRANCIS LTD]. *Georisk*, 1–18.

Bozorgzadeh, N., Harrison, J. P. & Escobar, M. D. (2019). Hierarchical Bayesian modelling of geotechnical data: Application to rock strength [Publisher: Thomas Telford Ltd]. *Géotechnique*. https://doi.org/10.1680/jgeot.17.P.282

Brunetti, M. T., Peruccacci, S., Rossi, M., Luciani, S., Valigi, D. & Guzzetti, F. (2010). Rainfall thresholds for the possible occurrence of landslides in Italy. *Natural Hazards and Earth System Sciences*, vol. 10no. 3, 447–458. https://doi.org/10.5194/nhess-10-447-2010

Böhme, M., Derron, M.-H. & Jaboyedoff, M. (2013). Quantitative spatial analysis of rockfalls from road inventories: A combined statistical and physical susceptibility model. *Natural Hazards and Earth System Sciences Discussions*, vol. 2. https://doi.org/10.5194/nhessd-2-81-2014

Chau, K. T., Wong, R. H. C., Liu, J. & Lee, C. F. (2003). Rockfall hazard analysis for Hong Kong based on rockfall inventory [Publisher: Springer]. *Rock Mechanics and Rock Engineering*, vol. 36no. 5, 383–408.

Choi, J. C., Liu, Z., Lacasse, S. & Skurtveit, E. (2021). Leak-Off Pressure Using Weakly Correlated Geospatial Information and Machine Learning Algorithms [Publisher: MDPI AG]. *Geosciences (Basel)*, vol. 11no. 181, 181.

Christen, M., Bühler, Y., Bartelt, P., Leine, R., Glover, J., Schweizer, A., Graf, C., McArdell, B. W., Gerber, W., Deubelbeiss, Y., Feistl, T. & Volkwein, A. (2012). INTEGRAL HAZARD MANAGEMENT USING A UNIFIED SOFTWARE ENVIRONMENT, 10.

Collins, B. D. & Stock, G. M. (2016). Rockfall triggering by cyclic thermal stressing of exfoliation fractures [Publisher: Springer Science and Business Media LLC]. *Nature geoscience*, vol. 9no. 5, 395–400.

Coutard, J.-P. & Francou, B. (1989). Rock Temperature Measurements in Two Alpine Environments: Implications for Frost Shattering [Publisher: Institute of Arctic and Alpine Research]. *Arctic and alpine research*, vol. 21no. 4, 399–416.

D'Amato, J., Hantz, D., Guerin, A., Jaboyedoff, M., Baillet, L. & Mariscal, A. (2015). Influence of meteorological factors on rockfall occurrence in a middle mountain limestone cliff. *Natural Hazards and Earth System Sciences*, 7587–7630.

D'Amato, J., Hantz, D., Guerin, A., Jaboyedoff, M., Baillet, L. & Mariscal, A. (2016). Influence of meteorological factors on rockfall occurrence in a middle mountain limestone cliff. *Natural Hazards and Earth System Sciences*.

Davies, M. C. R., Hamza, O. & Harris, C. (2001). The effect of rise in mean annual temperature on the stability of rock slopes containing ice-filled discontinuities [Place: Chichester, UK Publisher: John Wiley & Sons, Ltd]. *Permafrost and periglacial processes*, vol. 12no. 1, 137–144.

Davies, M. C. R., Hamza, O., Lumsden, B. W. & Harris, C. (2000). Laboratory measurement of the shear strength of ice-filled rock joints [Publisher: Cambridge University Press]. *Annals of Glaciology*, vol. 31, 463–467. https://doi.org/10.3189/172756400781819897

DeCoster, J. (2006). Testing group differences using t-tests, anova, and nonparametric measures. *Accessed November*, vol. 30no. 2010, 202006–.

Delonca, A., Gunzburger, Y. & Verdel, T. (2014). Statistical correlation between meteorological and rockfall databases. *Natural Hazards and Earth System Sciences*, vol. 14no. 8, 1953–1964. https://doi.org/10.5194/nhess-14-1953-2014

Derczynski, L. (2016). Complementarity, F-score, and NLP Evaluation, In *Proceedings of the Tenth International Conference on Language Resources and Evaluation (LREC'16)*, Portorož, Slovenia, European Language Resources Association (ELRA). Retrieved March 27, 2021, from https://www.aclweb.org/anthology/L16-1040

Derron, M.-H. (2010). *Method for the susceptibility mapping of rock falls in norway, tech. rep.* (tech. rep.). Geological Survey of Norway.

Dorren, L. K. (2003). A review of rockfall mechanics and modelling approaches [Publisher: SAGE Publications Ltd]. *Progress in Physical Geography: Earth and Environment*, vol. 27no. 1, 69–87. https://doi.org/10.1191/0309133303pp359ra

Dorren, L. & Berger, F. (2010). New approaches for 3D rockfall modelling with or without the effect of forest in Rockyfor3D.

Dou, J., Yunus, A. P., Bui, D. T., Merghadi, A., Sahana, M., Zhu, Z., Chen, C.-W., Khosravi, K., Yang, Y. & Pham, B. T. (2019). Assessment of advanced random forest and decision tree algorithms for modeling rainfall-induced landslide susceptibility in the izu-oshima volcanic island, japan. *Science of the total environment*, vol. 662, 332–346.

Douglas, G. (1980). Magnitude frequency study of rockfall in co. antrim, n. ireland. *Earth Surface Processes*, vol. 5no. 2, 123–129.

Dyrrdal, A. V., Isaksen, K., Hygen, H. O. & Meyer, N. K. (2012). Changes in meteorological variables that can trigger natural hazards in Norway [Publisher: Inter-Research]. *Climate research*, vol. 55no. 2, 153–165.

Erener, A. & Düzgün, H. S. B. (2010). Improvement of statistical landslide susceptibility mapping by using spatial and global regression methods in the case of More and Romsdal (Norway) [Place: Berlin/Heidelberg Publisher: Springer-Verlag]. *Landslides*, vol. 7no. 1, 55–68.

Fanos, A. M. & Pradhan, B. (2019). A Novel Hybrid Machine Learning-Based Model for Rockfall Source Identification in Presence of Other Landslide Types Using LiDAR and GIS [Place: Cham Publisher: Springer Science and Business Media LLC]. *Earth systems and environment*, vol. 3no. 3, 491–506.

Frauenfelder, R., Solheim, A., Isaksen, K., Romstad, B., Dyrrdal, A., Ekseth, K., Gangstø, R., Harbitz, A., Harbitz, C., Haugen, J. Et al. (2013). *Impacts of extreme weather events on infrastructure in norway* (tech. rep.). Report 20091808-01-R, Norwegian Geotechnical Institute, Oslo, Norway.

Frayssines, M. & Hantz, D. (2006). Failure mechanisms and triggering factors in calcareous cliffs of the subalpine ranges (french alps). *Engineering Geology*, vol. 86no. 4, 256–270.

Gelman, A., Carlin, J. B., Stern, H. S., Dunson, D. B., Vehtari, A. & Rubin, D. B. (2013). *Bayesian Data Analysis* (3rd ed.). New York, Chapman; Hall/CRC. https://doi.org/10.1201/b16018

Géron, A. (2019). *Hands-on machine learning with scikit-learn, keras, and tensorflow: Concepts, tools, and techniques to build intelligent systems.* O'Reilly Media.

Gilbert, G. (2020, October 23).

Grove, J. M. (1972). The Incidence of Landslides, Avalanches, and Floods in Western Norway during the Little Ice Age [Publisher: Institute of Arctic and Alpine Research]. *Arctic and alpine research*, vol. 4no. 2, 131–138.

Hales, T. & Roering, J. J. (2007). Climatic controls on frost cracking and implications for the evolution of bedrock landscapes. *Journal of Geophysical Research: Earth Surface*, vol. 112no. F2.

Hanssen-Bauer, I., Førland, E., Haddeland, I., Hisdal, H., Lawrence, D., Mayer, S., Nesje, A., Nilsen, J., Sandven, S., Sandø, A., Sorteberg, A. & Ådlandsvik, B. (2017). *Climate in Norway 2100 - a knowledge base for climate adaptation* (tech. rep. No. 1). The Norwegian Centre for Climate Services.

Hantz, D., Dewez, T., Levy, C., Guerin, A. & Jaboyedoff, M. (2016). Rockfal frequency in different geomorphological conditions, In *International symposium rock slope stability*.

Hastie, T., Tibshirani, R. & Friedman, J. H. (2009). *The elements of statistical learning data mining, inference, and prediction.* Springer.

Hefre, H., Ekseth, K. H., Høydahl, Ø. A. & Vernang, T. (2016). https://publikasjoner.nve.no/rapport/2016/rapport2016_21.pdf

Hjort, J. & Marmion, M. (2008). Effects of sample size on the accuracy of geomorphological models [Place: Amsterdam Publisher: Elsevier B.V]. *Geomorphology (Amsterdam, Netherlands)*, vol. 102no. 3, 341–350.

Hjort, J., Ujanen, J., Parviainen, M., Tolgensbakk, J. & Etzelmüller, B. (2014). Transferability of geomorphological distribution models: Evaluation using solifluction features in subarctic and Arctic regions. *Geomorphology*, vol. 204, 165–176. https://doi.org/10.1016/j.geomorph.2013.08.002

Hoek, E. (1981). *Rock slope engineering* (Rev. 3rd ed.). London, The Institution of Mining; Metallurgy.

Hosmer, D. W., Lemeshow, S. & Sturdivant, R. X. (2013). *Applied logistic regression, third edition* (3rd ed.). Hoboken, NJ, John Wiley; Sons.

Hungr, O., Evans, S. G. & Hazzard, J. (1999). Magnitude and frequency of rock falls and rock slides along the main transportation corridors of southwestern British Columbia [Place: Ottawa, Canada Publisher: Canadian Science Publishing]. *Canadian geotechnical journal*, vol. 36no. 2, 224–238.

Hungr, O., Evans, S. G., Bovis, M. J. & Hutchinson, J. N. (2001). A review of the classification of landslides of the flow type. *Environmental and Engineering Geoscience*, vol. 7no. 3, 221–238. https://doi.org/10.2113/gseegeosci.7.3.221

Hungr, O., Leroueil, S. & Picarelli, L. (2014). The Varnes classification of landslide types, an update. *Landslides*, vol. 11no. 2, 167–194. https://doi.org/10.1007/s10346-013-0436-y

Hutchinson, J. (1989). General report: Morphological and geotechnical parameters of landslides in relation to geology and hydrogeology. *International Journal of Rock Mechanics and Mining Sciences  Geomechanics Abstracts*, vol. 26no. 2, 88. https://doi.org/10.1016/0148-9062(89)90310-0

Jaedicke, C., Lied, K. & Kronholm, K. (2009). Integrated database for rapid mass movements in Norway [Publisher: Copernicus Publications]. *Natural hazards and earth system sciences*, vol. 9no. 2, 469–479.

Jaedicke, C., Solheim, A., Blikra, L., Stalsberg, K., Sorteberg, A., Aaheim, A., Kronholm, K., Vikhamar-Schuler, D., Isaksen, K., Sletten, K., Kristensen, K., Barstad, I., Melchiorre, C., Høydal, Ø. & Mestl, H. (2008). Spatial and temporal variations of Norwegian geohazards in a changing climate, the GeoExtreme Project [Place: GOTTINGEN Publisher: COPERNICUS GESELLSCHAFT MBH]. *Natural hazards and earth system sciences*, vol. 8no. 4, 893–904.

Jiménez-Perálvarez, J. D., Irigaray, C., El Hamdouni, R. & Chacón, J. (2009). Building models for automatic landslide-susceptibility analysis, mapping and validation in ArcGIS [Publisher: Springer]. *Natural hazards (Dordrecht)*, vol. 50no. 3, 571–590.

Kalsnes, B., Solheim, A., Sverdrup-Thygeson, K., Dingsør-Dehlin, F., Wasrud, J., Indrevær, K. & Bergbjørn, K. (2021). Flom og skred–sikringsbehov for eksisterende bebyggelse (foss).

Karpatne, A., Ebert-Uphoff, I., Ravela, S., Babaie, H. A. & Kumar, V. (2019). Machine Learning for the Geosciences: Challenges and Opportunities [Conference Name: IEEE Transactions on Knowledge and Data Engineering]. *IEEE Transactions on Knowledge and Data Engineering*, vol. 31no. 8, 1544–1554. https://doi.org/10.1109/TKDE.2018.2861006

Kellerer-Pirklbauer, A. (2017). Potential weathering by freeze-thaw action in alpine rocks in the European Alps during a nine year monitoring period. *Geomorphology*, vol. 296, 113–131. https://doi.org/10.1016/j.geomorph.2017.08.020

Krautblatter, M. & Moser, M. (2009). A nonlinear model coupling rockfall and rainfall intensity based on a four year measurement in a high Alpine rock wall (Reintal, German Alps). *Natural Hazards and Earth System Sciences*, vol. 9. https://doi.org/10.5194/nhess-9-1425-2009

Kristensen, L., Czekirda, J., Penna, I., Bernd, E., Nicolet, P., Pullarello, J. S., Blikra, L. H., Skrede, I., Oldani, S. & Abellan, A. (2021). Movements, failure and climatic control of the Veslemannen rockslide, Western Norway [Place: HEIDELBERG Publisher: SPRINGER HEIDELBERG]. *Landslides*, vol. 18no. 6, 1963–1980.

Kruskal, W. H. & Wallis, W. A. (1952). Use of Ranks in One-Criterion Variance Analysis [Publisher: Taylor & Francis Group]. *Journal of the American Statistical Association*, vol. 47no. 260, 583–621.

Kuhn, M. (2013). *Applied predictive modeling* (1st ed. 2013.). New York, New York, Springer.

Lied, K. & Bakkehøi, K. (1980). Empirical calculations of snow–avalanche run–out distance based on topographic parameters. *Journal of Glaciology*, vol. 26no. 94, 165–177.

Liu, Z., Gilbert, G., Cepeda, J. M., Lysdahl, A. O. K., Piciullo, L., Hefre, H. & Lacasse, S. (2020). Modelling of shallow landslides with machine learning algorithms [Publisher: Elsevier B.V]. *Di xue qian yuan.*

Lombardo, L. & Mai, P. M. (2018). Presenting logistic regression-based landslide susceptibility results. *Engineering Geology*, vol. 244, 14–24. https://doi.org/10.1016/j.enggeo.2018.07.019

Losasso, L. & Sdao, F. (2018). The artificial neural network for the rockfall susceptibility assessment. A case study in Basilicata (Southern Italy) [Publisher: Informa UK Limited]. *Geomatics, natural hazards and risk*, vol. 9no. 1, 737–759.

Luckman, B. H. (1976). Rockfalls and rockfall inventory data: Some observations from surprise valley, Jasper National Park, Canada [_eprint: https://onlinelibrary.wiley.com/doi/pdf/10.1002/esp.3290010309]. *Earth Surface Processes*, vol. 1no. 3, 287–298. https://doi.org/https://doi.org/10.1002/esp.3290010309

Lussana, C., Saloranta, T., Skaugen, T., Magnusson, J., Tveito, O. E. & Andersen, J. (2018). seNorge2 daily precipitation, an observational gridded dataset over Norway from 1957 to the present day [Publisher: Copernicus GmbH]. *Earth system science data*, vol. 10no. 1, 235–249.

Macciotta, R., Hendry, M., Cruden, D., Blais-Stevens, A. & Edwards, T. (2017). Quantifying rock fall probabilities and their temporal distribution associated with weather seasonality. *Landslides*. https://doi.org/10.1007/s10346-017-0834-7

Marmion, M., Hjort, J., Thuiller, W. & Luoto, M. (2008). A comparison of predictive methods in modelling the distribution of periglacial landforms in Finnish Lapland [Place: Chichester, UK Publisher: John Wiley & Sons, Ltd]. *Earth surface processes and landforms*, vol. 33no. 14, 2241–2254.

Marquínez, J., Menéndez Duarte, R., Farias, P. & JiméNez Sánchez, M. (2003). Predictive GIS-Based Model of Rockfall Activity in Mountain Cliffs [Place: Dordrecht Publisher: Kluwer Academic Publishers]. *Natural hazards (Dordrecht)*, vol. 30no. 3, 341–360.

Matsuoka, N. (1994). Diurnal freeze-thaw depth in rockwalls: Field measurements and theoretical considerations [Place: Sussex Publisher: John Wiley & Sons, Ltd]. *Earth surface processes and landforms*, vol. 19no. 5, 423–435.

Matsuoka, N. (2019). A multi-method monitoring of timing, magnitude and origin of rockfall activity in the Japanese Alps [Publisher: Elsevier B.V]. *Geomorphology (Amsterdam, Netherlands)*, vol. 336, 65–76.

Matsuoka, N. & Sakai, H. (1999). Rockfall activity from an alpine cliff during thawing periods [Publisher: Elsevier BV]. *Geomorphology (Amsterdam, Netherlands)*, vol. 28no. 3-4, 309–328.

McCarroll, D., Shakesby, R. A. & Matthews, J. A. (1998). Spatial and Temporal Patterns of Late Holocene Rockfall Activity on a Norwegian Talus Slope: A Lichenometric and Simulation-Modeling Approach [Publisher: Institute of Arctic and Alpine Research]. *Arctic and alpine research*, vol. 30no. 1, 51–60.

Mehta, P., Bukov, M., Wang, C.-H., Day, A. G., Richardson, C., Fisher, C. K. & Schwab, D. J. (2019). A high-bias, low-variance introduction to Machine Learning for physicists. *Physics Reports*, vol. 810, 1–124. https://doi.org/10.1016/j.physrep.2019.03.001

Miska, L. & Jan, H. (2005). Evaluation of current statistical approaches for predictive geomorphological mapping. *Geomorphology*, vol. 67no. 3-4, 299–315. https://doi.org/10.1016/j.geomorph.2004.10.006

Moen, K. & Humstad, T. (2009). Rv. *70 Oppdlstranda- Skredhendelser, risikovurdering, sikringstiltak. Fjellsprengningsteknikk, Bergmekanikk, Bergmekanikk/Geoteknikk*, vol. 27.

Park, S. & Kim, J. (2019). Landslide Susceptibility Mapping Based on Random Forest and Boosted Regression Tree Models, and a Comparison of Their Performance [Number: 5 Publisher: Multidisciplinary Digital Publishing Institute]. *Applied Sciences*, vol. 9no. 5, 942. https://doi.org/10.3390/app9050942

Pedregosa, F., Varoquaux, G., Gramfort, A., Michel, V., Thirion, B., Grisel, O., Blondel, M., Prettenhofer, P., Weiss, R., Dubourg, V. Et al. (2011). Scikit-learn: Machine learning in python. *the Journal of machine Learning research*, vol. 12, 2825–2830.

Pourghasemi, H. R. & Rahmati, O. (2018). Prediction of the landslide susceptibility: Which algorithm, which precision? *CATENA*, vol. 162, 177–192. https://doi.org/10.1016/j.catena.2017.11.022

Rapp, A. (1960). Recent Development of Mountain Slopes in Kärkevagge and Surroundings, Northern Scandinavia [Publisher: Swedish Society for Anthropology and Geography]. *Geografiska annaler*, vol. 42no. 2/3, 65–200.

Riley, S., Degloria, S. & Elliot, S. (1999). A Terrain Ruggedness Index that Quantifies Topographic Heterogeneity. *Internation Journal of Science*, vol. 5, 23–27.

Roberts, D. R., Bahn, V., Ciuti, S., Boyce, M. S., Elith, J., Guillera-Arroita, G., Hauenstein, S., Lahoz-Monfort, J. J., Schröder, B., Thuiller, W., Warton, D. I., Wintle, B. A., Hartig, F. & Dormann, C. F. (2017). Cross-validation strategies for data with temporal, spatial, hierarchical, or phylogenetic structure [_eprint: https://onlinelibrary.wiley.com/doi/pdf/10.1111/ecog.02881]. *Ecography*, vol. 40no. 8, 913–929. https://doi.org/10.1111/ecog.02881

Rupp, S. & Damm, B. (2020). A national rockfall dataset as a tool for analysing the spatial and temporal rockfall occurrence in Germany [_eprint: https://onlinelibrary.wiley.com/doi/pdf/10.1002/esp.4827]. *Earth Surface Processes and Landforms*, vol. 45no. 7, 1528–1538. https://doi.org/https://doi.org/10.1002/esp.4827

Samuel, A. L. (1959). Some Studies in Machine Learning Using the Game of Checkers. *IBM journal of research and development*, vol. 3no. 3, 210–229.

Sandersen, F. (2015). https://webfileservice.nve.no/API/PublishedFiles/Download/201802083/2317249

Sandersen, F., Bakkehøi, S., Hestnes, E. & Lied, K. (1997). The influence of meteorological factors on the initiation of debris flows, rockfalls, rockslides and rockmass stability. *Publikasjon - Norges Geotekniske Institutt*, vol. 201, 97–114.

Saravanan, R. & Sujatha, P. (2018). A State of Art Techniques on Machine Learning Algorithms: A Perspective of Supervised Learning Approaches in Data Classification, In *2018 Second International Conference on Intelligent Computing and Control Systems (ICICCS)*. https://doi.org/10.1109/ICCONS.2018.8663155

Sass, O. & Oberlechner, M. (2012). Is climate change causing increased rockfall frequency in Austria? *Natural Hazards and Earth System Sciences*, vol. 12no. 11, 3209–3216. https://doi.org/10.5194/nhess-12-3209-2012

Seneviratne, S. I., Nicholls, N., Easterling, D., Goodess, C. M., Kanae, S., Kossin, J., Luo, Y., Marengo, J., McInnes, K., Rahimi, M., Reichstein, M., Sorteberg, A., Vera, C., Zhang, X., Rusticucci, M., Semenov, V., Alexander, L. V., Allen, S., Benito, G., . . . Zwiers, F. W. (2012). Changes in Climate Extremes and their Impacts on the Natural Physical Environment, In *Managing the Risks of Extreme Events and Disasters to Advance Climate Change Adaptation*.

Shirzadi, A., Saro, L., Hyun Joo, O. & Chapi, K. (2012). A GIS-based logistic regression model in rock-fall susceptibility mapping along a mountainous road: Salavat Abad case study, Kurdistan, Iran. *Natural Hazards*, vol. 64no. 2, 1639–1656. https://doi.org/10.1007/s11069-012-0321-3

Smith, K. (2013). *Environmental hazards : Assessing risk and reducing disaster* (6th ed.). London, Routledge.

Steinsprang og steinskred. (2020). https://www.nve.no/naturfare/laer-om-naturfare/om-skred/steinsprang-og-steinskred/

Tajet, H. T. T. (2021). Ny normal 1991-2020.

The Norwegian Meteorological Institute. (2021). Klimaprofil sogn og fjordane. https://klimaservicesenter.no/kss/klimaprofiler/sogn-og-fjordane

Turner, A. K. & L. Schuster, R. (2012). *Rockfall : Characterization and control*. Washington, D.C, Transportation Research Board.

Varnes, D. J. (1978). Slope movement types and processes. *Special report*, vol. 176, 11–33.

Vegvesen, S. (2019). *Skredsikringsbehov for riks-og fylkesvegar i Region vest* (tech. rep.). https://www.vegvesen.no/fag/teknologi/geofag/skred/skredsikring

Volkwein, A., Schellenberg, K., Labiouse, V., Agliardi, F., Berger, F., Bourrier, F., Dorren, L. K. A., Gerber, W. & Jaboyedoff, M. (2011). Rockfall characterisation and structural protection – a review. *Natural Hazards and Earth System Sciences*, vol. 11no. 9, 2617–2651. https://doi.org/10.5194/nhess-11-2617-2011

Wyllie, D. C. & Mah, C. W. (2004). Rock Slope Engineering: Civil and Mining, 4th Edition, 456.

Yang, Y., Yang, J., Xu, C., Xu, C. & Song, C. (2019). Local-scale landslide susceptibility mapping using the B-GeoSVC model. *Landslides*, vol. 16no. 7, 1301–1312. https://doi.org/10.1007/s10346-019-01174-y

Zare, M., Pourghasemi, H. R., Vafakhah, M. & Pradhan, B. (2013). Landslide susceptibility mapping at Vaz Watershed (Iran) using an artificial neural network model: A comparison between multilayer perceptron (MLP) and radial basic function (RBF) algorithms. *Arabian Journal of Geosciences*, vol. 6no. 8, 2873–2888. https://doi.org/10.1007/s12517-012-0610-x

Zhai, Y., Song, W., Liu, X., Liu, L. & Zhao, X. (2018). A Chi-Square Statistics Based Feature Selection Method in Text Classification [ISSN: 2327-0594], In *2018 IEEE 9th International Conference on Software Engineering and Service Science (ICSESS)*. ISSN: 2327-0594. https://doi.org/10.1109/ICSESS.2018.8663882

Zwillinger, D. & Kokoska, S. (2000). *CRC standard probability and statistics tables and formulae*. Boca Raton, Chapman & Hall/CRC.

Å ilhán, K., Pánek, T. & HradeckÃ½, J. (2013). Implications of spatial distribution of rockfall reconstructed by dendrogeomorphological methods [Publisher: Copernicus GmbH]. *Natural hazards and earth system sciences*, vol. 13no. 7, 1817–1826.